POLYTECHNIC OF TURIN

MASTER's Degree in AEROSPACE ENGINEERING

MASTER's Degree Thesis

Conceptual design methodology and tool for reusable single-stage-to-orbit vehicles with horizontal take-off and landing

Supervisors

Dott.essa Roberta FUSARO

Prof. Nicole VIOLA

Ing. Valeria BORIO

Candidate

Tommaso MOLINARI

APRIL 2024

Summary

To date, space launchers remain prohibitively expensive and the low reliability compared to commercial aircraft stands out as the main obstacles of future space exploration plans. To address these challenges, future launch vehicles necessitate a paradigm-shift towards more reusable and sustainable assets. In the current fast evolving landscape of competitive launch vehicle design, the development of a dedicated Reusable Launch Vehicle (RLV) design methodology becomes crucial.

This thesis outlines the development steps towards an innovative sizing methodology for Single Stage to Orbit (SSTO) with Horizontal Takeoff and Horizontal Landing (HTOL) capabilities. Beginning with the elicitation of mission requirements, constraints, and assumptions, the methodology encompasses considerations such as vehicle geometry, propulsion strategy, and technological availability, thus defining conceptual configuration alternatives complemented by initial estimates of dimensions and performance to determine the technical feasibility of the planned mission. The iterative nature of this process aims at matching the hypothesized variables with the estimated ones, considering different Mach regimes, evaluating the thermal loads, and satisfying performance requirements across flight phases. During this highly iterative process, the definition of suitable propulsive configurations is critical to achieve the required thrust across different altitudes and minimizing propellant consumption. While this design procedure seeks convergence toward system volume and mass, a multiple-matching chart is developed to delineate the design space available for the chosen mission.

With the idea of subsequently integrating a graphical user interface developed in Matlab environment, this work provides a complete methodology and toolbox that contributes to advancing the conceptual design phase of future launch vehicles, essential for realizing cost-effective and reliable access to space.

Eventually, the methodology and the developed tool are applied to the case study of the SKYLON, a future reusable SSTO spaceplane developed by Reaction Engines Limited (REL), which exploits the Synergetic Air-Breathing Rocket Engine (SABRE) technology, a combined-cycle engine able to cover the entire mission profile of the vehicle using liquid hydrogen as propellant.

Table of Contents

List of Tables

List of Figures

Acronyms

ACE

Air Collection Enrichment

AFRSI

Advanced Flexible Reusable Surface Insulation

AMHC

Advanced Metallic Honeycomb

ATR

Air Turbo Ramjet

ELV

Expendable Launch Vehicle

ETW

Effective Takeoff Weight

GTOW

Gross Take-off Mass

HTOL

Horizontal Take-off and Landing

LACE

Liquid Air Cycle

LaRC

Langley Research Center

LEO

Low Earth Orbit

LH2

Liquid Hydrogen

LOX

Liquid Oxygen

RBCC

Rocket-Based Combined Cycle

RLV

Reusable Launch Vehicle

SABRE

Synergistic Air-Breathing Rocket Engine

SA/HC

Superalloy Honeycomb

SSTO

Single Stage to Orbit

TABI

Thermal Protection for Ablators and Vond Insulation

TBCC

Turbine-Based Combine Cycle

TI/HC

Titanium Honeycomb

TPS

Thermal Protection System

TSTO

Two Stage to Orbit

Chapter 1

Introduction

1.1 RLV - Reusable launch vehicles

Space launchers are still considered expensive today and have not yet reached the reliability of commercial aircraft. Many types of launch vehicles are ’expendable’ (ELVs), i.e. they can only be used once and the user pays for the entire vehicle.

As shown by Penn and Lindley in 1997 [1], the future-generation launch vehicle must be reusable to lower the cost of access to space and be more reliable. The main advantage of a reusable launch vehicle (RLV) is that it can be reused several times. All parts of the launcher can be recovered and reused. Furthermore, unlike expendable launch vehicles, whose first and last flight is the payload delivery flight, a reusable launch vehicle can be tested in flight before it is put into service and is therefore safer. This new utilization concept for launch vehicles thus brings with it numerous advantages that may overcome the reusable launcher’s needs like additional systems and landing gear or propellant for return and landing, which leads to an increase in the overall weight of the vehicle.

The idea of an RLV emerged as early as 1950 [2], but many years passed before a partially reusable launch vehicle was realized, as the level of technology at the time was not sufficient. To date, private companies and space agencies are pushing for the development of reusable launch vehicles (RLVs). The development of RLVs is estimated to be considerably more expensive than that of partially reusable launch vehicles or ELVs. However, RLVs offer the possibility of meeting both the current and future needs of the space industry. The term RLV is often used to refer to single-stage launch vehicles, transatmospheric launch vehicles, or military spaceplane configurations, but these terms are not interchangeable. For clarity, the term RLV is used for fully reusable vehicles that provide access to space, deployment of payloads on orbit, and controlled return to Earth [3].

So many reusability concepts can represent very different configurations. The initial categorization involves determining the number of stages for the vehicle, typically considering either a single-stage-to-orbit or a two-stage-to-orbit configuration for reusable spacecraft. Another critical factor is the propulsion strategy chosen, which may entail employing airbreathing engines during the initial ascent stages and switching to rocket propulsion when the atmosphere becomes too thin, or relying entirely on rocket propulsion throughout. Additionally, the method of takeoff and landing can vary between horizontal, resembling conventional aircraft, and vertical. The choice of takeoff mode is often a consequence of the propulsion concept selected rather than a predetermined decision, as the thrust requirements differ significantly between horizontal and vertical takeoff configurations.

1.2 Domain Specification

1.2.1 Application Domain: Conceptual Design Phase

The design of any aerospace vehicle evolves in three distinct and sequential phases that define the state of progress, starting from the high-level requirements that express the design topic desired by the stakeholders: Conceptual Design Phase, Preliminary Design Phase, and Detailed Design Phase. In the initial phase of the project, the design space of a prospective RLV design is unknown.

The focus of this study is on conceptual design, where configurations are defined and supported by an initial estimate of dimensions and performance to determine which spacecraft concepts are technically feasible for the chosen mission.

The emphasis of Conceptual Design assessment lies on achieving a high degree of correctness and multidisciplinary integration, rather than prioritizing a high degree of accuracy and disciplinary specificity [4].

This phase, which is the first step of the design process, requires the application of assumptions that are best made after careful evaluations, as the cost of changing the design increases and design freedom decreases as development progresses.

Decisions made at this stage of the design can determine the success or failure of the project.

Figure 1.1 shows the Design Freedom vs Knowledge available during the three different design phases.

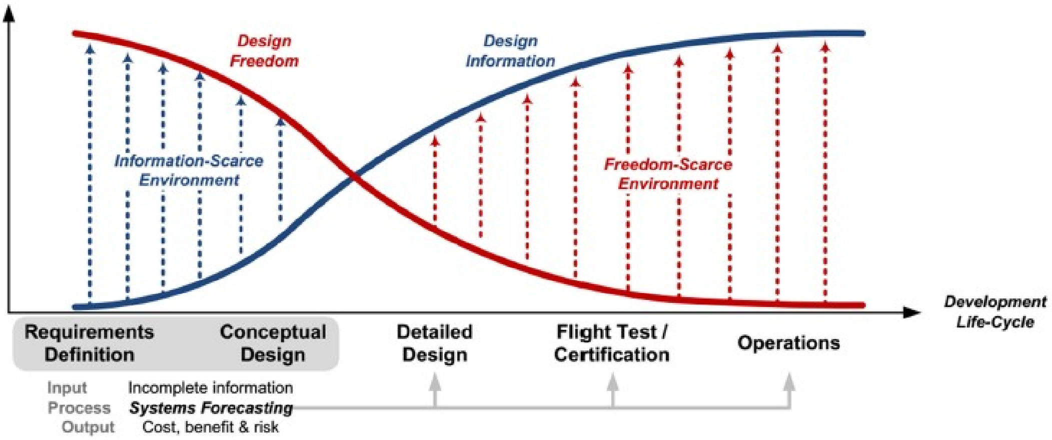

Figure 1.1: Aerospace Development Life-Cycle [5]

Chudoba notes, “The general life-cycle characteristics are established first during the conceptual design (CD) phase, clearly before a design proposal can be released to the follow-on design phases such as preliminary design (PD), detail design (DD), flight test (FT), and finally operation and disposal. CD is one of the most crucial life-cycle stages for a space program as the majority of the important decisions are locked down during this very development phase. As a rule of thumb, it can be assumed that around 80 percent of the flight vehicle configuration and mission tandem are determined during the CD phase alone, which is the key phase where the initial brainstorming has to take place." [6]
Once the conceptual design phase is finished, the baseline solution has been identified.

1.2.2 RLV Domain: Single Stage to Orbit HTOL

The thesis focuses on the development of a sizing methodology for the reusable launch vehicle configuration, specifically the single-stage-to-orbit (SSTO) design featuring horizontal take-off and landing procedures. It is alleged that SSTO holds superior long-term cost-effectiveness compared to the two-stage-to-orbit counterpart: despite the developmental challenges associated with single-stage vehicles, like complexity and engineering demands, they eliminate the need for duplicate hardware between stages, streamline recovery processes, and may reduce transportation costs. The idea of developing a fully reusable SSTO vehicle was significantly influenced by information gained from the partially reusable, multi-stage STS, such as the substantial costs linked to the various elements and infrastructure needed for that system.

Furthermore, the utilization of horizontal take-off not only reduces engine mass but also enhances operational flexibility through increased cross-range capabilities. This makes them ideally suited to meet the growing demand for economical and routine commercial space launches. Indeed, their potential for rapid reuse, through launches from any available airport, could narrow the considerable gaps in flight frequency and operational lifespan between a space launcher and an airliner. Categorized under hypersonic vehicles [7], a reusable single-stage-to-orbit (SSTO) spacecraft falls within the "Ascent and Re-entry Vehicles" classification within the Space Access System domain. Other categories within this domain include:

1. Reentry Vehicle Winged (RV-W) and Non-winged (RV-NW): The first vehicles execute controlled re-entry maneuvers within a planet's atmosphere, often following a gliding path. Their design is meticulously engineered to endure the intense thermal conditions of re-entry, while also allowing them to navigate and maneuver like traditional aircraft when within the atmosphere. The second type of vehicle is capable of executing a ballistic re-entry into a planet's atmosphere. Their design is significantly shaped by the imperative to optimize drag capacity for effective deceleration, all while staying within structural and thermal thresholds, often resulting in the adoption of blunt-shaped configurations. Examples are capsules or lifting bodies with restricted controllability.

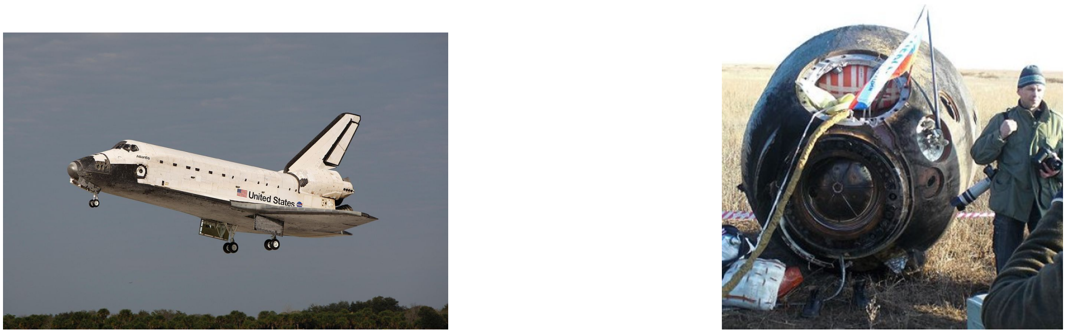

(a) RV-W ex: Space Shuttle

(b) RV-NW ex: Soyuz capsule

Figure 1.2: Reentry Vehicles

2. Cruise and Acceleration Vehicles (CAV): these aircraft-like slender vehicles, often equipped with air-breathing engines, are engineered for operation at high altitudes and low hypersonic speeds. During the design process, there's a strong focus on enhancing aerodynamic efficiency specifically for cruising. While they aren't intended for access to space, their primary function involves executing point-to-point missions, resembling the operations of commercial aircraft or serving as the lower stage in a two-stage-to-orbit system.

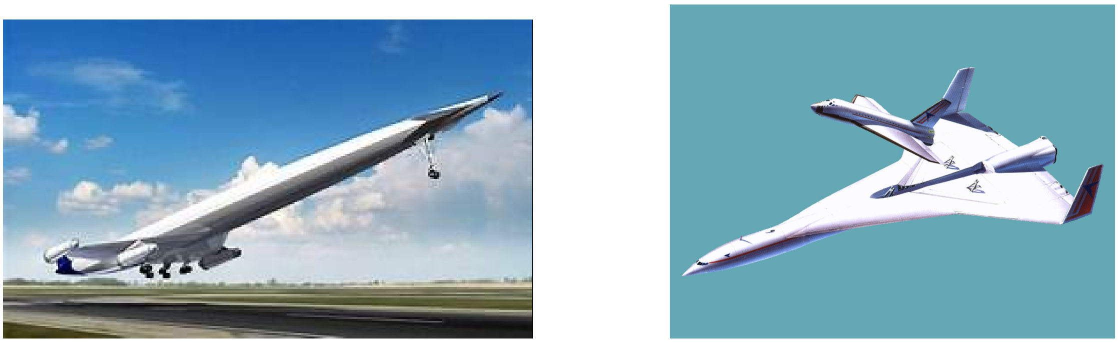

(a) CAV concept ex: Lapcat A2

(b) 1 Stage concept ex: Spacebus

Figure 1.3: Cruise and Acceleration Vehicles

3. Aero-Assisted Orbital Transfer Vehicles (AOTV): these vehicles commonly feature fixed, deployable, or inflatable heat shields designed to slow down the vehicle within the high-altitude atmosphere, utilizing atmospheric drag as a braking mechanism for the reentry from planetary missions or geosynchronous orbits. A problematic aspect is to design a control system capable of managing density irregularities, often referred to as "bumps". While early lifting brake concepts in Fig. 1.4a utilized an aerosurface that was a nearly flat disk, recent designs have shifted towards a wide-angle cone configuration with rounded outer edges to mitigate edge heating, in Fig. 1.4b. Experimental research has highlighted the significance of edge heating and afterbody heating, which notably diminish the usable angle-of-attack range and/or afterbody length for these configurations.

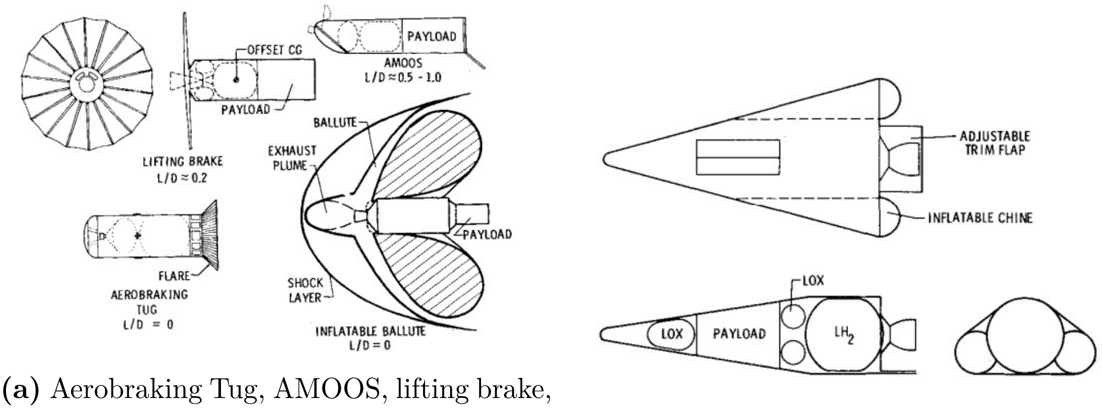

(a) Aerobraking Tug, AMOOS, lifting brake, ballute

(b) AOTV featuring high L/D capability

Figure 1.4: AOTV configurations [8]

Designing ascent and re-entry vehicles (ARVs) could have arduous challenges, such as reconciling the performance requirements of the ascent phase with the vehicle's ability to decelerate during re-entry, considering the flight through different Mach regimes ($0<M<30$), and withstanding thermal loads over extended flight periods. Moreover, it is necessary to install a propulsion plant that provides the required thrust across different altitudes, enabling the vehicle to ascend and access space with a considerable carryed payload [9]. The main problem with single-stage to orbit is that the entire empty mass of the vehicle must be placed in orbit, and, as a consequence, the payload fraction, i.e. the payload weight compared to the gross take-off weight, results in a very low value. To reduce this operational constraint, the research and development centers are currently working on engine configurations that can guarantee high performance reducing propellant consumption during ascent. That, the selection of engine types and their operational modes and consequently the integration between the airframe of the vehicle and the engine, hold fundamental significance.

1.2.3 Thesis Objectives

Upon establishing the domain and thus delineating the design parameters within which the thesis operates, the methodology development starts as the primary framework for assessing conceptual feasibility and formulating a solution space of possible design concepts for the high mission requirements from the beginning of the design process.

Space agencies such as ESA could be strongly interested in the project since there is little information in the literature regarding design methodologies for this type of vehicle.

The thesis objectives are:

1. Research and assess the relevance of current aerospace vehicle design methodologies and SSTO HTOL concept designs documented in the literature.

2. Identify methodological concepts that lead to a design framework for an SSTO HTOL.

3. Research analytical methods for evaluating vehicle performance and initiate a statistical analysis based on the creation of a comprehensive database that will serve for the dedicated SSTO HTOL design knowledge-based system.

4. Create a design methodology and algorithms for the conceptual design phase of SSTOs HTOL.

5. Apply the methodology and the developed tool to the case study of the SKYLON.

As an additional objective, a graphical user interface developed in Matlab environment could be integrated, enabling users to access and utilize it easily and swiftly. The methodology developed will be not suitable for the development of two-stage-to-orbit concept designs due to significant operational differences.
This thesis work is part of a project where other two master's degree thesis are involved. The Figure 1.5 shows the organisation chart of the project, i.e. how the development work of the methodology and the conceptual design tool is coordinated.

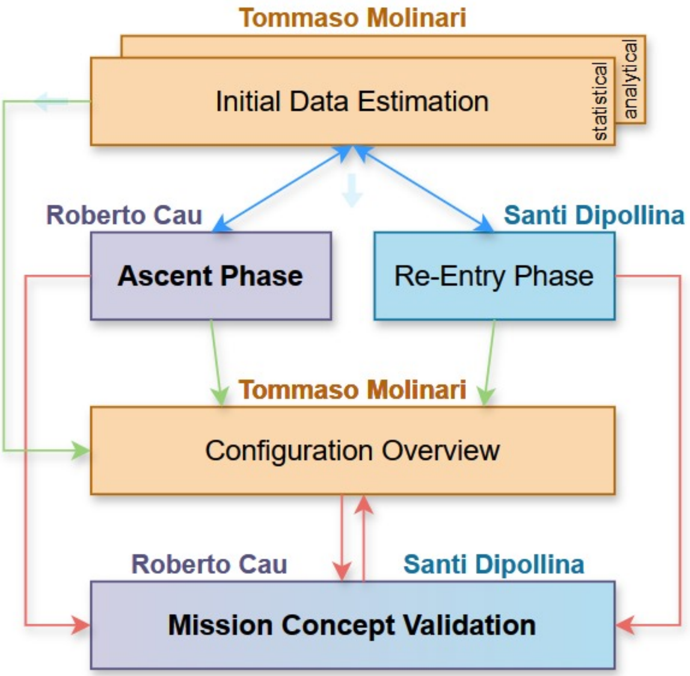

Figure 1.5: Project Organization Chart

1.3 Research Outline

In Chapter 2, a literature review is presented for the SSTO HTOL case study. This review examines both failed SSTO HTOL projects and those currently in the developmental phase, as well as potential propulsion strategies and suitable materials for thermal protection systems, allowing the creation of dedicated databases and the development of statistical analysis. A crucial step involves reviewing contemporary methodologies for aerospace vehicle design, as it allows us to assess the effectiveness, efficiency, and suitability of existing approaches in addressing the SSTO HTOL conceptual design.

Chapter 3 details the methodology development, starting from the initial requirements and progressing to the final design configuration. This process involves integrating the design space determined by the multiple matching chart with the vehicle sizing procedure. The sizing methodology facilitates an evaluation of volume feasibility.
In Chapter 4, a case study is identified to verify the methodology and tool validity. SKYLON is one of the most current examples of a reusable single-stage to orbit with orizzontal take-off and landing. The information obtained regarding this vehicle is compared with the results obtained through the created tool.
In Chapter 5, Conclusion and possible future works are reported.

Chapter 2

Literature Review

2.1 Review of Aircraft Design Methodologies

The design process is long and complex, involving high costs, especially for the development of unconventional vehicles, and significant risk factors. It is therefore necessary to organize the design process into clear and coherent phases using a synthesis methodology that provides a logical design sequence to address complex aerospace vehicle systems. Design synthesis systems are the foundation on which aerospace vehicle design organizations such as Boeing, Airbus, Lockheed Martin, etc. are based. Generally, the methodology considers the interaction between different disciplines and includes analysis methods and techniques used in the design phases. The design synthesis of a complete aerospace vehicle varies critical design parameters to achieve a feasible and functional design, called the 'converged' design due to the iterative computational approach.

In this section of the literature review chapter, some non-integrated/manual conceptual design methodologies for access to space vehicles are mentioned and reported as flow charts. It is necessary to specify that many synthesis systems are developed in-house and are therefore not accessible. Additionally, in this thesis work, source codes for detailed evaluation are not provided. Nevertheless, it has been found that the number of design methodologies for reusable access to space vehicles in the literature is much lower compared to the sources available for the design procedure of conventional aircraft. Therefore, this chapter section aims to provide a fairly comprehensive overview of the state of the art of major design synthesis, highlighting their general design philosophy and some basic specifications of the various procedures.

The methodology behind ASTRID-H, a conceptual design tool for high-speed vehicles developed at the Polytechnic of Turin, is also mentioned.

Spacecraft Design methodology by K.D. Wood [10]

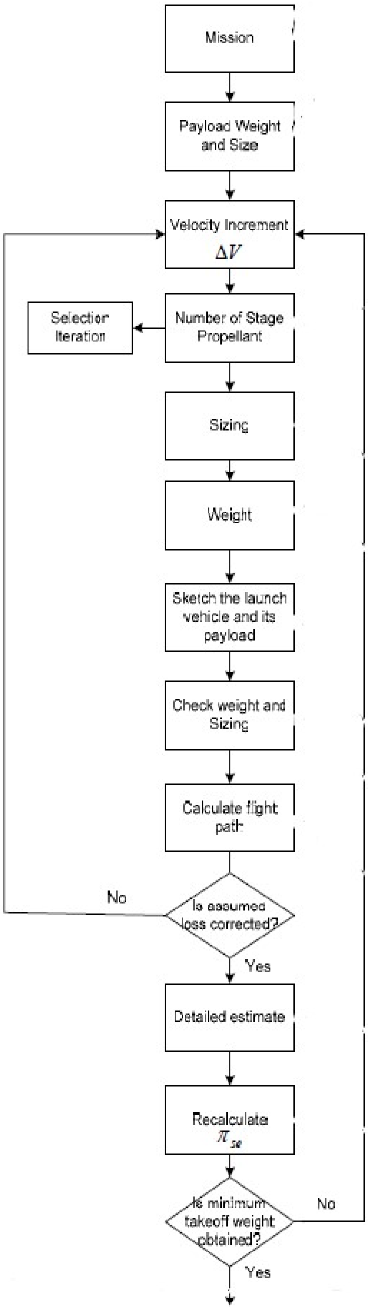

Figure 2.1: Synthesis flow chart

While specific details may vary, especially considering advancements in technology and methodologies since its publication in 1964, the book likely covers fundamental principles and approaches relevant to spacecraft design at the time. The design process begins with the mission selection and specification, that should state where the spacecraft is to go and what it is to do. The next step is to estimate payload weight and size to perform the mission, including instruments to measure, guidance and control equipment, communications equipment, and propulsion equipment for correcting navigational errors. Then estimate velocity increment for the mission: first, calculate the ideal velocity increment based on the principles of space flight mechanics, then estimate the gravity and drag losses including allowance for the offsetting gains due to the earth's rotation, and add them to the ideal velocity increment to estimate the total ΔV. At this point a selection of a number of stages and kinds of propellants for each stage is performed. This selection is of necessity tentative and will have to be repeated several times to get near to a minimum weight of minimum cost launch vehicle to fulfill the mission. Existing launch vehicles and launch vehicles currently under development are usually a good guide to a first choice of the number of stages and kinds of propellants. The process then continues with the sizing procedure, that includes a preliminary estimate of structure and equipment weight, by estimating π_{se} in the region of the current or projected near future stage of the art. Thus, the initial weight and size for each stage of the launch vehicle are calculated.

At this point you can sketch the launch vehicle and its payload approximately to scale, check the weights and sizes by other methods in which the structure weight is a function of the propellant weight, and calculate the launch flight path to orbit and verify the assumed gravity and drag losses. If assumed losses were not substantially correct start over again the velocity increment estimation. Then, a detailed estimates to verify the assumed value of π_{se} is required, including weights of powerplant, structure and other equipment, and recalculate it for each stage until the detailed weight estimate agrees with the assumed value. The process must be repeated varying each assumed value by a small amount until a minimum takeoff weight is obtained for each proposed combination of stages and propellants and select a minimum cost combination for the available alternatives.

Hypersonic Air-breathing Vehicle Design methodology by J.L. Hunt [11]

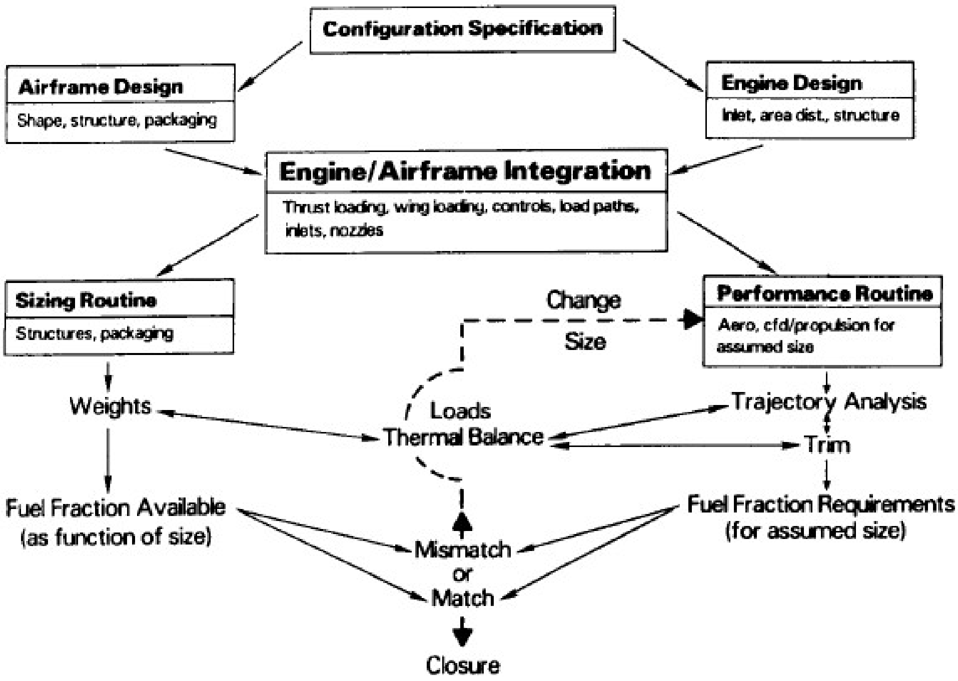

Figure 2.2: Methodology for vehicle design synthesis by Hunt

The design process refers to hypersonic accelerators and cruisers, with similar analytical tool requirements. The inlet area and in turn propulsion/airframe integration will be the dominant factor in shaping the vehicle configuration. First, the airframe shape, engine flow path, and area distribution are defined. Options on fuselage structural design, substructure, and materials are considered along with internal packaging arrangements. Engine/airframe integration is the center of the design process. Here load paths throughout the vehicles are optimized with particular emphasis on the synergistic transfer of the thrust load from the engine to the airframe inlet and nozzle contours are laid out.

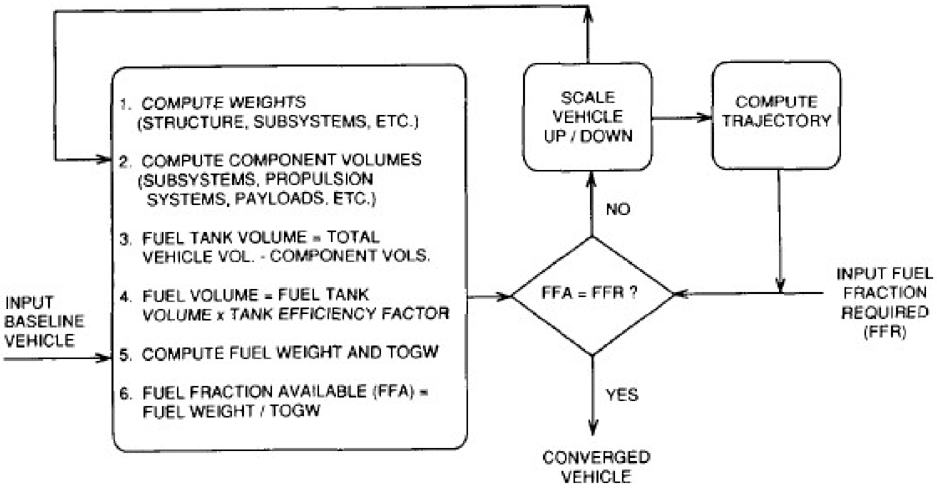

Figure 2.3: Vehicle sizing procedure by Hunt

The sizing routine requires scaling relationships for the vehicle subsystem and structure. Subsystem weights are based on a technology enhancement extrapolation of historical algorithms. the scaling relationships are based on vehicle length, gross weight, and applicable areas such as inlet or control surfaces. Structural weights are generally based on historical databases. The performance routine is a trajectory code, whether a simple energy state integration approach or a three-degree-of-freedom dynamic version. Aerodynamic and propulsion performance are the required inputs. With this aero/propulsion performance set, the fuel fraction required to perform the ascent, orbital insertion/circularization, and deorbit is determined from the trajectory analysis. Iterations are now required to adjust the structures/insulation for the optimal ascent and descent trajectory and vice versa and to perform an iteration on size/weight in the performance routine. The closure of the synthesis process is in terms of fuel weight fraction required and fuel weight fraction achievable as a function of gross weight for an airbreather ascent to orbital conditions and return with a fixed payload, the closure point is where two curves cross. The fuel fraction required line is nearly independent of gross weight, however, as the vehicle is scaled up geometrically, the increase in wing loading and resultant drag due to lift induces a slight positive slope. The achievable fuel fraction curve increases significantly with gross weight, until the negative influence of size on structural efficiency becomes too high. Increasing the thrust margin and/or degreasing the vehicle's weight for a given velocity increases the instantaneous energy imparted to the vehicle, thus it reduces the fuel fraction required.

Hypersonic Vehicle Design methodology by Czysz [12]

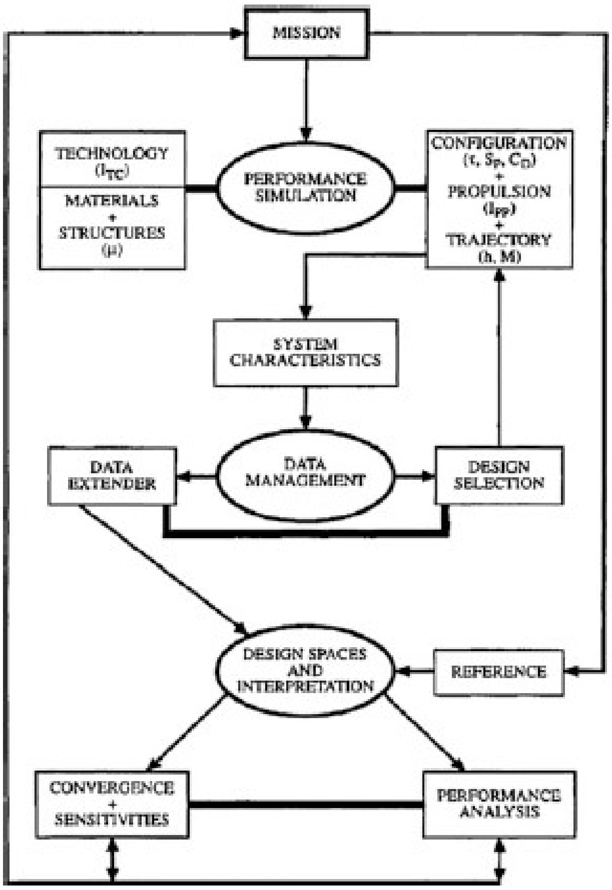

Figure 2.4: Methodology for vehicle design synthesis by Czysz and Murphy

The methodology for hypersonic and space launch vehicle convergence presented here is illustrated in Fig. 2.4. It is assumed that data sets on capabilities in propulsion, fuels, materials, and industrial manufacturing, have been generated, based on experience and extensions as well as on predictions from sizing programs. The propulsion performance index serves as a measure of the efficiency of the propulsion system. The structural index instead is defined by the product of three factors about configuration concept and slenderness, propulsion, propellant and aerodynamics, and payload and vehicle size. In general, the industrial capability index is a product of two factors, one related to the configuration concept and the other to the payload and vehicle size and geometry. Considering the mission requirements, a reference vehicle is hypothesized and characterized by carefully selecting essential parameters. The vehicle configuration concepts consider four reference shapes: blended body, winged body, waverider, and the right circular cone. The propulsion-propellant concepts consist of various types of combined-cycle engines, all-rocket engines and all-airbreathing engines. Then, a series of design spaces are constructed using these key parameters. Convergence to a vehicle design is sought based on the influence of these parameters on vehicle performance as calculated and plotted on the design spaces. The reference vehicle can be varied based on characteristic parameters in the design space. Actual engineering choices require interpretation of the design spaces. A design space is a parameter space of converged vehicles; it may involve two or more individual parameters or groups of parameters. In general, it is a multi-dimensional (multi-disciplinary) representation, but for practical reasons is shown on a two-variable plane, and any other variable is used as a parameter.

Space Transportation Systems Design methodology by W.E. Hammond [13]

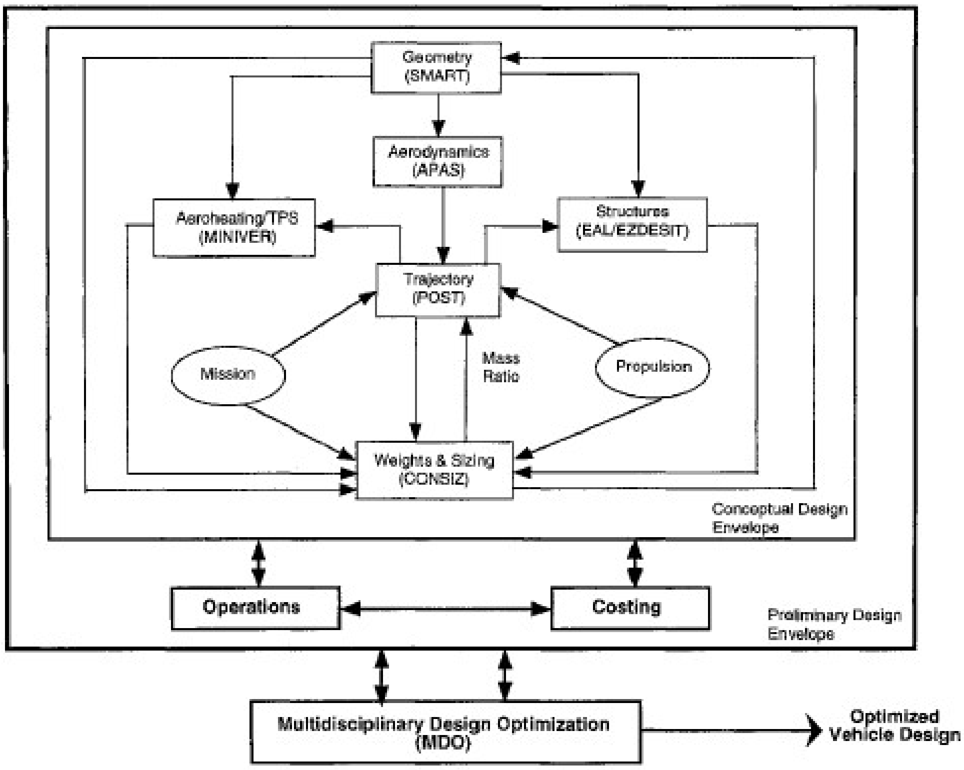

Figure 2.5: Methodology for vehicle design synthesis by Hammond

The first step in the design process is the statement of the problem, then developing the mission and vehicle requirements. Next, the actual design of a particle concept should be generating the vehicle geometry. SMART is a highly interactive program for generating aerospace vehicle geometries and interfacing them with an assortment of analysis tools. The program calculates the area, volume, c.g., and moments of inertia for any component or group of components. The first step after generating a geometric description of the initial design is to calculate the aerodynamic characteristics. ASAP calculates pressure distribution as well as force and moment coefficients for the configuration in the total speed range from subsonic to hypersonic. Once the aerodynamic characteristics have been determined, the components' weight is assumed for the initial trajectory analysis with POST. POST is used to analyze launch, on-orbit, and reentry trajectories subject to constraints, such as maximum acceleration, heating boundaries, and crossrange requirements. The principal results include propellant requirements for input to weights and sizing calculations and inflight conditions used by aeroheating analysis. The aeroheating calculation can be done using the MINIVER program, a simple engineering code that computes postshock and local flow properties as well as heating rate values based on perfect gas or equilibrium air chemistry. The structure analysis is a multi-step process. Using the SMART output, generating a detailed grid, mapping the aerodynamic loads, and taking into account inertial loads from POST, the stresses in the structure are calculated in PATRAN and sent to EXDESIT which determines the required thickness and weight of each skin panel. The results are used to enrich the approximate weights and sizing techniques in CONSIZ as well as to indicate areas of the vehicle that might require redesign. CONSIZ takes the propellant requirements, the overall vehicle/mission requirements and geometric information and calculates the weight of each component, the total weight, and the c.g. of the vehicle. outputs include a listing of vehicle parameters, such as length, wing span, volume, etc. In addition, the new size of the vehicle is iteratively fed back to SMART so the geometric representation can be adjusted. At this point, an iterative loop is usually established with SMART, APAS, POST and CONSIZ, which converges on a design concept that is used in the more detailed analyses.

ASTRID-H methodology by D. Ferretto, R. Fusaro, N. Viola [14]

ASTRID-H is a software tool developed at the Politecnico di Torino to support the design of hypersonic vehicles, ranging from initial data estimation to defining a design space, identifying the feasible design point, and sizing the vehicle. The tool was not intended to be applied to the design of access to space vehicles. However, the integrated multidisciplinary methodology can be adapted to the case studies at hand and presents the peculiarity of using the Multiple Matching Chart to partition the feasible design space into the various mission phases that a high-speed vehicle must undertake. The concept of the Multiple Matching Chart will be detailed in section 3.6 of Chapter 3.

Only the process aimed at conceptual design, called 'Layer 0', is interesting for our case study, without considering the interactions with the preliminary design layer of the subsystems, that are present in the methodology due to the need for a high level of integration between the airframe and the subsystems most impacting the configuration and sizing of the vehicle. This specific integration requirement for high-speed vehicles already imposes a strong limitation on the use of a conventional methodology applied to aircraft, which keeps the design phases in separate blocks. Additionally, the methodology on which the ASTRID-H tool is developed provides for designing the vehicle with a multi-fidelity level characteristic, offering the possibility of using models of varying accuracy levels in different design phases, according to the user's needs.

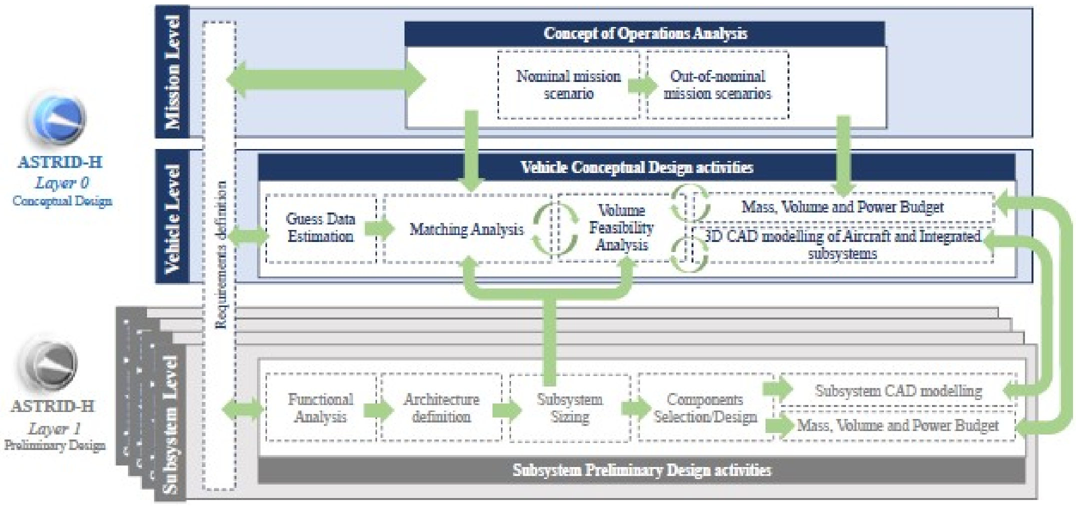

Figure 2.6: ASTRID-H Architecture

The Conceptual Design Module consists of five interconnected routines that complement each other: the Guess Data Estimation Routine, the Matching Analysis, the Volume Feasibility Analysis, the Mass and Volume Breakdown, and the 3D CAD modeling of the aircraft. The first routine is based on two algorithms that respectively provide a statistical analysis of high-speed vehicles and an estimation of masses using semi-empirical models. The Matching Analysis and the Volume Feasibility Analysis take preliminary guess data as input and define, following the implementation of a sizing algorithm and the multiple matching chart, the design point and verify that the obtained value is within the feasible design space. Once convergence is reached, the Mass and Volume Breakdown routine is initiated, which calculates the masses and volumes of the main components.

2.2 RLV SSTO HTOL - Research

2.2.1 Hystorical Background

In December 1931, the American rocketeer Robert Goddard published in a popular science article a description of a spaceplane, called a "stratosphere plane", with elliptically shaped wings as an aircraft, and propelled by a combination of air-breathing and rocket engines. This was one of the first spaceplane concepts ever made [15]. In this configuration, the rocket engine allowed the thrust out of the atmosphere, while, inside the atmosphere, two turbines positioned along the thrust stream of the rocket were rotated to drive two large propellers on either wing, which provided the power required by the vehicle. Spaceplane concepts remained fictional until 1957, when the Air Force launched the Aerospaceplane program, which aimed to develop a single-stage-to-orbit vehicle propelled by an air-breathing engine. By 1959, the project led to the development of a Recoverable Orbital Launch System (ROLS), an SSTO design with horizontal take-off capable of reaching a 300-mile-high orbit. The ROLS propulsion system allowed not to carry on board the oxygen needed as an oxidant, but to obtain it from the air collected during the flight, compressed, liquefied, and distilled, which would then be mixed with the liquid hydrogen before entering the engines. In 1962, due to uncertainties arising regarding the single stage to orbit design, the Air Force decided to shift the focus to Two-Stage-To-Orbit (TSTO) concepts. However, following the program's criticism by the Scientific Advisory Board, the Aerospaceplane project was terminated in 1963. Fiscal 1964 funding was cut by Congress, and the Pentagon opted against advocating for its reinstatement.

Star Raker

The concept design idea of an SSTO HTOL (Single-Stage To Orbit with Horizontal Takeoff and Landing) originated from the need of The North American Rockwell to deliver into Low Earth Orbit (LEO) two satellites of 35,000 metric tons each year, following studies related to the Satellite Power System (SPS) in the late 1970s. Considering a payload of 91 metric tons per launch vehicle, 770 flights per year are required. To meet this requirement, the launcher must have operational availability similar to that of a commercial aircraft. Using instead conventional Super-Heavy Launch Vehicles with a payload capacity of 400 metric tons, the frequency of flights requested every year drops, but refurbishment, stacking and launch pad cycle times remain very severe scheduling constraints. A configuration known as the Star-Raker was therefore developed [16]. The vehicle is completely reusable with a rapid turnaround and has the capability to ferry between airfields. It must meet the operational requirement of reaching a Low Earth Orbit (LEO) at 300 nautical miles [555,600 km], 28.5 degrees inclination from any launch site with a runway length ranging from 8,000 to 14,000 feet [from 2,438 to 4,267 m], and in particular, deliver 196,600 pound [89,176 kg] to that target orbit starting from the Kennedy Space Center. The Gross Takeoff Weight (GTOW) achieved is 5,000,000 lbs [2,267,961 kg] and to reach the required thrust for the mission, ten hydrogen-powered turbofan/turbo-air exchange/ramjet engines are installed, each with 140,000 lbf [63,503 kg_f] of thrust. The engine design will be based on the axial-flow turbojet GE CJ805, the turbofan-ramjet P & W SWAT 201, the Aerojet Air Turborocket, the variable throat nozzle Marquardt, ramjet engines, and tubular-cooled rocket engines Rocketdyne. Beyond the minimum atmospheric density threshold for convenient use of airbreather engines alone, three hydrogen-powered rocket engines are activated, each with 1.06 million pounds [480,808 kg_f]

of thrust and an I_{sp} of 455 seconds. Once 7,200 fps [2,195 m/s] is reached, the airbreather engines are shut down.

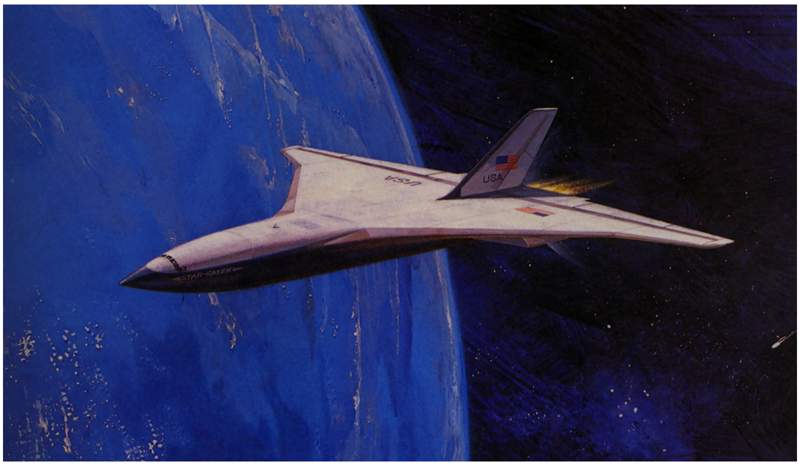

Figure 2.7: Star Raker artist's concept

Boeing/Langley SSTO

In 1977 Boeing designed a single stage to orbit concept at the request of The Hypersonic Branch of the Langley Research Center (LaRC) Lasked General Research Corporation (GRC), in order to evaluate the feasibility of using fully reusable two-stage launch vehicles incorporating airbreathing propulsion [17]. This conceptual SSTO horizontal takeoff design is fully reusable and lands horizontally in either a manned or unmanned mode. As an operational design requirement, it has the minimum liftoff weight with a 30,000-kg payload delivered to a 93 x 185 km, 28O orbit, placed in a payload bay sized like that of the shuttle. The vehicle employs a rocket sled for horizontal takeoff, which not only reduces the weight of the landing gear but also enables an optimal thrust-to-weight ratio of 0.7. This ratio is significantly lower than what would be required for a potential vertical takeoff, typically around 1.3. The estimated GTOW is approximately 1250 metric tons, of which only 14 percent remains as landing weight. A modified version of the space shuttle's main engines is used to provide a vacuum thrust of 2.65 NM.

Figure 2.8: Boeing SSTO artist's concept

NASP X-30

The National Aerospace Plane was intended to be a revolutionary step forward from the space shuttle. In the State of the Union speech of 1986, President Ronald Reagan declared the intention to develop "a new Orient Express that could, by the end of the next decade, take off from Dulles Airport and accelerate up to 25 times the speed of sound, attaining low-earth orbit or flying to Tokyo within two hours" [18]. To fulfill the US President's promise, the vehicle would be both a high-speed aircraft and a single-stage-to-orbit vehicle, powered by innovative air-breathing engines. The NASP program was initially intended to design and build two vehicles, the X-30, of which at least one would have to meet the requirement of reaching orbit in a single-stage configuration through the atmosphere at a maximum speed of Mach 25 [19]. The X-30 would employ a multicycle engine that transitioned during the ascent from jet to ramjet and scramjet operative modes, burning liquid-hydrogen fuel with oxygen captured from the atmosphere and cooled until liquefied. Both the engine and vehicle designs were crafted by Tony DuPont, an aerospace designer who had developed a multicycle jet and rocket engine initially under contracts with NASA, and later with ARPA. DuPont's vehicle design was built upon several questionable assumptions and optimistic interpretations of results, also including omissions (such as landing gear) for convenience. Following the end of the Cold War, NASP suffered substantial funding cuts, until the program was canceled by Congress in 1992. Although the program never came close to building the aerospaceplane or even flight testing, NASP contributed significantly to the development of materials resistant to high temperatures over repeated periods, which are needed on the vehicle's nose and body, and materials capable of tolerating repeated exposure to very low temperatures, as is the case with cryogenic fuel tanks.

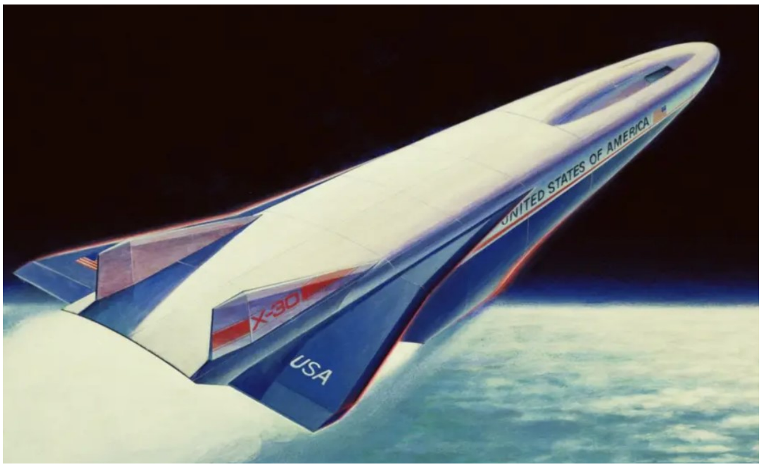

Figure 2.9: X-30 artist's concept

Tupolev Tu-2000

The Soviet project to develop the Tupolev Tu-2000 commenced in 1986 as a response to the US Rockwell X-30 project, which was mentioned previously. In that year, the Ministry of Defence of the Soviet Union released a technical specification for a single-stage reusable aerospaceplane. Designs submitted by Tupolev, Yakovlev Design Bureau and NPO Energia were examined, and the former received approval for the project. Three versions were planned: a Mach 6 test vehicle, which was under construction at the cancellation of the program, a Mach 6 intercontinental bomber, and a single-stage-to-orbit launch vehicle. The Tu-2000 reusable space launcher version would have weighed 260 metric tons at lift-off and reached Mach 25 needed to match orbital velocity. An 8 to 10-metric-ton payload would have been delivered to a 200 km orbit. The configuration concept included the installation of 8 turboramjets for the airbreathing phase, supported by a rocket engine to achieve the orbit. After the dissolution of the Soviet Union, the Russian Federation continued its efforts in developing the project until 1992, when it was forcibly suspended due to lack of funds.

Figure 2.10: Tupolev 2000 artist's concept

HOTOL

The development of a single stage to orbit with horizontal take-off took inspiration from the research conducted by British engineer Alan Bond in the field of pre-cooled jet engines. The HOTOL program was begun in 1982 by British Aerospace (BAe) and Rolls Royce led by John Scott and Dr Bob Parkinson. The progress of the project was quite well advanced by the time the British government withdrew further funding in the mid-1980s, reaching the detailed engine design and mockup phase. HOTOL, with a GTOW of 275 tons, would have taken off horizontally from any runway that could handle a Boeing 747 or Concorde-sized craft, using a rocket-powered sled to reach quickly its launch speed of 330mph [20]. From there, the main engine would provide thrust in air-breathing mode until the launch vehicle achieved a height of around 26-32km. Then, it would transition to pure rocket propulsion at Mach 5.0 - Mach 6.0 for the HOTOL's ascent to orbit. HOTOL was thus designed to incorporate a unique air-breathing engine, the RB545, also known as Swallow, that was under development by British engine manufacturer Rolls-Royce. This engine would be fed by a propellant consisting of a combination of liquid hydrogen/liquid oxygen. The resulting vehicle configuration would feature the possibility of deploying a 7-ton payload to LEO orbit or launching lighter payloads into geostationary orbit with the help of a perigee engine. Implementing a moderate re-entry profile would alleviate the thermal loading constraints. HOTOL would then perform a glide phase, eventually landing on a standard runway. In 1989, the British Government withdrew its funding due to austerity measures regarding public spending. The program was later declared suspended and the engine was classified as top secret, leaving no possibility of seeking foreign investors.

Figure 2.11: HOTOL artist's concept

Japanese Spaceplane

Concurrent with the American NASP project, Japan's NAL was engaged in developing a spaceplane following the requirements reported below: with a takeoff weight of approximately 386 tons, the vehicle will carry crew members and payload totaling 20 tons into orbit up to 570 km [21]. The propulsion system is intended as a combination of airbreathing and rocket engines. The chosen design is a Single-Stage-To-Orbit (SSTO), and the work on the project was scheduled to launch a prototype by 2006. In this direction, a cooperative consortium of industries and institutions presented a conceptual study that forms the basis for the state's program. The total takeoff weight was calculated to be 350.8 tons, and a wingspan of 24.68 meters was achieved. The spaceplane would have used small canard surfaces just behind the nose in addition to this configuration. Apart from this configuration, three major industrial groups have reflected on a solution to propose. In particular, three designs were developed: Mitsubishi, Fujl, and Kawasaki, which have slightly different dimensions, such as vehicle length and wingspan. Scramjet and rocket engines were chosen for propulsion so that the vehicle can operate in all different mission environments (atmosphere and space). The engines would have used a combination of liquid hydrogen and liquid oxygen as propellant.

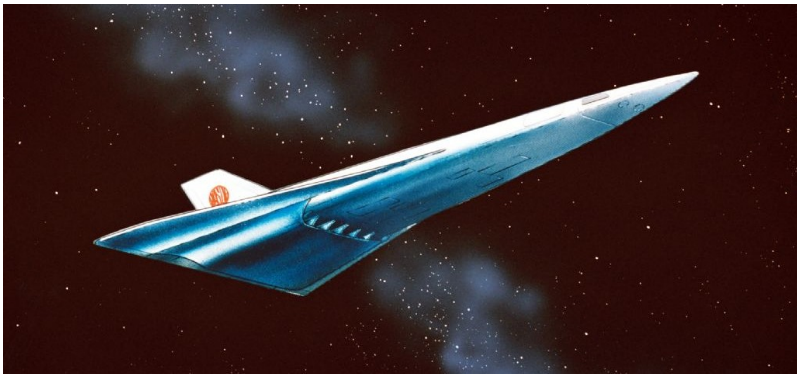

Figure 2.12: Japanese Mitsubishi Spaceplane artist's concept

2.2.2 Current Projects

In this section, ongoing projects for SSTO configurations are outlined. It's possible that some of these projects are currently on hold or significantly delayed compared to the planned schedules.

SKYLON

To resume the development of the British HOTOL project, the UK-based company Reaction Engines Ltd. was founded by Alan Bond, John Scott-Scott, and Richard Varvill in 1989, storing all the knowledge gained from the erased state program and with the focus on developing the technology, particularly the precooler. HOTOL SSTO/RLV renamed SKYLON. Thanks to private investment, offices and laboratories have been used at Culham Science Park (AEA site) since 2000 [22]. SKYLON is an SSTO spaceplane fully reusable with horizontal take-off and landing on a standard runway like a conventional aircraft. The vehicle utilizes SABRE engines, mounted in nacelles on the wingtips. They work as airbreathing engines as well as rockets, enabling the aircraft to operate inside the atmosphere and in space. Taking as reference the takeoff weight of 275 tons of the HOTOL, the first configuration, Skylon C1, was developed with a payload capacity of 12 tons in LEO. To meet market demands, the payload had to be increased to 15 tons, thus designing a scaled-up version of the initial configuration, the SKYLON C2 configuration, with a takeoff weight of 345 tons. Following technological development and studies on the engine cycle, the final design was defined in 2010, as the SKYLON D1 configuration.

Figure 2.13: SKYLON artist's concept

AVATAR/Hyperplane

AVATAR or Avtar, which stands for 'Aerobic Vehicle for Advanced Trans-Atmospheric Research', was first announced in May 1998 at the 'Aero India 98' exhibition held at Bangalore. During the past year, it has progressed becoming a more practical Reusable Launch Vehicle with military applications. Avtar is a reduced-scale version of the first 230-ton Hyperplane that India promoted in the early 1990s but later canceled due to excessively high costs. The primary characteristic of the "Hyperplane" design concept was its geometric scalability, allowing for the construction of a vehicle that weighs 25 tonnes at the lift-off (comparable to that of an advanced fighter aircraft). This might be the smallest feasible weight for a reusable SSTO spaceplane, enabling the release of 1 ton of payload into parking orbit at Mach 26. A small-scale Flight Technology Demonstrator has also been designed. The team working on this project includes scientists from DRDO and a Hyderabad-based company CIM Technologies. In early July 2001, the project was publicly announced in the United States by retired Air Cmdr Raghavan Gopalaswami [23]. Gopalaswam said the idea for Avatar originated from the Rand Corporation of the United States publication in 1987. Avatar takes off horizontally from a runway and uses a combination of turbofan, ramjet, and scramjet engines to reach a cruising altitude of 10 km. At that point, the propulsive transition occurs, and a cryogenic rocket engine provides the thrust needed to reach space. Once the mission is over, it deorbits, re-enters the atmosphere, and lands with the help of its engine like a conventional airplane. A single AVATAR can perform approximately 100 such missions, thus allowing a total of 100 tons of payload to be delivered into space. AVATAR/hyperplane was designed so that approximately 60 percent of its gross take-off weight is due to the transport of liquid hydrogen. This was possible considering the ability to collect the air from outside at high speeds with simultaneous oxygen liquefaction and onboard storage and use it to fuel the rocket engine. In this way, no oxygen is stored at take-off. It must be taken into account that the spaceplane almost doubles its mass in hypersonic flight due to this self-refueling process.

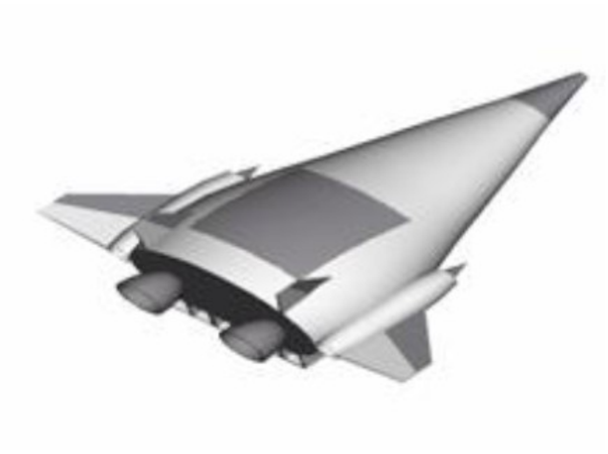

Figure 2.14: AVATAR/Hyperplane model concept

Radian One

Following a funding round of 27.5 million dollars in January 2022, the company Radian Aerospace, founded in 2016 and based in Bellevue, Washington, is seeking to develop and produce the Radian One [24]. Radian One is a single-stage-to-orbit fully reusable vehicle with runway takeoff and landing. The vehicle is designed to be manned (crew of 5 people) and to take up 5,000 pounds [2,268 kg] of cargo into orbit and reach any point on the Earth's surface in less than an hour. The vehicle is expected to have a return cargo capacity of approximately 10,000 pounds [4,536 kg]. Its configuration is similar to an aircraft, allowing for less infrastructure than vertical launch systems and ensuring possible turnaround within 48 hours. Radian One takes off subsonically with full propellant tanks from a rocket-powered sled. It then proceeds with a low-G ascent to low Earth orbit (LEO) to maintain crew safety and comfort during the flight. Once the suitable altitude is reached, Radian One is capable of entering space thanks to the thrust of three liquid-fueled rocket engines. Development of the cryogenic-fueled engine is already at an advanced stage, as Radian CEO Richard Humphrey said the first "full-scale" engine has been built and tested [25]. At full power, it will have a thrust of about 200,000 pounds [90,718 kg]. Once the mission and re-entry phase are completed, thanks to its winged configuration, it lands smoothly on any 10,000ft [3,048 m] runway.

Figure 2.15: Radian One artist's concept

Suborbital Spaceplane: Ascender and Lynx Mark III

This type of vehicle does not allow for reaching altitudes beyond about 100 kilometers, making them suitable for point-to-point missions, suborbital tourism, or deploying self-propelled payloads at very low orbital altitudes. Despite this, they feature configurations very similar to horizontal takeoff and landing single-stage-to-orbit vehicles.

Ascender is a small sub-orbital spaceplane under development by the company Bristol Aerospace [26]. The vehicle is designed considering the use of existing technology, minimizing development costs and risks. This approach aims to make the spaceplane appealing in the market, attracting investments from the private sector. Ascender can carry a pilot and a passenger, or be used for onboard experiments. It takes off horizontally from a standard airfield using its turbo-fan engine, followed by a phase of subsonic ascent up to an altitude of 8 km. Then the pilot ignites the rocket engine, allowing the vehicle to ascend rapidly until it reaches an altitude of 100 km. The maximum speed achievable during the ascent is approximately Mach 3. Due to the historically demonstrated greater development simplicity of rocket engines using hydrogen peroxide (HTP) compared to those using liquid oxygen (LOX), it was chosen to use HTP as the oxidizer in the propellant mixture. The technology required for the rocket engine was developed in the UK during the early 1970s. The aerodynamics, structure, and systems are all derived from existing airplanes or launchers and utilize well-established materials. The concept is instead innovative, assuming a shape similar to that of a lightweight aircraft suitable for hypersonic flights, fitted with a rocket motor.

The Lynx is a two-seat, piloted space transport vehicle designed by XCOR for the commercial reusable launch vehicle market [27]. It is capable of horizontal takeoff from a runway, transporting humans and payloads up to 100 km in altitude, conducting a suborbital flight of half an hour, and safely returning to Earth to land on the same runway it took off from. Its all-composite airframe makes it lightweight and resistant to stresses. Additionally, to manage the thermal loads during reentry from space, the design includes the installation of a Thermal Protection System (TPS) on the nose and leading edges. The area of the double-delta wing, spanning about 7.5 meters, is sized so that the wing loading during landing allows for moderate touchdown speeds near 90 knots. The length of the Lynx is approximately 9 meters.

The current version of the Lynx has been developed based on previous versions. The initial flight test vehicle is named "Lynx Mark I" and is designed to achieve an altitude of approximately 61 km. The "Lynx Mark II" incorporates identical propulsion and avionics systems as its predecessor. However, thanks to optimization of the dry weight, it offers improved performance, allowing it to be designed to reach altitudes of up to 100 km. The latest version, the "Lynx Mark III," after extensive modifications, represents a significant advancement over the Mark II. In fact, it has the capability to accommodate an external dorsal pod, allowing for the attachment of an upper stage capable of launching small satellites into low Earth orbit or carrying experimental payloads. The external dorsal pod has a maximum payload capacity of 650 kg.

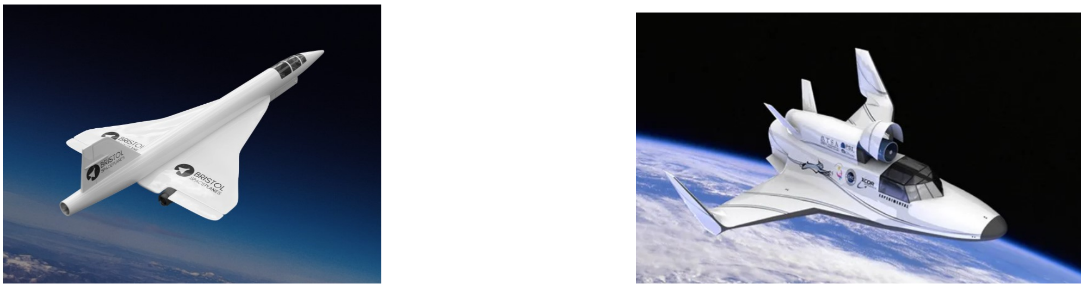

(a) Ascender artist’s concept **(b)** Linx Mark III artist’s concept

Figure 2.16: Suborbital Spaceplane configurations

2.3 Statistical Analysis

The first step in the design phase is to create a database of vehicles to serve as a reference for calculating statistical trends for key characteristics. The database is reported in Appendix A.1.

Since there are currently no horizontal take-off SSTO vehicles, the analysis took into account spaceplanes in the design phase, both discontinued projects and those still under development, with the insertion of some concepts proposed in support of NASA's Highly Reusable Space Transportation study [28][29][30]. Therefore, the statistical trends are based on the configurations entered in the database, and do not provide real or reliable information. The lack of detailed statistical analysis is one of the design problems of this setup, as hypothetical estimates or verifications for case studies cannot be compared to real vehicles. In contrast, conventional aircraft rely heavily on statistical studies by having a wide range of operational vehicle. The trend lines obtained are shown below. Some values obtained by entering the respective graphs will be used both to make a final check with the values obtained through the tool and as possible initial values for the first iterative cycle.

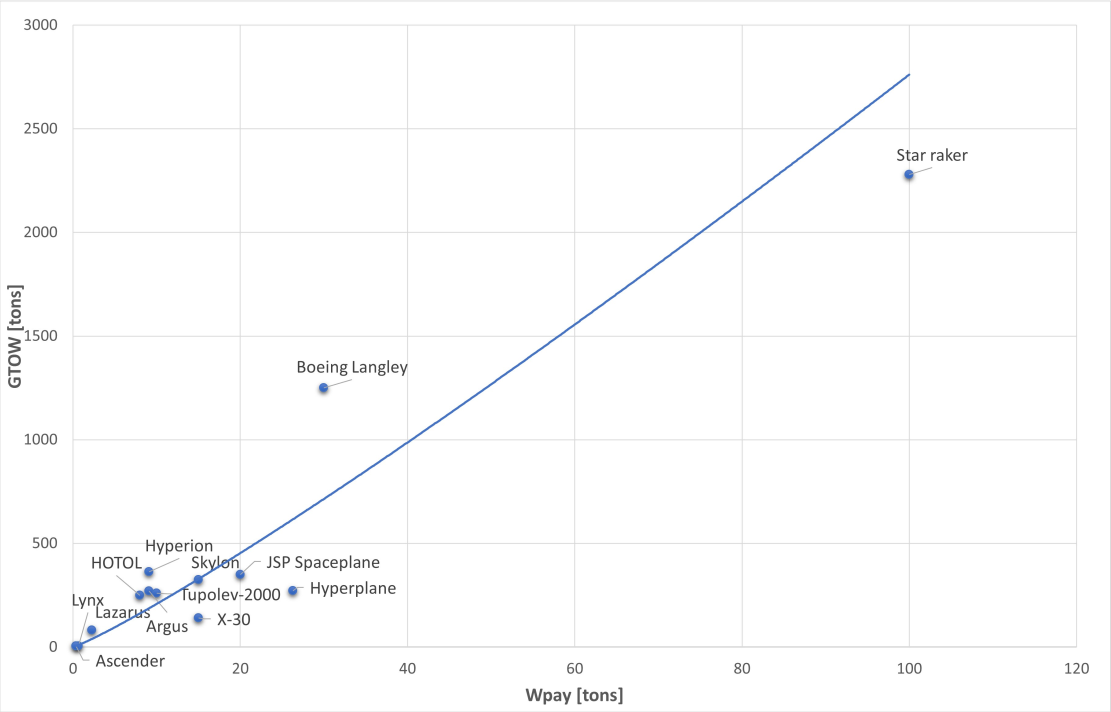

Figure 2.17: Payload Weight vs Gross Take-off Weight

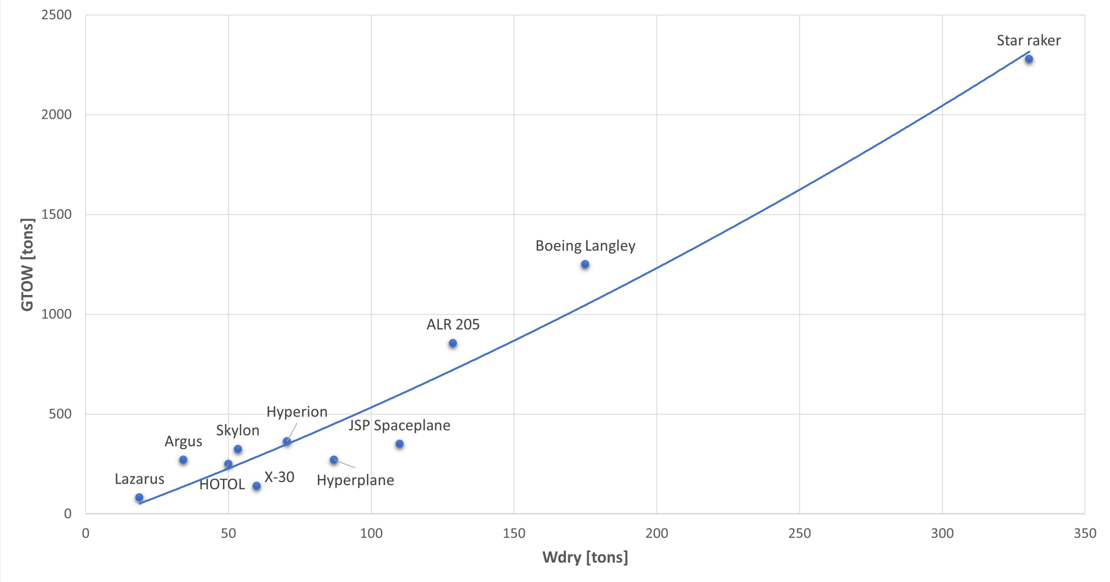

Figure 2.18: Dry Weight vs Gross Take-off Weight

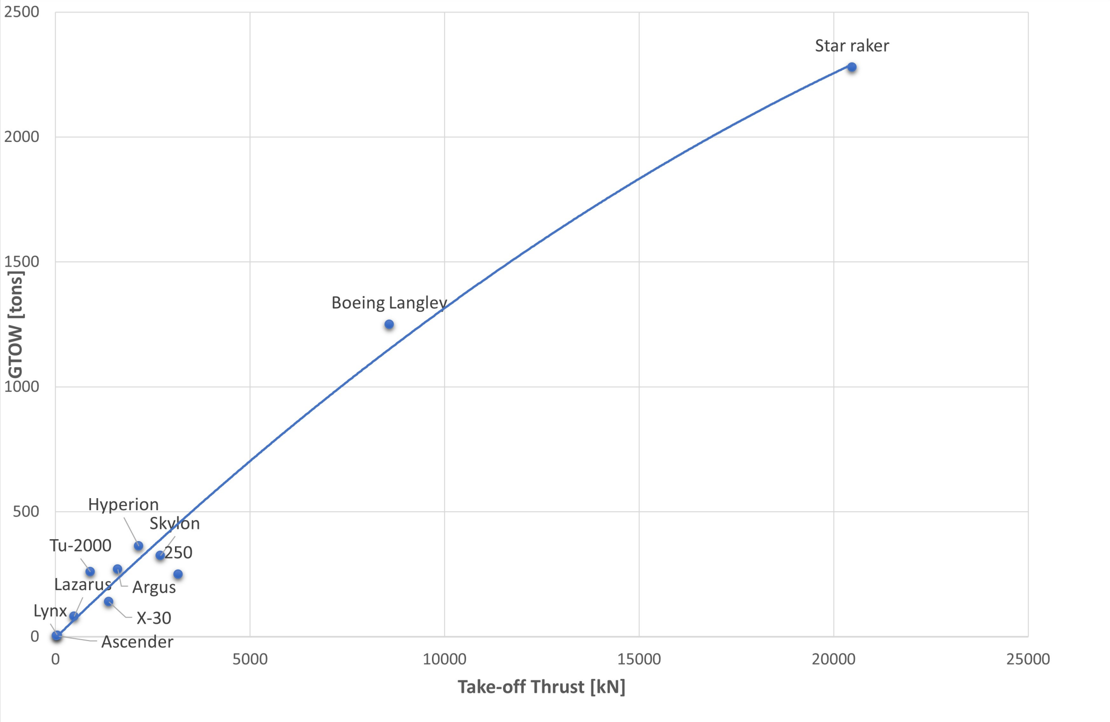

Figure 2.19: Take-off Thrust vs Gross Take-off Weight

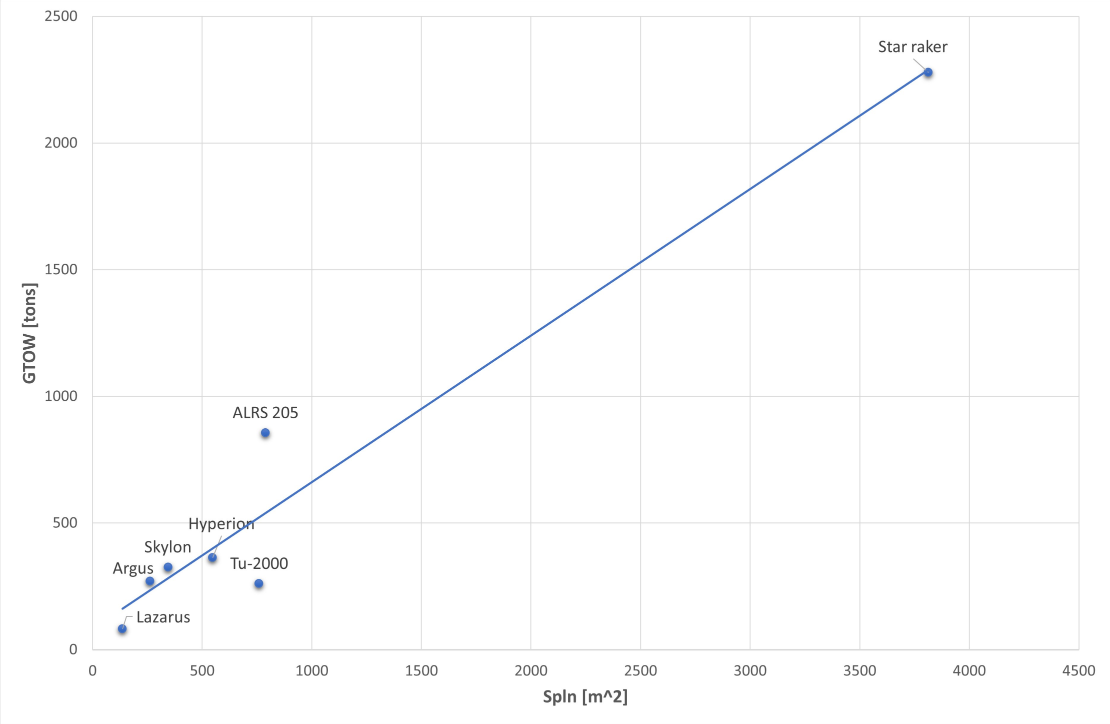

Figure 2.20: Reference Area vs Gross Take-off Weight

2.4 Propulsion Strategies

In this section, various propulsion architectures from the literature are presented, potentially usable for reusable SSTO (Single-Stage-To-Orbit) vehicles [31]. The vast majority of these are still in the development phase or classified as future propulsion strategies, as although some types of engines have been conceived and conceptually designed for decades, the necessary technological support for realization has always been lacking.
Following NASA's program for the development of the X-33, it was understood that the use of a conventional rocket-only propulsion system requires the system to have a structural efficiency that is very difficult to achieve with current technology. A hope for the feasibility of future SSTO vehicles is the development of propulsion strategies that ensure, at least at low altitudes, high specific impulses typical of airbreathing jet engines.

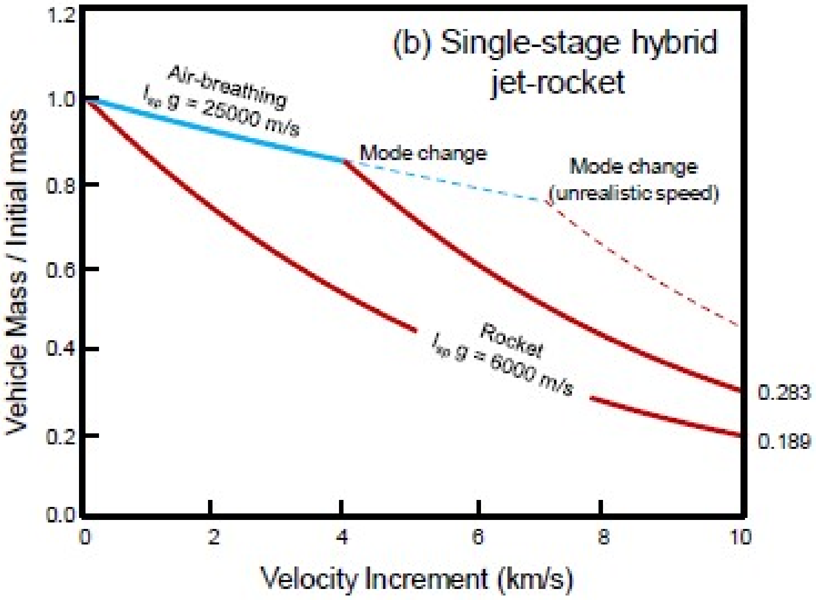

Figure 2.21: Comparison between velocity increments as a function of empty mass for rocket and hybrid systems.

By simply applying the rocket equation, the velocity increment to be imparted to the vehicle at burnout can be derived as a function of the empty mass fraction of the system. In Figure 2.21, the trends for a rocket-propelled vehicle and a vehicle equipped with "hybrid" propulsion are shown [32]. It can be observed that the empty mass fraction of an SSTO (Single-Stage-To-Orbit) vehicle with an airbreathing propulsion phase increases significantly compared to the values reached by the equivalent rocket-propelled system. Nevertheless, the use of this hybrid propulsion strategy brings with it a greater complexity of the propulsion system and an increase in its mass, thus requiring an innovative structural design that overcomes the practical values of current spacecraft. Another aspect to highlight concerns the thrust-to-weight ratio. Considering feasible hybrid propulsion systems, this parameter remains below unity, at least during the airbreathing operation mode, thus requiring a vehicle configuration that ensures a non-negligible lift.
Taking a closer look at the hybrid propulsion strategy, it can be divided into three categories [33]:

1. Combination of multiple individual engines mounted on an aircraft that operate separately in parallel or sequentially. In the case of access to space, a rocket engine is included.
2. Combination of an individual engine, usually a rocket engine, and an engine with more than one operational mode, such as a combined cycle engine.

3. A single combined cycle engine that includes all the operational propulsion modes necessary during the entire flight trajectory. In this case, it is necessary to define the transition between one cycle and another, which can be problematic from an engineering standpoint.

The first combined cycle concepts were developed around 1960 by the Marquardt Company. In general, the combined cycle engines can be divided into two categories: Rocket-Based Combined Cycle (RBCC) and Turbine-Based Combined Cycle (TBCC). From Figure 2.22, the performance trends in terms of specific impulse of a TBCC engine and an RBCC engine can be observed. The performance requirements of an SSTO capable of carrying an acceptable payload mass into orbit typically necessitate the use of fuel that provides high specific impulses, such as hydrogen.

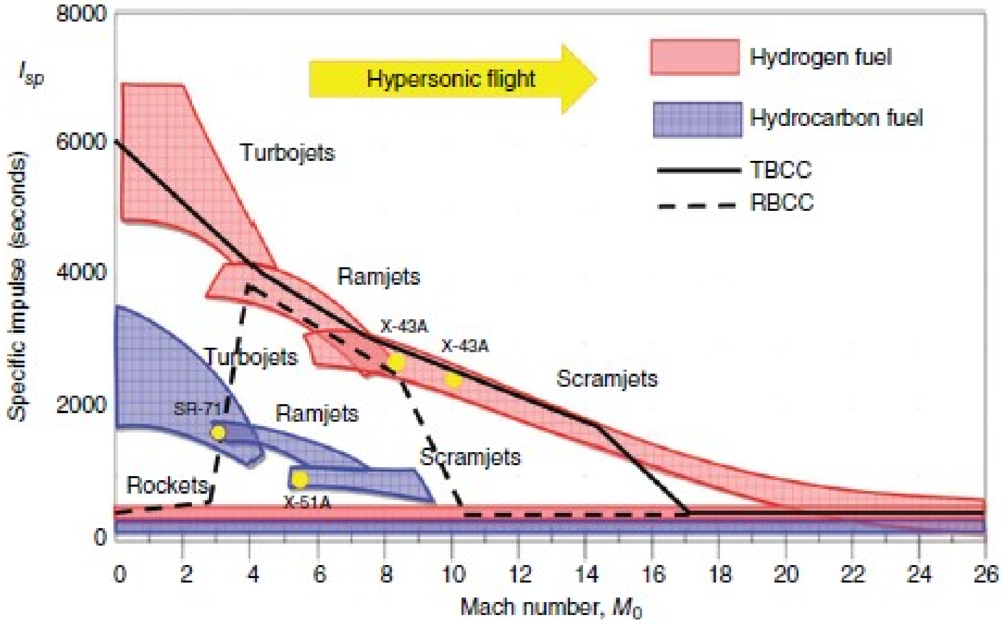

Figure 2.22: Performance comparison between different propulsion engines

2.4.1 A Comparison of Different Architectures

Termochemical Rockets

This architecture offers several advantages, such as a high thrust-to-weight ratio and the ability to operate in a vacuum environment, along with high reliability due to the experience gained from its use in multiple space missions. Thermochemical rockets can be divided into different classes depending on the type of propellant used. Solid Rocket Motors (SRMs) are extensively employed in various applications such as sounding rockets, military missiles, and boosters due to their relatively simple structure and ability to provide high levels of thrust. However, they cannot be stopped and restarted, their thrust profile is predetermined during the design phase, and the combustion products generated by conventional compositions are pollutants and harmful to the environment. Additionally, the specific impulse levels achieved are low, in the range of 300-350 sec.

Hybrid Rocket Engines (HREs) have the characteristic of storing the fuel and oxidizer in different states. In terms of performance, they fall between SRMs and Liquid Rocket Engines (LREs), offering relatively high specific impulses and significant operational flexibility. Nevertheless, low regression rates limit the levels of thrust that this propulsion system can provide.

Liquid Rocket Engines (LREs) are distinguished by their high specific impulses, which enable thrust control and restart capabilities during missions. Additionally, some propellant mixtures used in LREs are environmentally friendly. They typically use turbopumps to feed propellant into the combustion chamber, thereby increasing structural complexity and weight. In general, the major disadvantage of this propulsion strategy is the necessity to store both fuel and oxidizer required for the mission.

Ramjet/Scramjet

Ramjet engines are a type of airbreathing jet configuration where compression is not achieved mechanically through a dedicated compressor but instead utilizes the flow kinetics and the engine's cross-sectional geometry to spread the flow isentropically and compress it. The supersonic external airflow is thus compressed and decelerated through a series of oblique shockwaves until it reaches a subsonic regime. The airflow is then mixed with fuel, and the mixture is injected into the combustion chamber. Following a combustion at constant pressure in the combustion chamber, high-temperature products flow is expanded through the nozzle. Conventional ramjets fueled by hydrogen can achieve speeds of Mach 5 or 6; however, different propulsion systems are required to reach higher flight Mach numbers. Scramjets allow for acceleration of a vehicle to reach hypersonic flight regimes, ideally providing thrust from Mach 5 upwards to Mach 10. The engine configuration is similar to the ramjet, as no embedded turbomachinery such as compressors or turbines are used in the ducts. Additionally, the airflow is always decelerated and compressed through a series of oblique shockwaves. However, unlike ramjets, scramjets maintain airflow continuously in supersonic conditions.

It is therefore possible to consider a dual-mode ramjet-scramjet engine to cover a wide spectrum of flight Mach numbers, but it would not be able to provide thrust if the vehicle has not already exceeded a certain flight speed, nor could it operate in a vacuum. This type of engine would provide satisfactory performance above flight Mach numbers between 2 and 3. In general, ramjets, scramjets, and dual-mode engines cannot be used to carry out the entire mission of a Single-Stage-To-Orbit (SSTO) vehicle as it is necessary to employ two different engines or subsystems to accelerate the vehicle from static ground conditions and provide thrust during the in-space phase of ascent.

Liquid Air Cycle (LACE)

The underlying concept of this propulsion system is to extract oxidizer from the atmosphere. Liquid fuel, typically hydrogen, is pumped into a precooler and a condenser, where it exchanges heat with the airflow. This process liquefies the air, which is then pumped into the combustion chamber and burned at high pressure with hydrogen, similar to a conventional rocket engine. The hot gaseous products are then expanded through a supersonic nozzle. The propulsion system provides a specific impulse of around 1000 seconds. It works because liquid oxygen (LOX) has higher temperatures than liquid hydrogen (LH2), but the problem lies in the amount of hydrogen needed to liquefy the oxygen from the air. With 1 kg of hydrogen, a maximum of 10 kg of liquid oxygen can be obtained, resulting in an equivalence ratio of 7 to 8.

A more advanced version of the LACE system, called the Air Collection Enrichment (ACE) system, includes a liquid oxygen separator following the liquefier. This arrangement enables not only the supply of the rocket engine but also the simultaneous filling of the oxidizer tanks throughout the air-breathing ascent, which will then be used for the operational phase in the vacuum.

While both conventional LACE and ACE technologies are of interest in research and development, they are not ideal for an SSTO launcher due to their high fuel consumption. At sea level conditions, the basic LACE system requires fuel-air ratios up to eight times greater than the stoichiometric ratio to effectively cool down the air. Additionally, the technological complexity of these systems does not justify the modest increase in specific impulse compared to conventional thermochemical rockets.

Turbine Based combined cycle (TBCC)

These devices are designed to utilize a turbojet engine in the early stages of flight, which then gradually transitions into ramjet mode or into a dual-mode ramjet-scramjet system. The integration of these systems allows for achieving high flight speeds starting from a static condition at takeoff.

During subsonic flight phases, the incoming airflow is mechanically compressed by a turbo compressor, bringing it to high pressures towards the entrance of the combustion chamber. At higher flight speeds, the turbo compressor is bypassed, and the engine operates similarly to a conventional ramjet system.

The simplest architecture proposed for TBCC engines involves two separate flow paths for the different operating modes, significantly contributing to the overall weight of the engine. Other configurations propose integrating the turbojet and the dual-mode ramjet-scramjet subsystem into the same airflow path. In this case, it is necessary to implement specific devices capable of deviating the flow toward the correct subsystem based on flight conditions or the possibility of feathering the turbo compressor blades.

The Air Turbo Ramjet (ATR) is an example of this concept propulsion The main components of the turbo ramjet, moving in the streamwise direction from left to right, are: a low pressure ratio, high throughflow axial flow compressor, a turbine that is driven by high pressure, high temperature gases generated in a separate combustion chamber, a mixer, that blends the airflow with the turbine 'primary' flow, fuel injectors, a burner and a nozzle. The presence of the fan and turbine require that at least the forward portion of this engine be axisymmetric, rather than two-dimensional, which can complicate integration with the vehicle. A possible variation is the turbo ramjet rocket [34]. The primary reason for adding the internal rocket engine is to increase the thrust available at any speed, particularly at the lower and higher Mach numbers for which the ramjet and scramjet may not be adequate.

Rocket Based combined cycle (RBCC)

This type of combined-cycle engine features several propulsion subsystems that operate adapting to changing flight conditions. An RBCC engine typically includes an inlet, an isolator, an ejector primary rocket, a combustion chamber, and a nozzle. They do not require the installation of turbomachinery. During the initial phase of the mission, the rocket is ignited in ejector mode, accelerating the vehicle from zero velocity to supersonic speeds. This phase prepares the vehicle for activating the ramjet mode, typically occurring at a flight Mach number between 2 and 3. Once activated, the ramjet engine efficiently accelerates the vehicle up to Mach 5 or 6, at which point the transition to scramjet mode can occur if the engine configuration allows it. The ramjet/scramjet mode operates up to a certain Mach, then the rocket is used again, increasing fuel consumption but already being close to space.

In ejector mode, these engines increase the mass flow of rocket exhaust gases by pulling in additional mass from the surrounding atmosphere. Energy transfer occurs through viscous shear forces rather than turbomachinery, resulting in lower energy transfer efficiency compared to turbojets. However, it is still considered good candidates for low-speed propulsion primarily due to its mechanical simplicity and the ability to easily integrate it into the baseline engine flow path. It has

also been demonstrated that the thrust of the baseline engine can be significantly increased.
The configuration of RBCC engines can be axisymmetric or integrated with the vehicle body, resulting in performance benefits due to forebody pre-compression and afterbody expansion. Both configurations are suitable for both horizontal and vertical takeoff due to the high thrust provided by the rocket during initial acceleration.

Synergetic Air-Breathing Rocket Engine (SABRE)

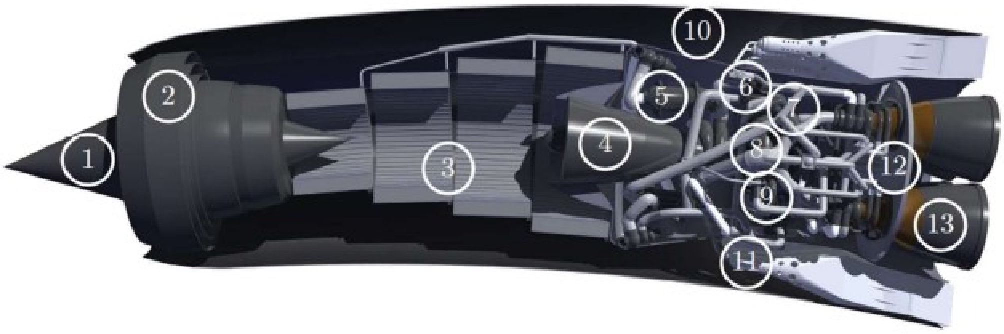

Figure 2.23: 1) movable spike 2) intake 3) precooler 4) air compressor 5) pre-burner and reheater (HX3) 6) helium circulator 7) H2 pump 8) He turbine and regenerator (HX4) 9) LOx pump 10) spill duct 11) ramjet burners 12) heat shield 13) thrust chamber [35]

The Synergistic Air-Breathing Rocket Engine (SABRE) is the key component of the Skylon, enabling the single-stage-to-orbit vehicle to operate in both air-breathing and rocket modes. This unique engine concept operates like a turbojet, utilizing hydrogen as fuel in combination with air from take-off until the transition point, set at an altitude of 25 km, enabling the engine to reach a Mach number of 5. Once this speed regime is reached, the engine transitions to rocket mode, during which air is replaced by liquid oxygen (LOx), ensuring a specific energy release during combustion compatible with the levels required for ascent to low Earth orbit. The transition of the SABRE to rocket mode occurs at an altitude where it is no longer feasible to sustain LH2-air external combustion due to the rarefied conditions of the atmosphere at that altitude. However, the advantages of this innovative engine design are significant, as the air-breathing operating mode allows for a reduction in the amount of propellant needed to be stored inside the Skylon to ensure access to the target orbit, consequently increasing the payload mass that can be transported to its destination. The architecture of the SABRE is well summarized by the following figure 2.24 [22]

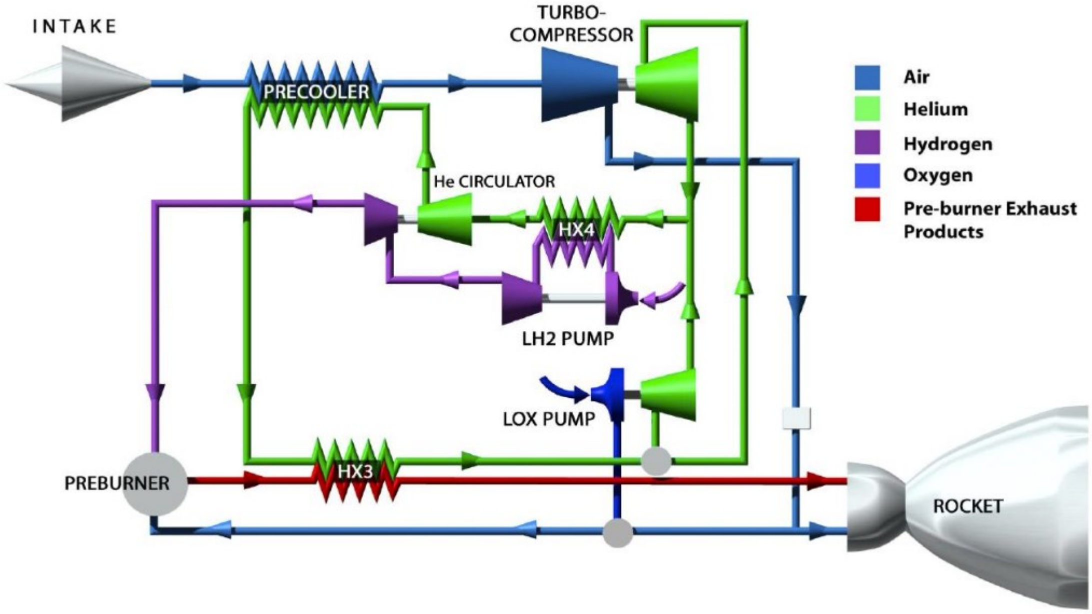

Figure 2.24: Simplified SABRE cycle

Regarding its air-breathing operating mode, the SABRE falls into the category of deeply precooled combined cycle engines, where the primary air cycle is coupled with a secondary regenerative cycle using helium for thermal management of the engine. This solution allows for the regeneration of a portion of the heat extracted from the hot incoming airflow into the engine, extending its operation in air-breathing mode up to a Mach regime exceeding 5 without performance degradation, particularly in specific impulse. Additionally, the SABRE involves a two-stage combustion process occurring in two different combustion chambers: the PreBurner (PB) and the main combustion chamber (CC), enabling the regeneration of a portion of the heat produced during the initial combustion segment, again utilizing the helium cycle. The regenerated heat through the helium cycle is utilized to heat the cold flow of hydrogen stored at a temperature close to 0K to maintain its liquid state during storage, as well as to power the compressor involved in the primary air cycle. As reported in V. F. Villàcé, the incoming air captured by the intake is deeply cooled by a flow of cold helium inside the precooler (PC), then passes through the high-pressure ratio air compressor (AC), downstream of which the flow is split with a variable splitting ratio depending on the flight Mach number and redirected to the two combustion chambers. The two-stage combustion takes place first in the PB, where a portion of the air is burned under fuel-rich conditions.

The exhaust gases from the PB, after exchanging some of their heat in a heat exchanger with helium, rejoin with the second air flow from the splitting at the main CC, where combustion is completed again under fuel-rich conditions. Finally, the combustion products from the main CC then expand in the nozzle, generating thrust. Additionally, bypass burners are provided for a portion of the incoming air flow at the intake, optimizing engine performance and efficiency. Regarding the engine's operation in rocket mode, the engine cycles are shorter as the air intake is closed, and the two-stage hydrogen-air combustion is replaced by a single stage of hydrogen-oxygen combustion. Oxygen in this configuration contributes to heat regeneration by cooling the nozzle walls, thereby recovering some of the heat produced during the hydrogen combustion. As reported in the Skylon User Manual, this engine can provide a gross thrust of approximately 2 MN per nacelle in both of its operating modes. In the air-breathing phase, it offers a specific impulse ranging from 40,000 to 90,000 Ns/kg. However, in the rocket phase, the specific impulse value is around 4500 Ns/kg. The architecture of the SABRE engine is indeed custom-designed for space access, offering significant advantages. It provides a high thrust-to-weight ratio during air-breathing operation, coupled with moderate specific fuel consumption, which enables efficient propulsion during the initial phase of flight. Furthermore, as it transitions to rocket mode, it maintains a high specific impulse, ensuring optimal performance during the phase of reaching the target orbit.

2.5 Thermal Protection System (TPS)

When flying at high-speed regimes, it is crucial to consider the use of a Thermal Protection System (TPS) for protection against aerodynamic heating, while paying attention during the design phase to the impact on the vehicle's performance due to operational capability and system weight. These aspects are particularly relevant in the case of Single-Stage-To-Orbit (SSTO) vehicles due to the large surfaces that require thermal protection and the various operational phases they undergo during flight missions. The configuration of future commercial vehicles, which allows for high flight frequency, requires a reusable lightweight and robust thermal protection system that requires minimal maintenance. In this case, ceramic tile and blanket TPS, such as those used on the Space Shuttle orbiter, are not suitable because they require more than 40,000 work hours to refurbish the thermal protection system between flights. Furthermore, despite effectively protecting the vehicle from aerodynamic heating, the materials they are composed of are very fragile and do not allow the orbiter to fly through rain.

The TPS for future reusable vehicles must be able to withstand various operational environments, not only rain but also aerothermal, acoustic, and thermal-mechanical loads, as well as potential low- and high-velocity impacts caused respectively by dropped tools during maintenance procedures and orbital debris. To reduce maintenance hours and avoid the use of fragile materials that are easily damaged, thus increasing damage tolerance, the TPS must be easy to inspect and should not require waterproofing between flights.

Active systems will not be considered. While an active TPS could potentially be functional and make the vehicle lighter, it has been decided in this thesis work to focus only on passive TPS due to their widespread use in real space missions. Additionally, an active TPS is more complex and therefore less reliable.

2.5.1 TPS Concepts

A brief description of each TPS concept considered in this thesis are given in this section. Three categories of Thermal Protection Systems (TPS) are examined, based on "Parametric Weight Comparison of Advanced Metallic, Ceramic Tile, and Ceramic Blanket Thermal Protection Systems" by David E. Myers, Carl J. Martin, and Max L. Blosser [36]. These are: metallic panels, rigid ceramic tiles, and flexible ceramic blankets. The TPS of the Shuttle, as well as advanced and proposed TPS concepts, are included in the examination.

Flexible Ceramic Blankets

Flexible ceramic blankets used in Thermal Protection Systems (TPS) are constructed with fibrous insulation between outer layers of woven ceramic fabric. These blankets are reinforced with a coating on the outer fabric layer to increase their stiffness, and they are attached to the structure using room temperature vulcanizing (RTV) adhesive. Blankets offer cost-effective installation due to their initial flexibility.

An example of this is the Advanced Flexible Reusable Surface Insulation (AFRSI) blankets employed on the Space Shuttle orbiter. This type of TPS requires waterproofing after each flight, resulting in significant maintenance efforts and expenses. Additionally, although initially flexible, the addition of the C-9 coating and exposure to high temperatures make the outer fabric brittle and susceptible to damage. Another significant issue is the surface roughness due to the manufacturing process, which leads to an increase in both drag and aerodynamic heat fluxes. This latter issue is less pronounced in the Thermal Protection for Ablators and Bond Insulation (TABI) TPS, as it has a smoother surface in comparison. TABI TPS allows for greater tolerance to higher temperatures but also shares waterproofing and surface brittleness issues similar to AFRSI. The relatively low emissivities of blanket fabrics coated with C-9 limit their usage in high-temperature environments.

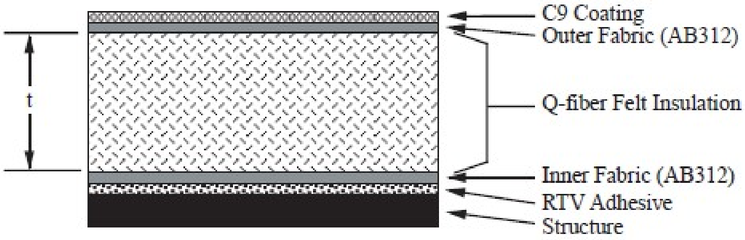

(a) AFRSI thermal protection system

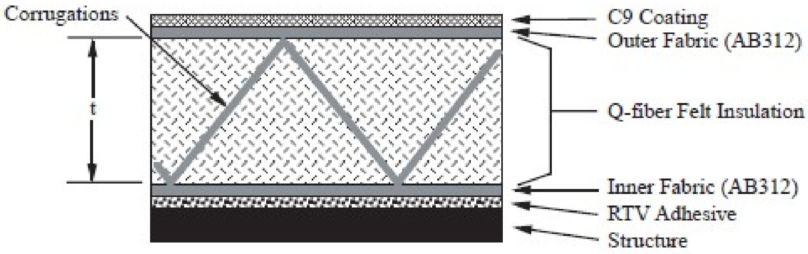

(b) TABI thermal protection system

Figure 2.25: Flexible Ceramic Blankets examples

Rigid Ceramic Tiles

Rigidized ceramic insulation tiles have the ability to withstand high temperatures, which is why they were used on the Space Shuttle orbiter in surface areas where temperatures ranged between 950 and 1800 K. The basic structure of the thermal protection system consists of a ceramic tile, a Nomex (nylon) felt strain isolation mounting pad, and RTV adhesive. If the tiles are coated, the surface emissivity and toughness improve, and catalycity is reduced. Examples include the LI-900 (144.2 kg/m3) and LI-2200 (302.4 kg/m3) tiles, which are coated on five sides. The nature of ceramic tiles is fragile and low in strength, so they must not be affected by the thermal and mechanical strains of the underlying structure, and therefore need to be isolated using a felt strain isolation pad (SIP). The size of the orbiter tiles is limited to approximately 15cmx15cm square footprints due to strain isolation and thermal shock requirements. The tiles have low tolerance to impact damage, and after each flight, waterproofing is required, which, combined with inspections and repairs, leads to high costs and extended maintenance times. To reduce maintenance times and costs, and improve performance, such as strength and durability as well as increased temperature capabilities, advanced tile systems have been developed, of which the AETB tile with TUFI coating is an example.

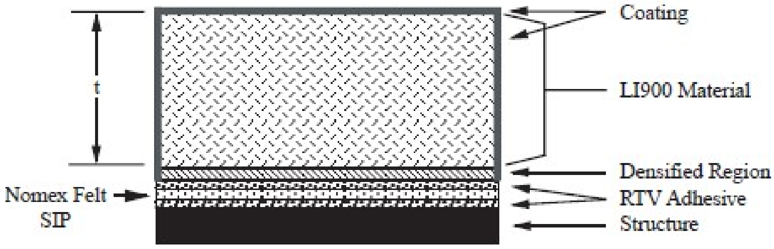

(a) LI-900 thermal protection system

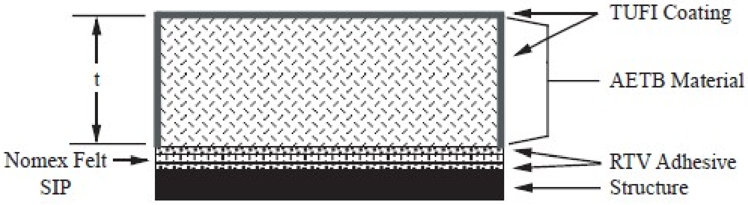

(b) AETB thermal protection system

Figure 2.26: Rigid Ceramic Tiles examples

Metallic Panels

The Metallic Thermal Protection System (TPS) concept is under development at NASA Langley Research Center as an alternative to ceramic TPS. The concepts have progressed during the development phase from early metallic heat shields to titanium multiwall concepts to superalloy honeycomb sandwich panels. In this study, the design of the metallic TPS concept features a thin metallic box enclosing lightweight fibrous ceramic insulation. The use of low-density, efficient fibrous insulation helps reduce the weight of the metallic box. This box is supported by an edge support system made of RTV and Nomex felt to prevent any flow from beneath the panels and is secured to the structure using mechanical fasteners. The outer face of the box, except for the multiwall concept, is crafted from a honeycomb sandwich structure to enhance load-bearing capacity and durability.
Considering an application on a spacecraft, appropriate superalloys are used in surface areas where high temperatures are reached, while titanium alloys are utilized in areas where temperatures are lower to minimize weight. The substantial difference from ceramic tiles is that metallic materials have a ductile nature, potentially allowing for a more robust TPS and easy design modification, such as making the facesheets thicker to improve durability. Additionally, maintenance times are greatly reduced, as waterproofing is not required since the encapsulated designs are inherently waterproof, and the use of mechanical fasteners allows for easy removal and reattachment.

Metallic TPS panels offer many benefits but have not yet been sufficiently flight-proven, unlike tiles and blankets that have been widely used. This leads to high expected initial costs due to the required tooling. Moreover, special design features may be necessary to allow the spacecraft structure to accommodate the mechanical fasteners.
One example of metallic TPS is as follows:

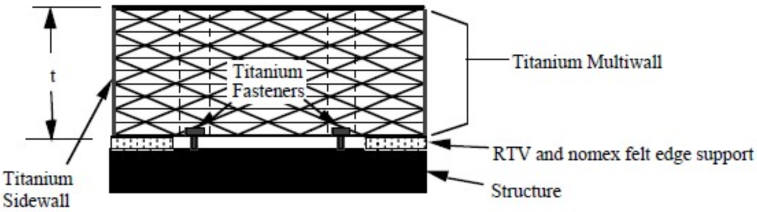

Figure 2.27: TIMW thermal protection system

Other concepts are presented below. The SA/HC metallic TPS integrates lightweight insulation materials such as Q-fiber and Cerrachrome between dual metallic honeycomb sandwich panels. An enhanced version, known as SA/HC2, has been created to improve the performance of the superalloy honeycomb system. The titanium honeycomb (TI/HC) metallic TPS concept offers a lighter alternative for lower temperature applications. the Advanced Metallic Honeycomb thermal protection system (AMHC) is presented by NASA LaRC as an upgrade to the current superalloy honeycomb metallic system.

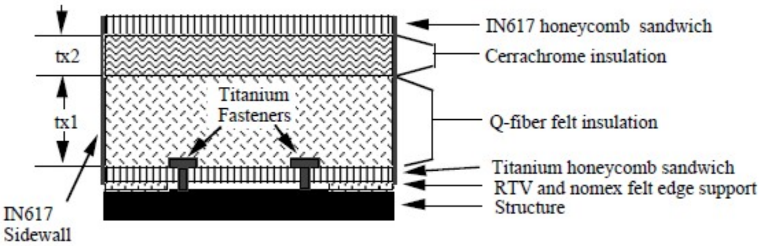

Figure 2.28: SA/HC thermal protection system

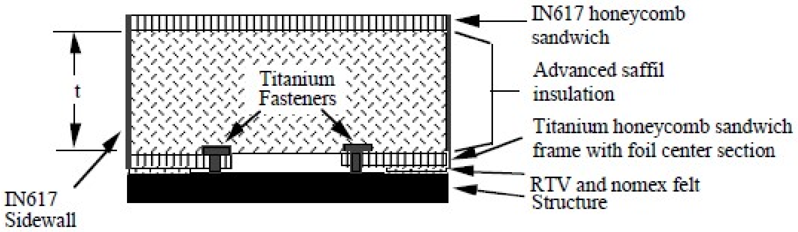

Figure 2.29: SA/HC2 thermal protection system

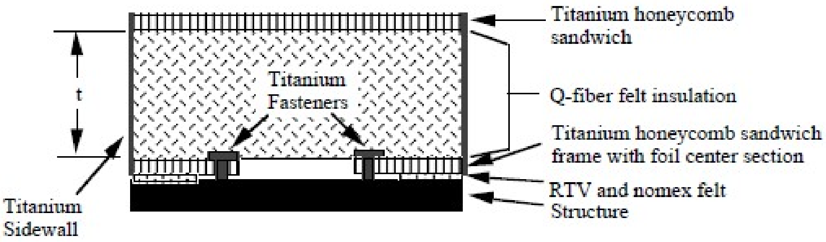

Figure 2.30: TI/HC thermal protection system

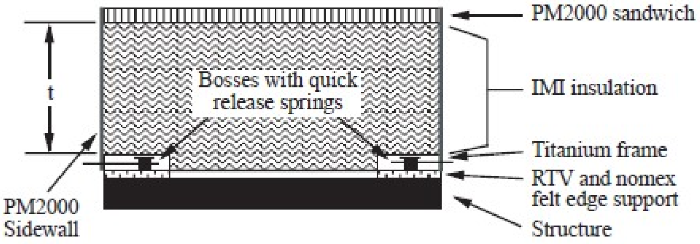

Figure 2.31: AMHC thermal protection system

Chapter 3

Methodology Development

3.1 Approach

The development of the conceptual design is based on an iterative process that aims to bring the hypothetical variables into convergence with the calculated ones. The methodology starts with the definition of requirements, constraints and assumptions regarding mission performance, the chosen vehicle configuration, propulsion strategy and technological availability. Dimensioning must take into account that a launch vehicle differs significantly from a conventional aircraft, not only because of the need to get into space and the more extreme external conditions to which it is exposed, but also because it requires a volume of propellant that can account for up to 80 percent of the total volume of the vehicle, unlike the conventional aircraft, whose essential volume is that of the passengers. The mass ratio is determined for the selected mission trajectory according to the performance analysis of the vehicle, which is considered as a single system due to the interdependence of aerodynamics, propulsion and structure. From the choice of propellant, the required percentage of vehicle volume occupied by the propellant can be determined. The individual propellant densities can vary from 70 kg/m3 to 1300 kg/m3 (normal boiling point hydrogen to triple point LOX). So volume becomes the dominant factor for the hypersonic sizing program. With the convergence criterion, the available volume is iterated until it corresponds to the required volume. The design procedure therefore converges to the volume and mass of the system but does not allow a comparison of the available thrust with that required in the various mission phases, nor a check of the planform load limit on landing. In parallel, a multiple-matching chart is developed to obtain the design space available for the selected mission.

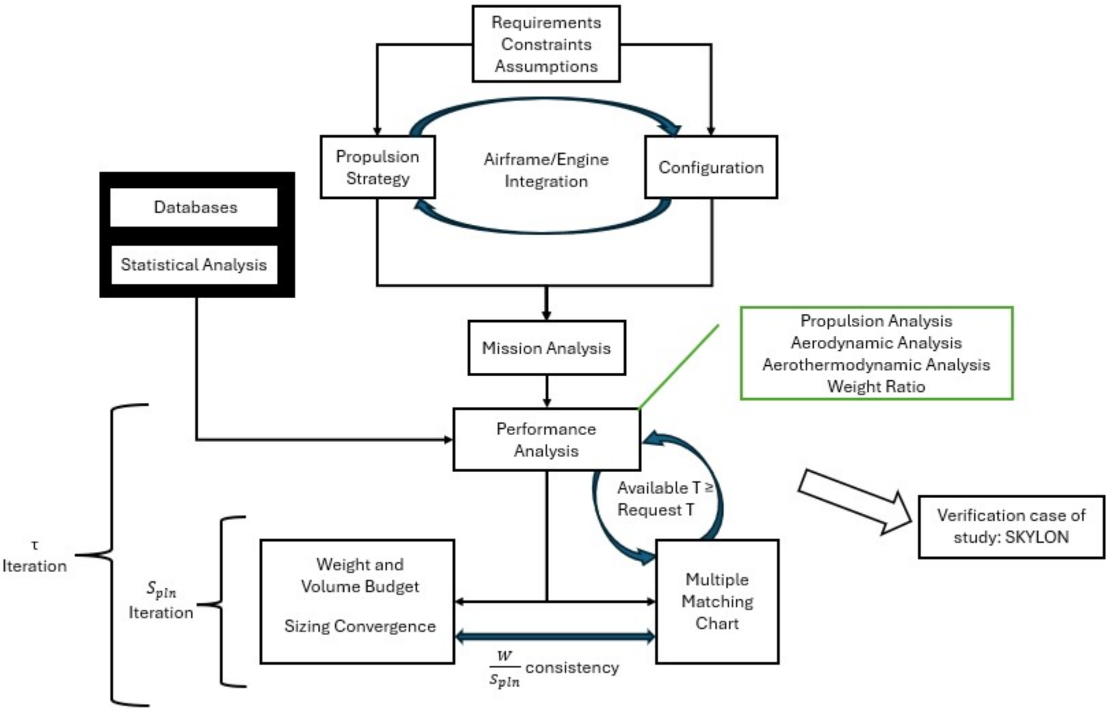

Figure 3.1: conceptual scheme of the methodology

Requirements, Constraints, Assumptions

The first phase of the methodology consists of considering input values provided by stakeholders, mission constraints, and various assumptions necessary for the development of the conceptual design. The primary requirement is the mission objective, which is to deliver a certain payload quantity to a desired target orbit. Additionally, it is necessary to specify whether the vehicle should also be configured for transporting personnel into orbit. Since the tool is designed for a vehicle with horizontal takeoff and landing, runway length requirements are also included as criteria. It may be required for the vehicle to take off and land at conventional airports. Therefore, the propulsion strategy to be applied and the configuration concept of the vehicle are chosen. Design values such as the Mach number transition between airbreathing and rocket propulsion modes, the dynamic costant pressure, and the Industrial Capacity Index (see section 3.2) can be selected. As for the assumptions to be applied, these will be introduced step by step into the tool since they are not directly chosen by the user.

3.2 Sizing Methodology

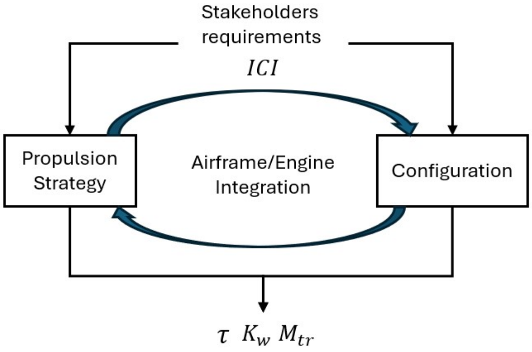

Figure 3.2: sizing methodology input/output variables

The sizing of the SSTO horizontal take-off and landing begins with the choice of vehicle configuration, which is closely linked to the choice of the propulsion system and structural material according to the equation:

$$\text{ICI} \;= 10 \cdot \frac{\left(\frac{\rho_{\text{ppl}}}{WR-1}\right)}{\left(\frac{W_{\text{str}}}{S_{\text{wet}}}\right)} \tag{3.1}$$

The ratio between the propulsion index and the structural index, which are independent of each other, is defined as an index of industrial capacity and determines the technical maturity of the conceptual design, that is the technical ability to achieve a given objective. The variation of this ratio leads to a variation of the vehicle size and geometry. High values of ICI require a high level of technology. As reported in Curran's chapter [33], the maximum achievable value is approximately 37.7 m^{-1}, using the values from Tjonneland. Industrial capacity index values around 32 m^{-1} were deemed available by Czysz in the 1994 time frame.

In this initial phase of the methodology development, it is important to evaluate first the dimensionless volume index tau, introduced by Kuchemann. From the book chapter 'Scramjet propulsion - transatmospheric launcher sizing' by Czysz and VDK [33], the value range of tau can be extrapolated based on the selected configuration and propulsion strategy.

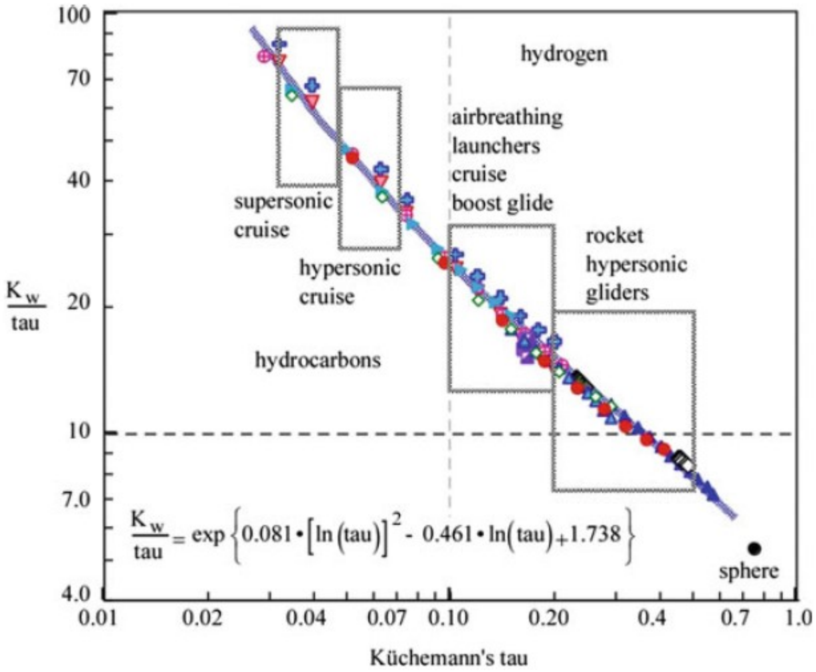

Figure 3.3: Reference geometric parameters of hypersonic aircraft configurations

This parameter defines the 'slenderness' of the vehicle and sets the total volume in relation to the planform surface as follows:

$$\tau = \frac{V_{tot}}{S_{pln}^{1.5}} \tag{3.2}$$

From the graph in Figure 3.4, the information regarding the typical range of this sizing parameter for our case study is extracted, which turns out to be $0.1 < \tau < 0.25$. Assuming a value of tau, the ratio between wetted surface and planform surface Kw can be determined by the fundamental sizing relations taken from 'Hypersonic Convergence', an approach that allows the geometry of a hypersonic vehicle to be related to the volume and surface area through a parametric study. For each chosen geometric profile or configuration, the tau index allows a scaling of the surface and volume sizes of the vehicle.

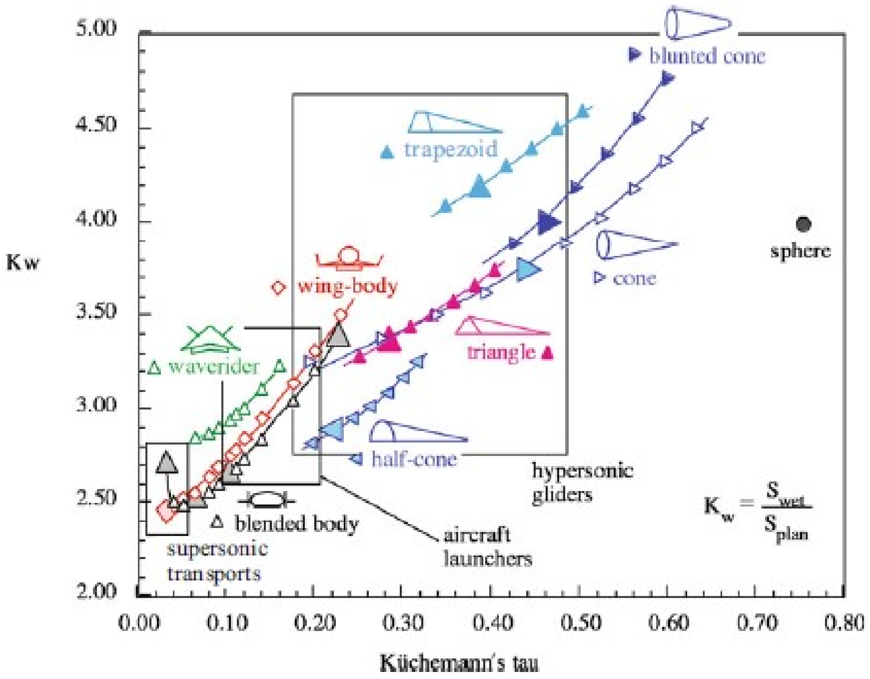

Figure 3.4: The surface and volume continuum of hypersonic configuration concepts

The configurations applicable to the case of single stage to orbit HTOL fall into the 'airbreathing' range, and are therefore the following:

1. Wing Body

$$K_w = -93.831 \cdot \tau^3 + 58.920 \cdot \tau^2 - 5.648 \cdot \tau + 2.821 \tag{3.3}$$

2. Blended Body

$$K_w = -62.217 \cdot \tau^3 + 29.904 \cdot \tau^2 - 1.581 \cdot \tau + 2.469 \tag{3.4}$$

3. Waverider

$$K_w = -533.451 \cdot \tau^3 + 220.302 \cdot \tau^2 - 22.167 \cdot \tau + 3.425 \tag{3.5}$$

3.3 Mission Analysis

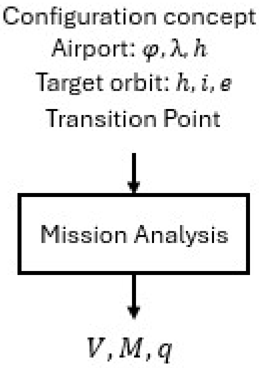

Figure 3.5: mission analysis input/output variables

The mission profile for the SSTO HTOL may vary depending on the propulsion strategy, selected configuration and mission requirements and constraints, such as the coordinates of the launch base and the choice of target orbit. It consists of a take-off phase with a similar procedure as for subsonic and supersonic aircraft, and a second climb phase in which the space launcher withstands a dynamic pressure of approximately 25-95kPa, which remains constant for the remaining transatmospheric climb until reaching the rocket transition Mach, entering in the third and last ascent phase in rocket mode. It is worth noting that the dynamic pressure in this phase should not exceed 100 kPa due to structural constraints, nor should it be below 24 kPa to achieve the required airflow and therefore thrust values for the vehicle, and maintain the required lift. This phase is followed by a climbing phase until it enters an elliptical transfer orbit (coast phase) and then circularizes at apogee at an altitude of about 100-150 km. An example of the typical SSTO ascent corridor is reported in Figure 3.6 below. If requested, a transfer to Hohmann can be carried out, with possible changes of plan, to reach the target orbit at a higher altitude. Once in orbit, the vehicle can deploy its payload to either orbit the Earth or loiter until the proper entry interface is required to reach a specific target. Once the payload is released, it can de-orbit and perform an autonomous unpowered landing at the launch site. It is necessary to first define the model of the environment in which the flight path is to be analysed. In this case, it was decided to proceed with the implementation of the mathematical ISA model, extended up to an altitude of 80 km. In this model, the atmosphere is divided into layers in which the absolute temperature varies linearly with the geopotential height. The values for pressure and density are determined by applying hydrostatic balance, which relates the rate of change of pressure with geopotential altitude, and the

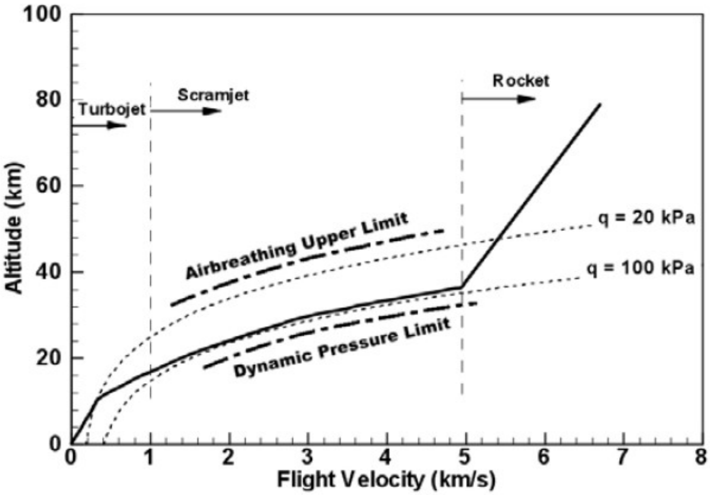

Figure 3.6: Hypersonic airbreathing flight corridor [37]

ideal gas law. After that we can determine the trajectory of the mission. The general equation of the motion of the space launcher along the trajectory is:

$$m\frac{dV}{dt} = T\cos(\alpha+\delta) - D - mg\sin\theta \tag{3.6}$$

There is no general solution to the equation because the quantities involved may be functions of velocity and/or time, which depend on the design of the vehicle and the flight path. To obtain explicit solutions, the terms can be considered independent in order to integrate the equation

$$\int_0^2 dV = V_2 - V_0 = \int_0^2 g\left[\frac{T\cos(\alpha+\delta) - D}{\dot{m}_\mathrm{P}}\right]\frac{dm}{m} - \int_0^2 g\sin\theta dt \tag{3.7}$$

Where $m = m_0 - \int_0^2 \dot{m}_\mathrm{P} dt$ and $\dot{m}_\mathrm{P}$ is the total propellant flow rate. We initialize the integration at time $t_0 = 0$, so that $V_0 = 0$, while the final condition is regarded as the end of the powered phase. The value of the velocity V_2 can be derived approximately with Kepler's law as follows if the perigee of the drag-free transfer orbit coinciding with point 2 (Hohmann transfer). Considering that the drag in the unpowered phase, i.e. during the transfer orbit, causes a reduction in velocity, the velocity at point 2 must be higher in order to reach the circular target orbit. The solution of the integral requires detailed knowledge of the engine characteristics and the aerodynamics of the vehicle as well as the ascent trajectory. However, it is possible to obtain approximate closed-form solutions by dividing the trajectory into segments modeled so that altitude and speed are directly dependent on each other. This is done by defining coefficients that can be chosen to match the thrust weight and aerodynamics of the vehicle to maintain a reasonable flight path angle. The trajectory modeling described by Billing in 'Design and development of Single-Stage-To-Orbit Vehicles' is used [38]. From the take-off, the first ascent phase segment is modeled as

$$Z = C_5 + C_6 V^2 \tag{3.8}$$

The subsequent ascent segment leads to reaching the selected dynamic pressure.

$$V = C_2 + C_3 Z + C_4 Z^2 \tag{3.9}$$

Next comes the climb phase at constant dynamic pressure.

$$V = \sqrt{\frac{2q}{\rho}} \tag{3.10}$$

The rocket flight phase is instead modeled for simplicity as a Hohmann transfer that begins from the switch point. A specific ΔV is then calculated to be provided at the start of the Hohmann transfer.

$$\Delta V = \sqrt{2\left(E_h + \frac{\mu}{r_{max_{airbreathing}}}\right)} \tag{3.11}$$

Regarding the re-entry phase, a Lifting Entry is considered. To date, a re-entry corridor has neither been defined nor validated for the case study; the re-entry path is determined by the Equilibrium Glide Equations. Thus, the velocity during Entry has been derived as a function of altitude and the ratio $\frac{L/D}{\beta}$.

$$v = \sqrt{\frac{g_0\left(r_0 + h\right)}{1 + \frac{\rho(r_0+h)L/D}{2\beta}}} \tag{3.12}$$

where $\beta = \frac{m}{C_\mathrm{D} S_\mathrm{pln}}$ is the ballistic coefficient. The time for entry can be extrapolated from the derivative of velocity with respect to time through algebraic steps. This is done as a function of the ratio between entry velocity and flight velocity, and the aerodynamic efficiency.

$$\Delta t = \frac{1}{2}\sqrt{\frac{r_0}{g_0}}\frac{L}{D}\ln\frac{1 + \left(\frac{v}{v_{c0}}\right)^2}{1 - \left(\frac{v}{v_{c0}}\right)^2} \tag{3.13}$$

with

$$\frac{v}{v_{c0}} = \left[1 + \frac{\rho r}{2\beta}\right]^{-\frac{1}{2}} \tag{3.14}$$

This data is of particular importance for calculating the heat load required for sizing the Thermal Protection System.

3.4 Performance Analysis

The determined velocities and Mach numbers along the trajectory, and therefore the dynamic pressure experienced by the vehicle throughout the flight path, can be fed into propulsion, aerodynamics, and aerothermodynamics analysis to evaluate vehicle performance.

If the user has selected engines listed in the propulsion database and a specific vehicle configuration in the aerodynamic database, the performance data can be directly incorporated into the methodology algorithm. The user could expand the databases by including performance data obtained from his own analysis (ex. CFD analysis). Instead, if the user has chosen not to use any database, analytical methods are implemented to develop the performance analysis. This approach is called 'multifidelity approach'.

3.4.1 Engines performance

For the assessment of propulsion performance, operational modes are considered as individual engines for ease of analysis. The thrust levels in each operational mode are initially estimated statistically (see section 2.3), with high-speed thrusts derived from the statistical analysis in Roberto Cau's thesis work [39].

Additionally, to evaluate the switch between one airbreathing mode and the other, the trends of specific impulses are observed, and maximum values are sought. Subsequently, it is verified that the transition Mach numbers are compatible with the ranges identified in Roberto Cau's thesis. The control parameter for the switch between airbreathing mode and rocket mode is instead the product of specific impulse and thrust-to-weight ratio. This leads to defining consistent input values between airbreathing and rocket modes. The switch between airbreathing mode and rocket mode occurs around Mach 5, unless scramjet technology is present, that can increase this value up to Mach 12.

In this section are reported the final equations of ideal cycle analysis performed to estimate the thrust and fuel efficiency of engines. The ideal cycle analysis does not describe the components of the engine but only reports the variations in airflow conditions within the engine. The analytical methods are consistent with the formulations provided by Roberto Cau [39], and reported in Appendix B. Ideally, only the total pressure ratio and total temperature ratio across the compressor and the turbine, if present, are assumed to differ from unity.

Please note that the subscript '0' indicates values referring to ambient conditions.

Engine mode	**Engine performance**
Turbojet	$\frac{F}{\dot{m}a_0} = M_0 \left[\left\{\left(\frac{\theta_0}{\theta_0 - 1}\right)\left(\frac{\theta_T}{\theta_0\tau_c} - 1\right)(\tau_c - 1) + \frac{\theta_T}{\theta_0\tau_c}\right\}^{\frac{1}{2}} - 1\right]$
Ramjet	$\frac{F}{\dot{m}a_0} = M_0\left(\sqrt{\tau_b} - 1\right)$
Scramjet	$\frac{F}{\dot{m}} = M_0\sqrt{\gamma R T_0}\left\{\sqrt{\eta_{\text{KEO}}\ (1+f)\left[1 + \frac{\eta_b\ f\ h_{pr}}{c_p T_0\left(1+((\gamma-1)/2)M_0^2\right)}\right]} - 1\right\}$
Ejector	$I_{sp_p} = \frac{a_0 M_0}{g_0}\phi_p\frac{V_{p0}}{V_0}$
Rocket	$I_{sp} = \frac{c^* c_F}{g_0}$

Table 3.1: Operational engine modes performance

3.4.2 Aerodynamics performance

Curran Model

The Curran aerodynamic model is presented in Ref. [33] In this simplified model, the analysis of aerodynamic coefficients is correlated to a parameter F, which is dependent on the geometry of the aircraft and is defined as:

$$F = \sqrt{\left(\frac{V_{\text{tot}}^{0.667}}{S_{\text{pln}}}\right) \cdot \left(\frac{S_{\text{wet}}}{S_{\text{pln}}}\right)^{1.5}} = \tau^{0.333} \cdot K_W^{0.75} \tag{3.15}$$

in which appears the Küchemann parameter τ and the parameter K_w which employ known geometric variables such as the total aircraft volume V_{tot}, the aircraft wetted surface S_{wet} and the aircraft planform area (also known as reference area) S_{pln}. Having the parameter F, it is possible to determine the maximum aerodynamic efficiency $(L/D)_{max}$ through an empirical correlation as a function of Mach number M:

$$\left(\frac{L}{D}\right)_{\text{max}} = \frac{A}{M} \cdot (M + B) \cdot (1.11238 - 0.1866\dot{\theta} \cdot F) \tag{3.16}$$

With A and B empirical coefficients. Also empirically bound to F is the C_{D_0}, which is found with

$$\beta C_{D_0} = 0.05772 \cdot e^{0.4076 \cdot F} \tag{3.17}$$

where $\beta = \sqrt{|M^2 - 1|}$. Hence, the Drag coefficient can be calculated:

$$C_D = C_{D_0} \cdot (1 + B) \tag{3.18}$$

where the term in brackets depends on the flight condition

- Acceleration: (1+B)=1.075
- Minimum fuel flow Cruise: (1+B)=1.75
- Max efficiency Glide: (1+B)=2

Having the Drag Coefficient and the Maximum Efficiency, it is now possible to calculate the Lift Coefficient for the three above-mentioned flight conditions:

- Acceleration: $C_L \sim 0.1 \cdot (C_L)_{L/Dmax}$
- Minimum fuel flow Cruise: $C_L \sim 0.82 \cdot (C_L)_{L/Dmax}$
- Max efficiency Glide: $C_L \sim (C_L)_{L/Dmax}$

The aerodynamic model just described allows for a simplified and rapid determination of aerodynamic coefficients, requiring a minimal set of inputs. This facilitates its application to any selected aircraft configuration, for which knowledge of the two fundamental parameters, τ and K_w, is sufficient.
In this model, for a fixed configuration, the aerodynamic coefficients are solely functions of the flight Mach number, while the dependence on the angle of attack α is not considered. Consequently, the results obtained may be somewhat inaccurate and suitable primarily for an initial design iteration when limited input data are available.

3.4.3 Aerothermodynamics performance

In this section, wall temperatures, thermal fluxes, and thermal loads to which an SSTO vehicle is subjected during the glide re-entry phase are calculated. A low-fidelity 1D analytical model is considered acceptable for the conceptual design phase.
From input values of velocity and kinematic viscosity obtained respectively from the equilibrium glide equations and the assumption of the ISA atmospheric model, the local Reynolds number can be derived, a very important parameter for determining the behavior of viscous airflow.

$$Re_x = \frac{u_e \cdot x}{v_e} \tag{3.19}$$

The nature of airflow within the boundary layer, formed around a body fully immersed in the flow, can transition from a laminar condition, following the profile of the body, to a turbulent condition. The transition phenomenon is gradual and not easily predictable, but it is necessary to have some engineering tool to predict at which Reynolds number this transition occurs, even if it involves high approximations. In this thesis, the application of an empirical formula used by Bowcutt (Eq. 3.20), based on the cone data of Dicristina, V. [40], is considered.

$$Re_T = 10^\wedge \left(6.421 \cdot \exp\left(1.029 \cdot 10^{-4} \cdot \text{ Mach }^{2.641}\right)\right) \tag{3.20}$$

By equating Eq. 3.19 to Eq. 3.20, the transition point along the vehicle's surface can be determined. At this point, thermal fluxes relative to each velocity and flight altitude are calculated. Once again, one of the simplest methods for estimating hypersonic aerodynamic heating is considered, requiring minimal detail. A generalized form of the thermal flux is used as follows:

$$q_w = 10^4 \cdot \rho^N V^M C \left[\frac{W}{m^2}\right] \tag{3.21}$$

During the calculation phase, the following values are considered for N, M, and C in the case studies according to the different nature of the airflow around a flat plate. The units for q_w, V, and ρ were W/m^2, m/s, and kg/m^3, respectively.

Case of study	**N**	**M**	**C**
Stagnation point	0.5	3	$1.83 \cdot 10^{-8} R^{-0.5} \left(1 - \frac{T_w}{T_0}\right)$
Laminar flat plate	0.5	3.2	$2.53 \cdot 10^{-9} \cos(\varphi)^{0.5} \sin(\varphi) x^{-0.5} \left(1 - \frac{T_w}{T_0}\right)$
Turbolent flat plate V <3962 m/s	0.5	3.37	$3.89 \cdot 10^{-8} \cdot \cos(\varphi)^{1.78} \sin(\varphi)^{1.6} (x - x_T)^{-\frac{1}{5}} \left(\frac{T_w}{556}\right)^{-\frac{1}{4}} \left(1 - 1.11 \frac{T_w}{T_0}\right)$
Turbolent flat plate V >3962 m/s	0.5	3.7	$2.2 \cdot 10^{-9} \cdot \cos(\varphi)^{2.08} \sin(\varphi)^{1.6} (x - x_T)^{-\frac{1}{5}} \left(1 - 1.11 \frac{T_w}{T_0}\right)$

Table 3.2: Heat flux coefficients

As can be observed, the heat flux at the stagnation point depends on the inverse of the square root of the radius of the vehicle's nose, similar to the exact equation for a cylindrical shape:

$$q_w = 0.57 \, \mathrm{Pr}^{-0.6} \left(\rho_e \mu_e\right)^{1/2} \sqrt{\frac{\mathrm{d}u_e}{\mathrm{d}x}} \left(h_{\mathrm{aw}} - h_w\right) \tag{3.22}$$

It can be demonstrated that the approximate solution obtained exhibits a direct similarity with the exact result given by Equation 3.22.
In laminar and turbulent flow conditions, the variable phi in the equations represents the local body angle with respect to the freestream, and x is the distance measured

along the body surface in meters. On the other hand, x_T represents the distance measured along the body surface in the turbulent boundary layer.
The validity of this analytical method is considered reasonable as long as boundary-layer theory remains valid under various flight conditions. For more detailed work, it's advisable to resort to more accurate models or CFD analyses.
To calculate the surface temperature T_w, necessary for determining thermal fluxes, a simple energy balance at the surface is considered, assuming the absence of internal cooling systems but only heat radiation outward.

$$q_{\text{convective}} + q_{\text{radiative}} = \varepsilon\sigma {T_w}^4 \tag{3.23}$$

where $q_{\text{convective}}$ is the convective heat transfer to the surface, $q_{\text{radiative}}$ is the radiative heat transfer to the surface arising from thermal radiation caused by the hot gas in the shock layer, and $\varepsilon\sigma {T_w}^4 \left[\frac{W}{m^2}\right]$ is the heat flux radiated away from the hot wall. In this last equation, σ is the Stefan–Boltzmann constant, and ϵ is the emissivity of the surface. For the atmospheric re-entry trajectory of an SSTO with horizontal landing, $q_{\text{radiative}}$ can be considered negligible as it assumes small values.
Finally, a key quantity for the sizing of the Thermal Protection System is the heat load, defined as:

$$Q = \int_{t_0}^{t_f} q_w(t)\, dt \left[\frac{J}{m^2}\right] \tag{3.24}$$

Given the vehicle's re-entry trajectory and thus the calculated heat flux over the descent time, the integral can be solved.

3.4.4 Weight Ratio definition

Once the performance parameters of the engines, the velocities and the aerodynamics performance of the spaceplane along the modeled trajectory have been determined, the weight fraction is calculated, which indicates the amount of propellant consumed during the transatmospheric ascent. The Breguet formula is then applied in discrete positions where the air-breathing mode is on, dividing the trajectory into steps, each characterized by an altitude increase of 100m.

$$\text{Range } = V t_f = V \left(\frac{L}{D}\right) I_{sp} \ln\left(\frac{W_i}{W_f}\right) \tag{3.25}$$

Assuming a reasonable flight path angle for the trajectory segment, the range is determined. To calculate the WR in each step, the average values of the speed and the propulsive and aerodynamic performance between the extremes of the segment under consideration are taken into account.

$$\left(\frac{W_i}{W_f}\right) = exp\left(\frac{\Delta h}{V \sin\theta \left(\frac{L}{D}\right) I_{sp}}\right) \tag{3.26}$$

For the rocket ascent, the Tsiolkovsky equation is applied, taking as ΔV the difference between the ΔV required to reach orbit through an elliptical transfer trajectory and the velocity of the spacecraft at the moment the airbreathing mode is turned off, also taking into account the losses due to drag.

$$\left(\frac{W_i}{W_f}\right) = exp\left(\frac{\Delta V}{gI_{sp}}\right) \tag{3.27}$$

The product of all weight ratios calculated for each step returns the overall WR along the trajectory. In case the Weight Ratio obtained is greater than 5, according to Ref.[33], vertical takeoff should be considered.

$$WR_{tot} = \left(\prod_{i-segment} WR_{airbreathing_i}\right) \cdot WR_{rocket} \tag{3.28}$$

3.5 Volume and Weight Budget

Taking into account a fixed tau value, the results obtained from the geometry, the aerodynamic and propulsion module and performance analysis are used to determine the weight and volume of the vehicle. The sizing procedure ends with the calculation of the total weight and volume of the vehicle based on the results of the previous analyses. The method uses the parametric relations given by VDK and Czysz for an SSTO vehicle [33]. Please note that all weights are measured in kilograms (kg).
The weight budget is developed starting from the dry weight equation

$$W_{\text{dry}} \approx (1+\mu_a) \cdot \left(W_{\text{str}} + W_{\text{eng}} + W_{\text{sys}} + W_{\substack{\text{crew}\\\text{provisions}}}\right) = W_{\text{EO}} \tag{3.29}$$

The weight terms can be expressed as follows:

- Structural Weight: $W_{str} = I_{str} \cdot K_w \cdot S_{pln}$
- Engine Weight: $W_{eng} = \frac{TW_0 \cdot W_R}{E_{TW}} \cdot W_{EO}$
- Subsystems Weight: $W_{sys} = C_{un} + f_{mnd} \cdot N_{crw} + f_{sys} \cdot W_{dry}$
- Crew Provision Weight: $W_{\substack{\text{crew}\\\text{provisions}}} = f_{cprv} \cdot N_{crw}$

If $N_{crew} = 0$, the vehicle is driven by an automatic control system.
Knowing the Weight Ratio (WR) and providing a required Industrial Capacity Index (ICI) value, the structural index I_{str} can be calculated from Equation 3.1.
The typical ranges of the sizing parameters in the above equations were given by Czysz and VDK after personal discussions with European Aerospace engineers.

$0.16 < f_{sys} < 0.24$
$1.9 < C_{un} < 2.1\ ton$
$1.05 < f_{mnd} < 1.45\ ton/person$
$0.45 < f_{cprv} < 0.50\ ton/person$
$0.14 < f_{crw} < 0.15\ ton/person$

Table 3.3: Typical ranges of the sizing parameters

Lower values can be considered for future applications requiring a high level of industrial technology, while higher values can be used for a more conservative approach.
The dry weight can be rewritten as follows:

$$W_{dry_W} = \frac{I_{str} K_W S_{pln} + C_{sys} + W_{cprv} + \frac{TW_0 W_R}{E_{TW}} \left(W_{\text{pay}} + W_{crw}\right)}{\left[\left(\frac{1}{1+\mu_a}\right) - f_{sys} - \frac{TW_0 W_R}{E_{TW}}\right]} \tag{3.30}$$

It can be noted that the propulsion parameter is highly influential for the Wdry, as it appears both in the numerator and denominator. We can proceed to estimate the value of the Effective Takeoff Weight (ETW) for the chosen propulsion strategy by considering the recommended range by Czysz for the following ratio:

$$4.8 < \frac{ETW}{TW_0 \cdot WR} < 7.7 \tag{3.31}$$

Based on the choice of the f_{sys} value within the range considered in Table 3.3, it can be observed that for weight ratios around 3, the values of ETW are concentrated in a narrow range. However, as the weight ratio increases, the thrust-to-engine weight ratio can vary significantly.
We now proceed with the mathematical method for calculating budget volume. The volume, as already mentioned, is a fundamental parameter for the sizing of the vehicle, as it not only represents an additional feasibility routine, but also the ratio of volume to surface area determines the configuration concept for the system.
The total volume can be expressed as follows:

$$V_{\text{tot}} = V_{\text{ppl}} + V_{\text{sys}} + V_{\text{eng}} + V_{\text{void}} + V_{\text{pay}} + V_{\text{crew}} \tag{3.32}$$

Where the volume terms can be explained as follows:

- Total Volume: $V_{\text{tot}} = \tau \cdot S_{\text{pln}}^{1.5}$
- Propellant Volume: $V_{\text{ppl}} = W_{\text{OE}} \cdot \frac{(WR-1)}{\rho_{\text{ppl}}}$

- Subsystems Volume: $V_{\text{sys}} = V_{\text{un}} + f_{\text{crw}} \cdot N_{\text{crw}} + K_{\text{vs}} \cdot V_{\text{tot}}$
- Engine Volume: $V_{\text{eng}} = k_{\text{ve}} \cdot TW_0 \cdot W_R \cdot W_{\text{OE}}$
- Empty Volume: $V_{\text{void}} = k_{vv} \cdot V_{\text{tot}}$
- Payload Volume: $V_{\text{pay}} = W_{\text{pay}}/\rho_{\text{pay}}$
- Crew Volume: $V_{\text{crw}} = (V_{\text{pcrv}} + k_{\text{crw}}) \cdot N_{\text{crw}}$

The typical ranges of the sizing parameters in the above equations are provided by Czysz and VDK after personal discussions with European Aerospace engineers.

$5.0 < V_{un} < 7.0\ m^3$
$11 < f_{crw} < 12\ m^3/person$
$0.02 < k_{vs} < 0.04$
$0.25 < k_{ve} < 0.75\ m^3/person$
$0.10 < k_{vv} < 0.20$
$0.90 < k_{crw} < 2.0\ m^3/person$
$5 < V_{pcrv} < 6\ m^3/person$

Table 3.4: Typical ranges of the volume parameters

Solving for the empty weight, we arrive at the following equation:

$$W_{\text{OE}} = \frac{\tau \cdot S_{\text{pln}}^{1.5} \cdot (1 - k_{vv} - k_{\text{vs}}) - (v_{\text{pcrw}} - k_{\text{crw}}) \cdot N_{\text{crw}} - W_{\text{pay}}/\rho_{\text{pay}}}{(WR - 1)/\rho_{\text{ppl}} + k_{\text{ve}} \cdot TW_0 \cdot W_R} \tag{3.33}$$

$$W_{dry_V} = W_{\text{OE}} - W_{\text{pay}} - f_{crw} \cdot N_{crw} \tag{3.34}$$

3.5.1 TPS Sizing

For the sizing of the TPS, and therefore to calculate the required thickness and resulting weight, the results obtained from a code developed in Ref.[36] are considered as reference. The code calculates temperatures using a transient, nonlinear, implicit, one-dimensional finite element solution technique, and includes the thermal and mass models of the considered TPS concepts. The thermal analysis was validated by comparing the results with those of a more accurate two-dimensional finite element analysis (EAL).

A direct interface between the TPS and a smooth aluminum structure, 2.54 mm thick, is assumed, as depicted in the figure.3.7

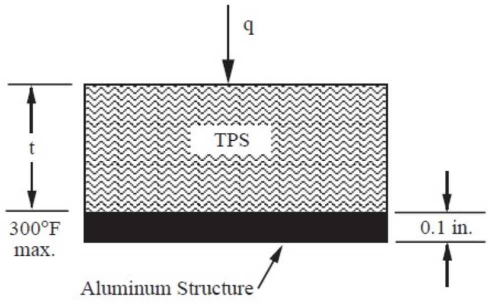

Figure 3.7: Simplified thermal model of TPS sizing problem

The inner surface of the structure is assumed to be adiabatic or fully insulated, with a maximum temperature limited to 422 K. Thermal flux is then applied to the outer surface of the TPS, and its required thickness is sized to meet the temperature limitation of the inner structure. The values of thermal flux considered are those obtained from the aerothermodynamic analysis in section 3.4.3, which, when integrated over the flight time, provide the thermal load. For simplicity, in this thesis work, the emissivity of the TPS is considered the same for each TPS concept. The graphs extrapolated from [36] are reported below, illustrating the influence of thermal load on the weight of various TPS concepts. The value obtained from entering these graphs following the thermal flow analysis will be considered as part of the overall structural index, and it will be referred to as I_{TPS}.

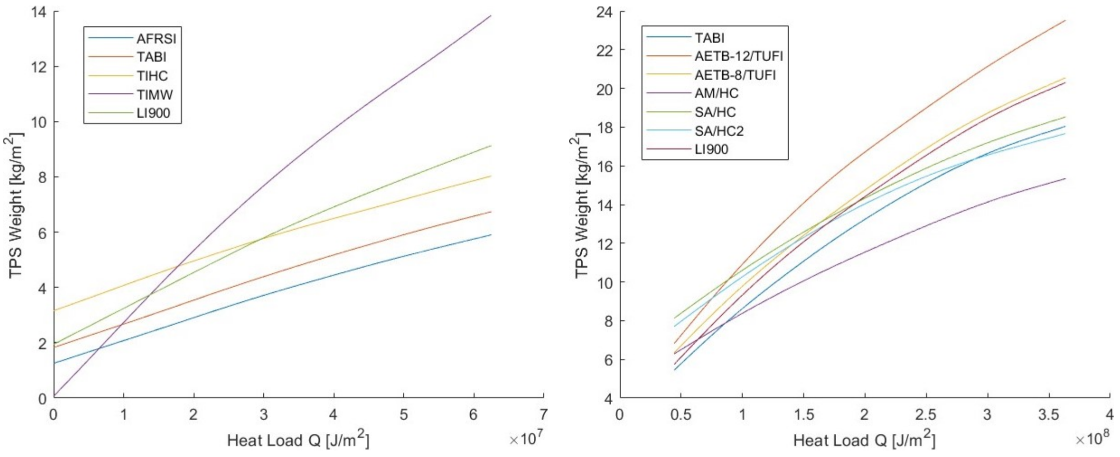

Figure 3.8: Thermal load influence on the TPS weights

The blanket TPS designs are generally lighter than other concepts across nearly all considered conditions. AFRSI stands out as the lightest option, with TABI only slightly heavier. Titanium Multiwall (TIMW) is not competitive in weight for most conditions due to its relatively high thermal conductivity but assumes a similar weight to blanket designs at very low integrated heat loads. For higher heating profiles, the AMHC metallic concept tends to have the lowest weight, followed by TABI. Furthermore, LI-900 tiles, AETB-8 tiles, Superalloy Honeycomb (SA/HC), and Advanced Superalloy Honeycomb (SA/HC2) metallic concepts exhibit similar weights across the range of parameters considered. In general, metallic concepts are lighter at higher temperatures due to the use of low-density fibrous insulations, but they offer lower high-temperature tolerance compared to tiles.

3.6 Multiple Matching Chart

The matching chart used for conventional aircraft contains the various high-level mission requirements in terms of thrust-to-weight ratio and wing loading, and defines a 'performance-oriented' design space. By analyzing the requirement curves of the various mission phases, it is possible to determine whether a configuration falls within the design space or does not meet a requirement.

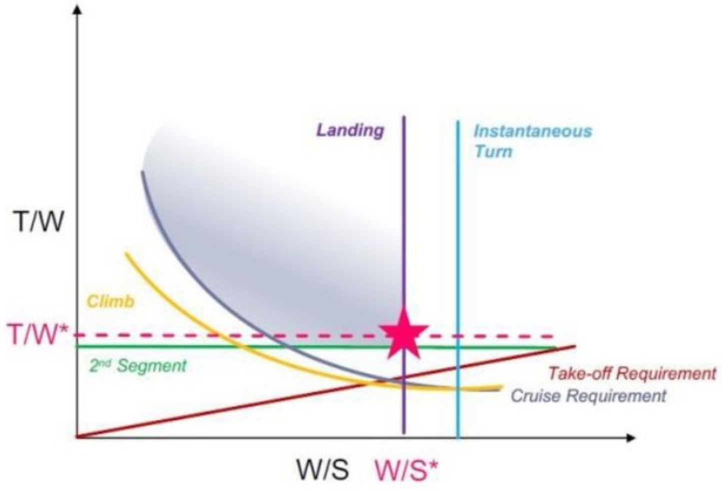

Figure 3.9: typical Matching Chart for conventional aircraft [14]

It can be noted in Figure 3.9 that the design space is identified by the shaded area, where the design point is located. The design point determines the configuration of the vehicle. In the case of the spaceplane, a single matching chart can not be used due to the different mission profiles and propulsion systems. Rather, the curves in the matching chart representing the requirements need to be extended to supersonic and hypersonic flight regimes, where the engine may operate in a different mode or be a completely different engine than the one used in the subsonic. Also, the space access requirement needs to be verified. Therefore, the T/W parameter cannot be normalized based on a specific altitude (e.g. sea level). In these cases, the comparison between subsonic, supersonic, and hypersonic requirements no longer has any meaning. In the study of the mission of a SSTO, the multiple matching chart approach is used, where the performance and high-level requirements are considered separately for each speed regime. [14]. However, it is necessary to consider a geometric consistency parameter between the different flight regimes for each matching chart in order to obtain a global design point. Indeed, if the T/W requirements may change during the mission, the design planform surface is considered fixed. Another parameter to consider is the amount of propellant consumed to reach a certain mission phase: if you know the weight ratio, you can normalize the planform load at a certain altitude. In this way, the minimum normalized W/S value determined in all phases can be considered as a design parameter for the entire mission. In general, to define the matching charts it is necessary to identify the flight requirements through equations in which T/W = f(W/S), or that T/W is constant or that W/S is constant.

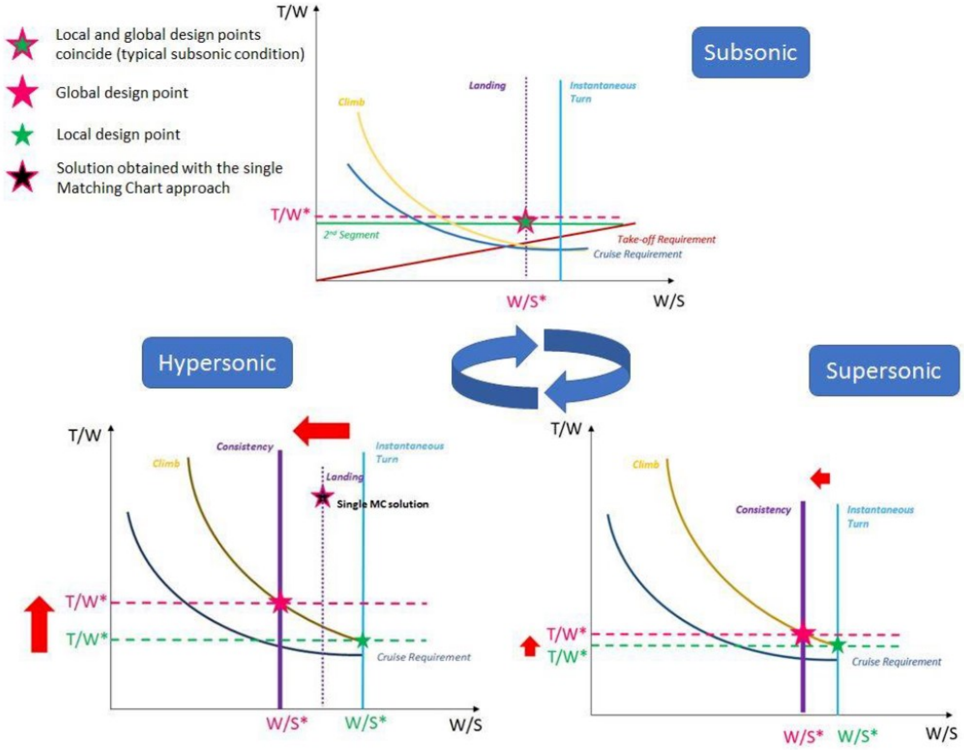

Figure 3.10: example of Multiple Matching Chart approach [14]

3.6.1 Take-off requirement

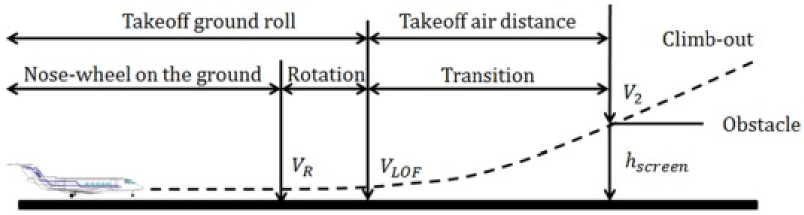

Figure 3.11: Take-off maneuver scheme

The horizontal take-off is the mission phase in which the vehicle leaves the ground and overcomes a fictitious obstacle at a height defined by the regulations (35ft or 50ft for FAR25). The takeoff procedure is divided into 3 phases: Taxiing, Maneuvering and Climbing. All three phases are included in the definition of 'take-off field length', which is one of the key design requirements for the HTOL spacecraft concept. Since the intention is to use existing runways, the vehicle must fall into the category of FAR25 certification requirements if it weighs more than 12500 lb [5670 *kg*].
Assuming that the aerodynamic drag on the ground and the rolling friction between the wheels and the runway are not taken into account, the required take-off distance can be defined as T/W = f(W/S) as follows

$$\left(\frac{T}{W}\right)_{TO} = \frac{W_{TO_{kg}}/S}{\rho_0 \sigma TOP_{25} C_{L_{TO}}} \tag{3.35}$$

For FAR 25 regulated aircrafts, the Takeoff Parameter (TOP25) results $TOP_{25} = 3.2808\ l_{TO}/37.5\ [kg/m^2]$ according to Roskam methodology [41].

3.6.2 Second segment requirement

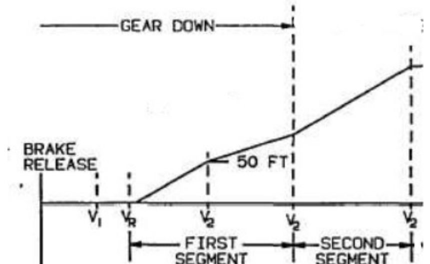

Figure 3.12: Second segment scheme

The second segment climb is the flight path that begins once the fictitious obstacle has been overcome up to 400 feet, keeping the flight speed constant. According to the FAR regulation, in a multi-engine configuration, the climb gradient must be 0.024 for 2-engine aircraft, 0.027 for 3-engine aircraft and 0.03 for 4-engine aircraft. In addition, the climb gradient must also be guaranteed in the event of one inoperative engine.
The second segment requirement can be defined as follows:

$$\left(\frac{T}{W}\right)_{2nd} = \frac{N_{\text{engines}}}{N_{\text{engines}} - 1}\left(\frac{1}{E_{2nd}} + G_{2nd}\right) 1/\sigma \tag{3.36}$$

This requirement does not depend on the planform load.

3.6.3 Climb and cruise requirements

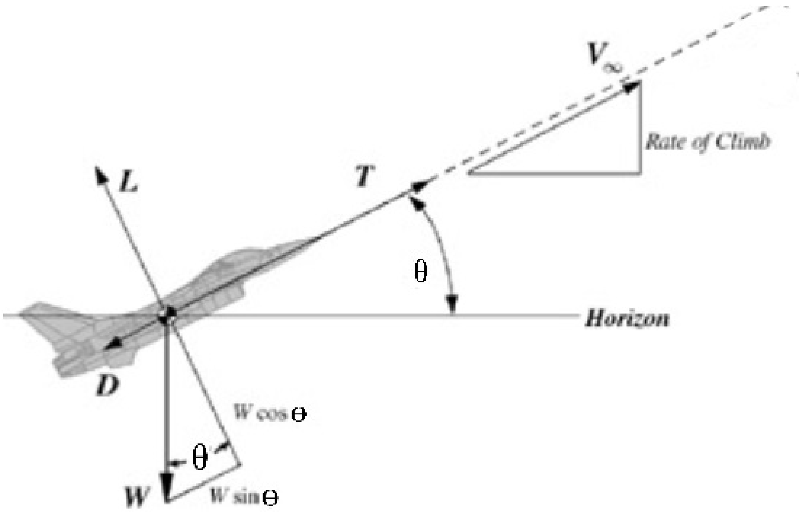

Figure 3.13: Simplified aircraft forces scheme in flight

Following the flight path, the requirements for the climb and cruise phases must be defined. For a mission in low Earth orbit, the dynamic equations for flight over a non-rotating, homogeneous, spherical Earth determine the equations for the motion of the vehicle. The climb and cruise requirements define the condition under which the vehicle's motion is uniform and remains along the direction of the flight path. The equations of motion are as follows:

- Climb phase

$$L = W\cos\theta \tag{3.37}$$

$$T = D + W\sin\theta \tag{3.38}$$

- Cruise phase

$$L = W \tag{3.39}$$

$$T = D \tag{3.40}$$

Lift and drag can be expressed as follows:

$$L = qC_LS \tag{3.41}$$

$$D = qC_DS \tag{3.42}$$

if the T/W term is inserted into the equations of motion and extrapolated, the following equations are obtained, which represent the flight requirements:

- Climb requirement

$$\left(\frac{T}{W}\right)_{\text{climb}} = \left(\frac{q_\infty C_D}{gW_{kg}/S} + G_{\text{climb}}\right)\frac{1}{\pi\sigma^*} \tag{3.43}$$

- Cruise requirement

$$\left(\frac{T}{W}\right)_{\text{cruise}} = \left(\frac{q_\infty C_D}{gW_{kg}/S}\right)\frac{1}{\pi\sigma^*} \tag{3.44}$$

It is necessary to divide these two requirements for each flight regime and insert the values of the performance parameters that are representative of the specific flight segment. The requirements are corrected using the density rate to match the initial conditions of the different flight regimes. Taking into account the chosen trajectory, the two requirements are included or not in the different matching charts depending on whether or not a climb and/or cruise phase is present.

3.6.4 Landing requirement

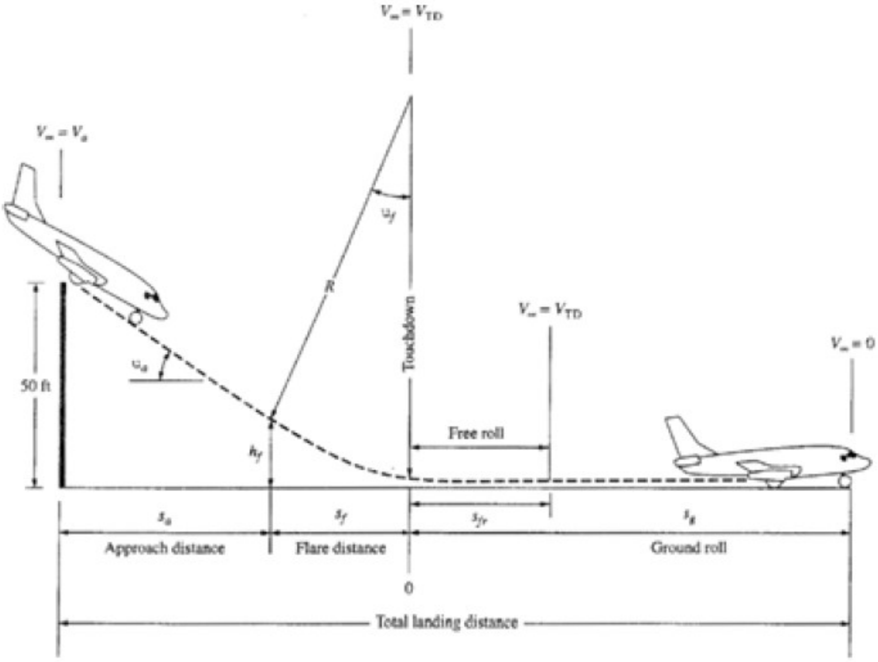

Figure 3.14: Landing maneuver scheme

In the configuration selected at the concept design level, the descent and landing phase takes place without the use of the propulsion system. The standard landing procedure for conventional aircraft then applies. The landing maneuver enables the vehicle to complete the flight phase and come to a complete stop after touching down on the ground. The maneuver consists of 4 phases: First, the vehicle is in the landing approach phase to gradually descend after overcoming a fictitious obstacle in accordance with the regulations (50 feet). It then performs a pre-touchdown connection retraction, called a flare, which reduces the vertical component of the speed at which touchdown occurs (in general, it is desirable to have a vertical speed of less than 0.5 m/s at touchdown) and a free roll phase, i.e. a time interval after ground contact during which the vehicle moves along the track without any braking action being applied, and finally the braking phase, which decelerates the vehicle until it stops.

The model used to derive the landing requirement comes from Loftin statistics, which is based on the evaluation of some semi-empirical parameters for the landing phase of jet engines.

The landing field length is determined by multiplying the available landing distance by a correction coefficient:

$$s_{LFL} = 1.6 s_{ALD} \tag{3.45}$$

Where s_{ALD} is expressed as: $s_{ALD} = \frac{V_{app}^2}{k_{app}^2}$
k_{app} is the approach parameter, which according to the Loftin model has the following value: $k_{app} = 1.7\sqrt{\frac{m}{s^2}}$
From the equilibrium equation at landing the following equation is derived:

$$\left(\frac{W_{kg}}{S}\right)_{LDG1} = \frac{1.23\rho_0 \sigma C_{L_{MAX}} k_{app}^2 s_{LFL}}{2g} \tag{3.46}$$

$$\left(\frac{W_{kg}}{S}\right)_{LDG1} = k_L \sigma C_{L_{MAX}} s_{LFL} \tag{3.47}$$

In order to obtain a requirement for W/S that can be consistent with the other flight phases, the weight value must be traced back to the initial condition of each flight phase as follows:

$$\left(\frac{W_{GTOW_{kg}}}{S}\right)_{LDG2} = \frac{k_L \sigma C_{L_{MAX}} s_{LFL}}{W_{GLW_{kg}}/W_{GTOW_{kg}}} \tag{3.48}$$

3.6.5 Orbit Reaching requirement

This section has been added to extend the applicability of the matching chart to access-to-space vehicles. Therefore, a formulation of T/W as a function of wing loading has been sought, which can take as input the requirement to achieve orbital velocities. The detailed procedure for obtaining the formulation is presented in the thesis work of Roberto Cau. Below the key steps to the final formulation are reported. We have started from the rocket equation:

$$\Delta V = I_{\text{sp}} \cdot g_0 \cdot \ln\left(\frac{W_i}{W_f}\right) \tag{3.49}$$

Rewriting specific impulse as a function of thrust, through some algebraic steps, the term T/W can be isolated.

$$\frac{T}{W} = \frac{W_{\text{ppl}}}{W} \frac{\Delta V \; g_0}{t_b \; \ln\left(\frac{W_i}{W_i - W_{\text{ppl}}}\right)} \; . \tag{3.50}$$

At this point, we have considered a semi-empirical formulation of the Propulsion Index given in Ref. [33], which expresses it as a function of the maximum Mach number attainable with the propulsion system used:

$$I_P = \frac{\rho_{\text{ppl}}}{\text{WR} - 1} = 107.6 \cdot 10^{-0.081 \cdot M_{\max}} \tag{3.51}$$

From which the value of W_{ppl} can be explicitly expressed. Furthermore, referring to [33], a formulation of the planform surface area S_{pln} was used to relate the final weight to the surface area.

$$S_{pln} = \left[\frac{I_p}{I_{str}} \cdot \frac{K_w}{\tau} \cdot \frac{1}{K_v} \cdot \frac{1}{K_{str}} \cdot \left(1 + \frac{W_{\text{pay}}}{W_f} \right) \right]^{1.409} \tag{3.52}$$

in which the parameters K_v and K_{str} are:

$$K_v = 1.1857[0.4(\rho_{pay}/175.6)^{0.123} - 6.867e^{-3}\tau^{-1} + 8.2777e^{-4}\tau^{-2} - 2.811e^{-5}\tau^{-3}] \tag{3.53}$$

.

$$K_{str} = (0.317)\tau^{0.205} \tag{3.54}$$

Substituting into 3.51 and defining the parameters a and b as follows:

$$\begin{cases} a = I_{str} \cdot \tau \cdot K_v \cdot K_{str} \\ b = I_p \cdot K_w \end{cases} \tag{3.55}$$

This yields a value of W_{ppl} as a function of the surface, one of the key parameters for defining the matching chart. Upon substituting the W_{ppl} value obtained into equation 3.50, we obtain:

$$\frac{T}{W} = \frac{\rho_{\text{ppl}}\ W_{pay}\ K_W}{(W/S)^{-0.71}\, W^{1.71}\ a - W\ b} \cdot \frac{\Delta V}{g_0\ t_b\ \ln\left(W \Big/ \left(W - \frac{\rho_{\text{ppl}}\ W_{\text{pay}}\ K_W}{(W/S)^{-0.71}\ W^{0.71}\ a\ -\ b} \right) \right)} \tag{3.56}$$

This equation represents a new formulation of the thrust-to-weight (T/W) ratio in relation to the wing weight-ratio (W/S), referring to the orbit reaching requirement. This is designed to be applied to each mission phase, according to the MMC approach.

The following parameters are considered as input data for the ascent phases.

tau	Küchemann parameter τ
W	Maximum Weight (of the phase)
W_{pay}	Payload mass
M_{max}	Maximum Mach number (of the phase)
h	Maximum altitude (of the phase)
ROC	Rate Of Climb (of the phase)
I_{str}	Structural index
ρ_{pay}	Payload mean density
ΔV	Change in velocity (of the phase)

Table 3.5: Input of the orbit reaching requirement function

3.7 Convergence Logic

For a given slenderness parameter of the vehicle, the plan area is iterated until the available weight and volume correspond to the required weight and volume. In this procedure, the equations for the empty weight, which are obtained from the weight and volume budget, are used as convergence parameters.

$$W_{dry_W} - W_{dry_V} = 0 \tag{3.57}$$

This is the first iteration of the code, which already provides a dimensioned configuration. Subsequently, the variable τ is iterated so that the wing loading at take-off is consistent with the maximum wing loading limit obtained through the multiple matching chart study.

$$W/S_{sizing} - W/S_{mmc} = 0 \tag{3.58}$$

Of course, modifying the parameter τ results in changes to geometric dimensions, so it must be considered that the iteration on the surface area needs to be reiterated. The last consideration concerns the thrust values. The available thrusts in each considered flight phase must be greater than or equal to the required thrusts obtained through the matching chart study. If the condition is not met, and database engines are installed, the number of engines is increased. However, if the engine performances from analytical models are considered, the statistical values of thrust are increased proportionally and used as input for the next iteration. This is because the engine does not have fixed performance but can be 'designed' directly for the mission. In the case of an engine selected from the database, thus with a fixed ETW (Engine Thrust Weight), the procedure alters the weight of the propulsion system, so the iterations on τ and the surface area must be incorporated within it. In the other case, it is possible to adjust the required ETW for the engine, but an increase in weights may not be avoided due to the feasibility verification of the volumes. Even in this case, it is necessary to iterate the parameters S_{pln} and τ within it.

Chapter 4

Case Study: SKYLON

This chapter provides a more detailed overview of the SKYLON, as presented in section 2.2.2 of chapter 2, the chosen vehicle for the case study to which the developed methodology has been applied. The main informations are taken from the SKYLON Users Manual (Ref. [42]. SKYLON is an SSTO spaceplane fully reusable, currently under development by the British company Reaction Engines Limited (Reaction) since 2009. This vehicle takes off and lands on a runway like a conventional aircraft, thus belonging to the category of HTOL vehicles. This aspect constitutes a significant advantage in its operational management; for instance, it can be prepared for departure in a hangar near the runway, thereby avoiding the complex and expensive transportation challenges associated with launch facilities. To increase the achievable mass ratio for an SSTO, SKYLON exploits the SABRE engine technology, a combined-cycle LOX/LH2 engine able to cover the entire mission of the vehicle by working both in airbreathing mode and rocket mode. The mass ratio obtained is estimated to be approximately 23 percent more than using a pure rocket system. The engine's airbreathing mode, used by the takeoff phase, is switched to pure rocket mode after accelerating the vehicle to Mach 5.14 at 28.5 km altitude, until reaching Low Earth Orbit. Once the climb phase and the subsequent insertion into orbit are completed, the payload is deployed and the orbital operations are accomplished. After that, the vehicle returns to Earth. The re-entry interface is passed at an altitude of 120 km, where the vehicle maneuvers to control temperatures and thermal loads and to meet the pre-calculated requirements for return to the spaceport. Following a gliding approach similar to the Space Shuttle, it reaches the landing runway.

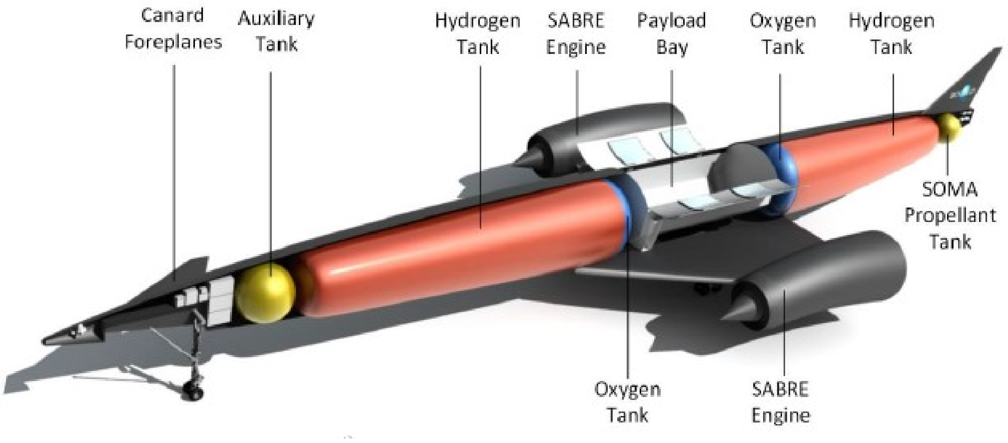

Figure 4.1: Skylon Layout [42]

As it can be seen in Figure 4.1, the SKYLON configuration has a slender airframe which, in contrast to designs of other SSTO spaceplanes, features a distinct separation between the fuselage and the delta wing (positioned approximately halfway up the fuselage). This characteristic has been demonstrated to be optimal in terms of weight, lift, and volume, but poses challenges in the management of heat flows, as it gives rise to localized high heat fluxes that necessitate an active cooling system. The payload bay of this vehicle is positioned at the wing attachment point, and the payload is loaded from above. The axial symmetric nacelles, on which the SABRE engines are mounted, are positioned on the wingtips.

The majority of the fuselage is dedicated to housing the hydrogen cryogenic tanks, with a smaller portion reserved for the liquid oxygen tanks. This allocation is facilitated by the fact that, during the initial phase of ascent, the oxidizer is sourced from the outside air, in addition to the low density of hydrogen that leads to larger fuel tanks. The placement of the tanks is associated with equilibrium problems that impact the vehicle. These challenges were resolved through meticulous aerodynamic design and the implementation of differential burning of the propellant in the two tanks.

The SKYLON is equipped with control surfaces for atmospheric flight, including Canard foreplanes for pitch control, ailerons for roll control, and an aft fin for yaw control. During the pure rocket phase, control is achieved through differential engine thrust. Additionally, it features a SOMA (SKYLON Orbital Maneuvering Assembly) module with engines designed for orbital maneuvers, fed by a specific propellant tank.

Regarding the materials, the primary structure consists of a frame composed of titanium struts reinforced with silicon carbide, while the aluminum tanks are suspended using Kevlar ties. The frame is further covered with sheets of reinforced

glass ceramic material, serving as both the aeroshell and the primary thermal protection system, supplemented by a multilayer metallic heat shield.
The dimensional and mass characteristics of the SKYLON are reported in table 4.1.

Fuselage Length	83.1 m
Wing Span	26.8 m
Height	13.5 m
Max Payload Mass	15.0 tons
Gross Take-Off Mass	325.0 tons
Dry Mass	53.4 tons

Table 4.1: Dimensional and mass characteristics of the SKYLON D1 spaceplane.

The work carried out involves verifying the results of the tool created in the MATLAB environment based on the methodology considered. It begins with the definition of requirements.
To remain consistent with the case study, the mission objective chosen is to deliver a payload of 15000 kg to a target orbit at an altitude of 100 km. Selecting the airbreathing + rocket propulsion strategy and thus choosing the SABRE engine, the vehicle configuration can be modeled as a wing body. The SABRE engine, being capable of operating in both airbreathing and all-rocket phases, has the transition between the two modes set at Mach 5. Additionally, following the Skylon reference, it is decided not to carry crew onboard, thus avoiding acceleration limitations.
For the ascent modeling, it is necessary to identify the dynamic pressure for the ascent phase at constant dynamic pressure. This information is extrapolated from the Skylon's transition point between airbreathing and all-rocket phases, located at an altitude of 28500 km and presenting a flight speed at Mach 5. Mission requirements also include the required runway length for takeoff and landing, as well as the latitude of the launch base. Since the ascent graph in the Skylon user manual does not show cruise phases, it is assumed in our code that the launch base is at the equator and at sea level. Finally, a value is assumed for the index of industrial capacity according to the maturity and technological advancement required for the vehicle design.
Below is a table listing all the initial inputs for defining the vehicle's configuration concept, propulsion strategy, and mission.

Payload Weight	15.0 tons
Target Orbit	100 km
Propulsion Strategy	Airbreathing+Rocket
Engine	SABRE
Transition Mach	5
Configuration Concept	Wing Body
Crew Number	0
Dynamic Pressure	26.123 kPa
Launch base Altitude and Latitude	sea level, 0°
Take-off lenght	4000 m
Landing lenght	1900 m
Industrial Capacity Index	37.7 m^{-1}

Table 4.2: Requirements, Assumptions and Constraints

The maximum value of the ICI parameter has been assumed according to the estimates provided in Ref.[33].
The analysis of the tool starts with the application of the trends derived from statistical analysis, from which the following values are obtained:

GTOW	328049.4 kg
W dry	68988.9 kg
Take off Thrust	2337 kN
S_{pln}	449.9 m^2

Table 4.3: Statistic analysis applied for the case study

The values of the reference surface and empty weight will only serve as a final comparison, while the takeoff weight and thrust will be used as inputs for the first iterative cycle.

Case Study: Mission Analysis

We proceed with the initial comparison between the mission profile obtained and that provided by REL for the Skylon. The modeling is referred only to the airbreathing part as it is functional to performance calculation; the rocket phase did not require modeling since constant performance was assumed and the trajectory considered to reach orbit is a Hohmann transfer.
Considering the attainment of a constant dynamic pressure $q = 26.123\,[kPa]$ and the formulations provided by Billing [38], the following ascent profile is obtained:

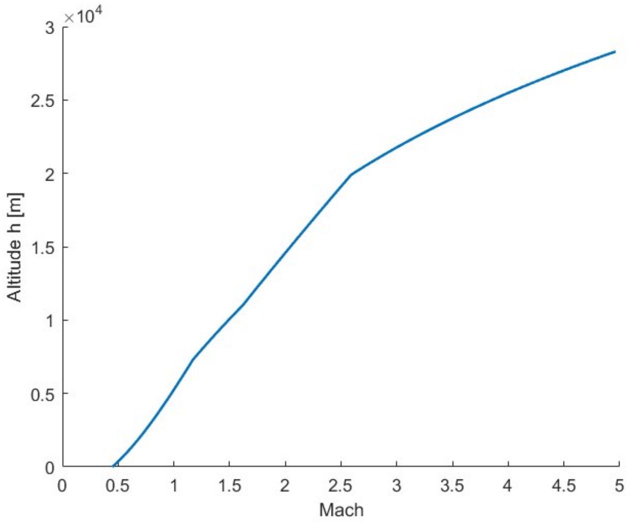

Figure 4.2: Airbreathing ascent phase

A more accurate modeling of the ascent trajectory, including the rocket phase, was conducted using ASTOS by Roberto Cau [39] and is subsequently reported in section 4.
On the other hand, the re-entry phase was modeled considering the following input data, in line with typical values for glide re-entry vehicles. The vehicle weight considered is the dry weight, and the surface area is the planform surface, both obtained after ascent performance analyses and estimations of vehicle weights and volumes.

Vehicle Re-entry Weight	55648 tons
S_{pln}	382 m^2
C_D	0.5
L/D	1.5

Table 4.4: Re-entry phase Input Data

The re-entry profile is derived (Section 3.3).

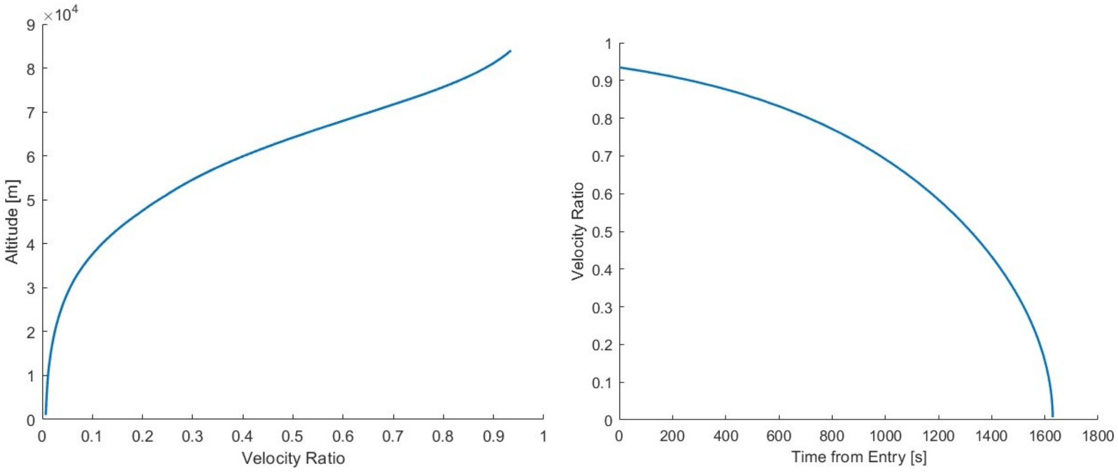

Figure 4.3: Altitude, Time from Entry and Velocity Ratio

Case study: Performance data

- Engine performance

The performance of a reduced model of the SABRE engine provided by REL, as reported in the propulsion database in Appendix A.3, is implemented into the tool. A multiplicative coefficient is then applied to make the thrust levels compatible with the SKYLON configuration, based on the maximum thrust data provided by Longstaff, R. [22] and the Skylon user manual [42], from which the vacuum thrust value is also taken.

- Aerodynamics performance

Regarding aerodynamics, it was chosen to directly incorporate the Skylon database into the algorithm of the tool, as reported in Appendix A.2. The lift and drag coefficients were extrapolated in order to maximize the lift-to-drag ratio for the first ascent phase, resulting in an average value of α of approximately 5°. The trend of aerodynamic efficiency is reported in comparison with the empirical model of Curran applied to our configuration.

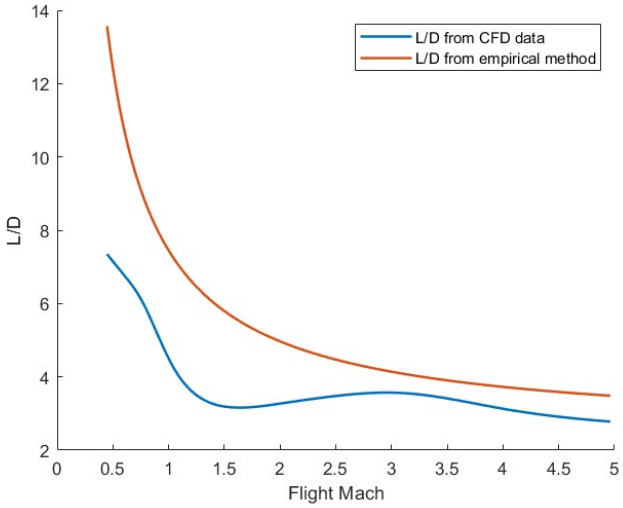

Figure 4.4: Comparison of aerodynamic efficiency during the airbreathing phase between CFD analysis (Appendix A.2) and Curran Method (3.4.2)

The empirical method by Curran is therefore acceptable for Mach numbers greater than three, while it overestimates aerodynamic efficiency at lower speeds. For the study of the matching chart, specific values of the aerodynamic coefficients were identified:

$C_{L_{TO}}$	0.687
$C_{L_{LDG}}$	0.864
$C_{D_{\text{turbcruise}}}$	0.0620
$C_{D_{\text{turbclimb}}}$	0.0401
$C_{D_{\text{ramcruise}}}$	0.0311
$C_{D_{\text{ramclimb}}}$	0.0399

Table 4.5: Aerodynamic coefficients for the Multiple Matching Chart

- Aerothermodinamics performance

From the glide reentry profile, data are extracted to perform the aerothermodynamic analysis (Section 3.4.3), necessary for TPS sizing. Below are the obtained results for wall temperature, heat fluxes, and thermal loads.

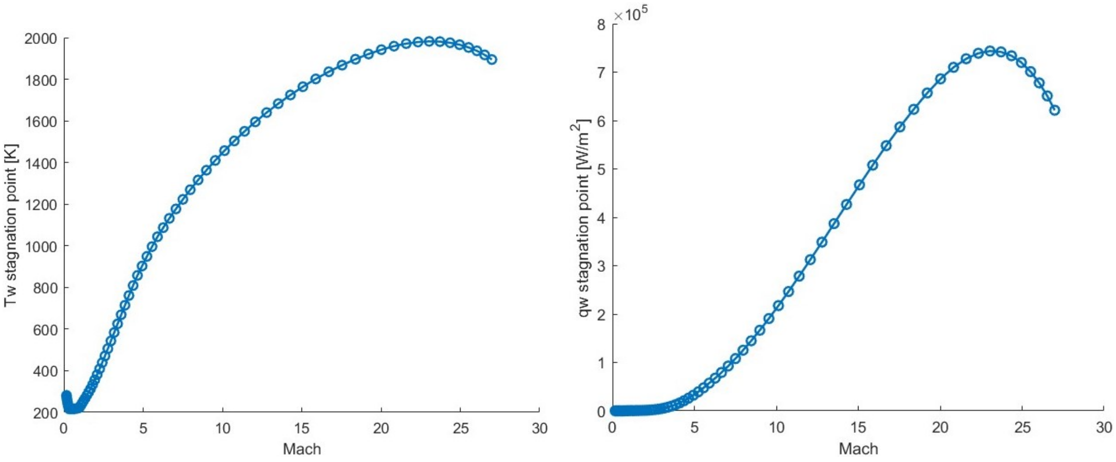

(a) Wall temperature during reentry

(b) Heat flux during reentry

Figure 4.5: Stagnation point

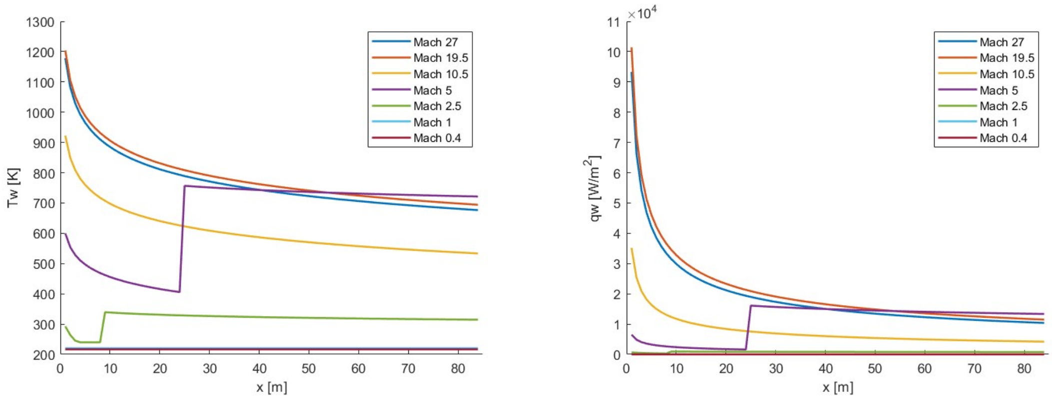

Figure 4.6: Isomach lines of wall temperature and heat flux along the SSTO x-body

It is noted from Figure 4.5 that the stagnation point temperatures can reach up to 2000 Kelvin, hence the consideration of materials capable of tolerating high temperatures is necessary. From Figure 4.6, it is observed how the wall temperature and heat fluxes decrease along the x-body in the laminar case, then rise significantly in some phases of re-entry due to turbulent flow detachment.

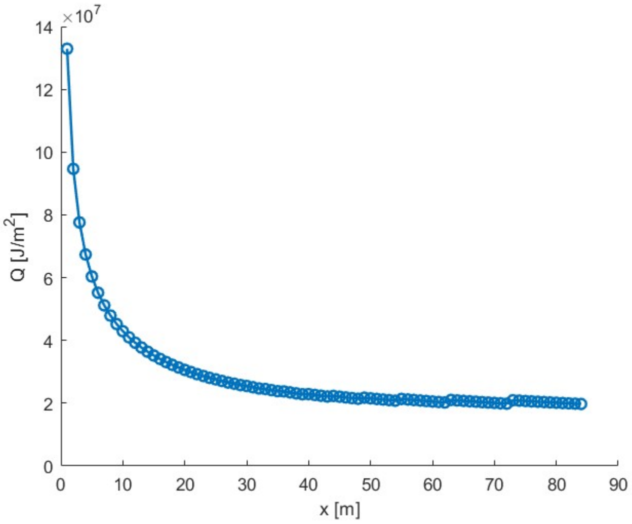

Figure 4.7: Heat Loads along the SSTO x-body

Values for TPS sizing are extracted from the thermal load trends (Figure 4.7).

- Weight Ratio

For the weight ratio calculation, the ascent is divided into 4 phases.

Phase:	**SABRE mode:**	**End condition(s):**
Take off	Airbreathing (turbojet)	Altitude: 50 m
First Climb phase	Airbreathing (turbojet)	Mach: 2.2
Second climb phase	Airbreathing (turbo-ramjet)	Altitude $\geq$ 28000, Mach: 5
Third climb phase	Rocket	Altitude $\geq$ 90 km

Table 4.6: Ascent phases description

We assume a maximum pitch angle for the first ascent phase of about 8° and for the second ascent phase of about 3°, which ends with the switch of propulsion mode from airbreathing to rocket. The Weight Ratio calculation (Section 3.4.4) via the design tool yields the following values, referring to the different flight phases:

WR_{TO}	1.01
WR_{turbojet}	1.0341
$WR_{\text{turbo-ramjet}}$	1.0386
WR_{rocket}	4.4485

Table 4.7: Ascent phase Weight Ratio

Since engine ignition is not required during re-entry, the total weight ratio is:

$$WR = 4.8254 \tag{4.1}$$

Case study: TPS Sizing

To obtain the TPS weight index $I\text{str}_{\text{TPS}}$, the obtained thermal load values are entered into the graphs provided in Section 3.5.1, and the respective TPS weight per unit area for various material types is observed.

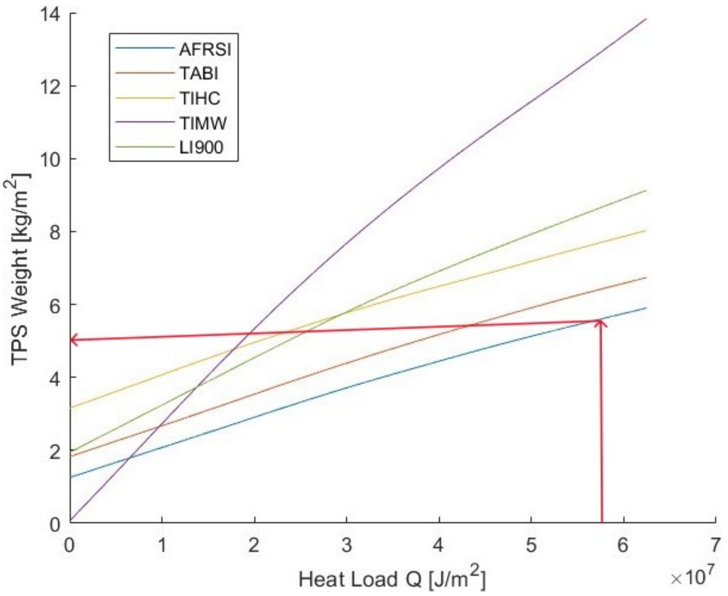

Figure 4.8: Example of TPS weight evaluation procedure

For our case study, the TPS that ensures the minimum weight is selected, resulting in:

$$I\text{str}_{\text{TPS}} = 4.047 \tag{4.2}$$

Case study: Multiple Matching Chart

In this section, following the procedure outlined in Section 3.6, the multiple matching charts related to the different operational phases of the SABRE engine are presented: turbojet, turbo-ramjet, rocket. Tables 4.8, 4.9, 4.11 summarize the design points for the respective ascent phases.

Planform loading (turbojet mode)	893.34 kg/m^2
Thrust-to-Weight ratio (turbojet mode)	0.76

Table 4.8: Design point for turbojet mode ascent phase

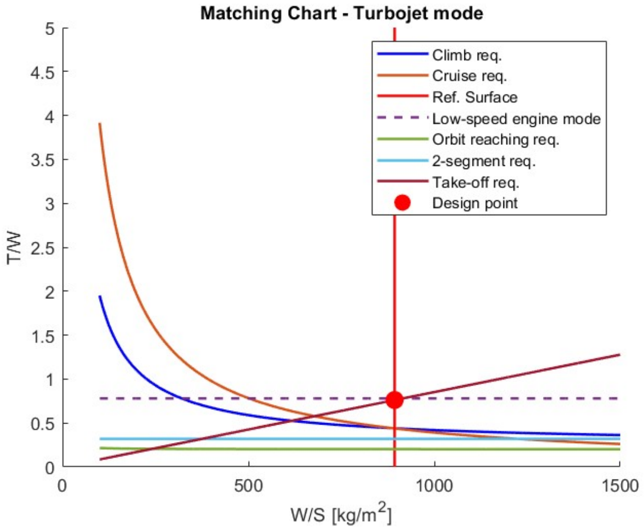

Figure 4.9: SKYLON D1 matching in turbojet mode

Planform loading (turbo-ramjet mode)	855.34 kg/m^2
Thrust-to-Weight ratio (turbo-ramjet mode)	0.64

Table 4.9: Design point for turbo-ramjet mode ascent phase

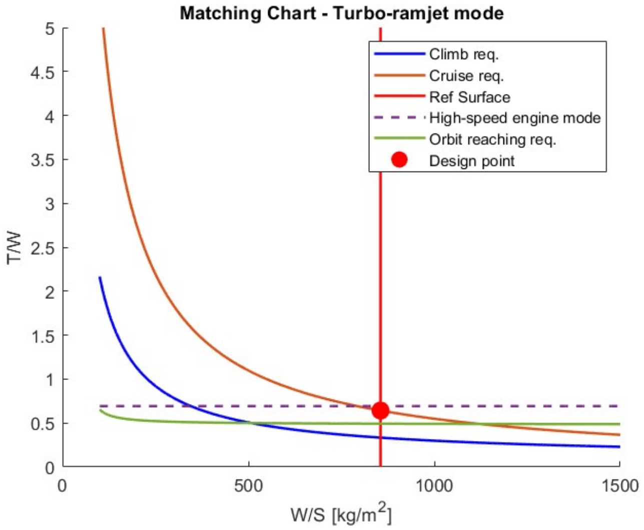

Figure 4.10: SKYLON D1 matching in turbo-ramjet mode

Planform loading (rocket mode)	823.56 kg/m^2
Thrust-to-Weight ratio (rocket mode)	1.30

Table 4.10: Design point for rocket mode ascent phase

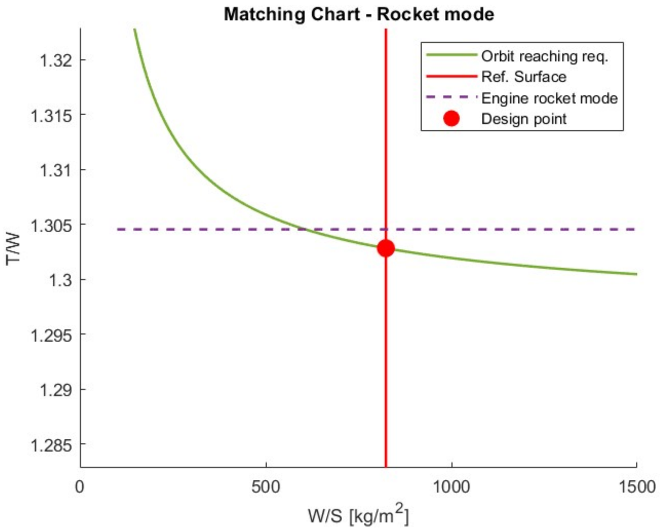

Figure 4.11: SKYLON D1 matching in rocket mode

The diagrams depict all trends with reference to their corresponding initial condition. The red lines shown in the turbo-ramjet mode and rocket mode graphs represent the additional consistency requirements. The operational condition of the turbo-ramjet is assumed to begin around Mach 2.2 (16500 m). In the respective turbo-ramjet operational condition graph, it is observed that the most stringent requirement is for cruise. This is because cruise is assumed at the TOC (28500 m) of the airbreathing phase, while for the climb requirement, average altitude and speed levels are considered. In these operational conditions, the SABRE allows adequate thrust levels, although it is always considered at maximum throttle. Furthermore, it is observed that the orbit reaching requirement is not greatly influenced by changes in the size of the reference surface. From the required landing length, high values of Wing Loading are obtained, but they are compatible with the range required for a Horizontal Takeoff Horizontal Landing SSTO (Ref. [33]).

Case study: Weight and Volume Budget

In this section, the weights and volumes of the main system items obtained are reported, followed by a verification of the results by comparing them to the values of the SKYLON D1 provided by REL and reported in Table 4.1.

From the definition of the Industry Capacity Index, information regarding the value of the Structural Index is obtained:

$$Istr = 10\frac{Ip}{ICI} = 17.77\ kg/m^2 \tag{4.3}$$

It is verified that it falls within the range considered in the table 3.3.
From the sizing procedure, the following is obtained:

Kuchemann parameter τ	0.217
Planform Surface S_{pln}	382 m^2
Wet Surface S_{wet}	1321 m^2

Table 4.11: SSTO vehicle size

The following tables report the outputs of the design tool that define the weight and volume budget.

Gross Take-off Weight	
Payload Weight	15000 kg
Crew Weight	0 kg
Dry Weight	55648 kg
Structure Weight	18137 kg
Subsystems Weight	13030 kg
Engine Weight	13404 kg
TPS Weight	5346 kg
Margin	11.48 %
Propellant Weight	270260 kg
LH2 Weight	61434 kg
LOX Weight	208826 kg
TOT	340909 kg

Table 4.12: Weight Budget SSTO

Total Volume	
Payload Volume	300 m^3
Crew Volume	0 m^3
Empty Volume	162.02 m^3
Subsystems Volume	37.40 m^3
Engine Volume	66.47 m^3
Propellant Volume	1054.18 m^3
LH2 Volume	871.16 m^3
LOX Volume	183.02 m^3
TOT	1620.15 m^3

Table 4.13: Volume Budget SSTO

These data were obtained following the three iterations highlighted in section 3.7. The figure below shows the variations in Gross Take-off Weight and Propellant Weight during the iterative cycle necessary to meet the wing loading constraint given by the matching chart once the configuration with two engines has already been reached.

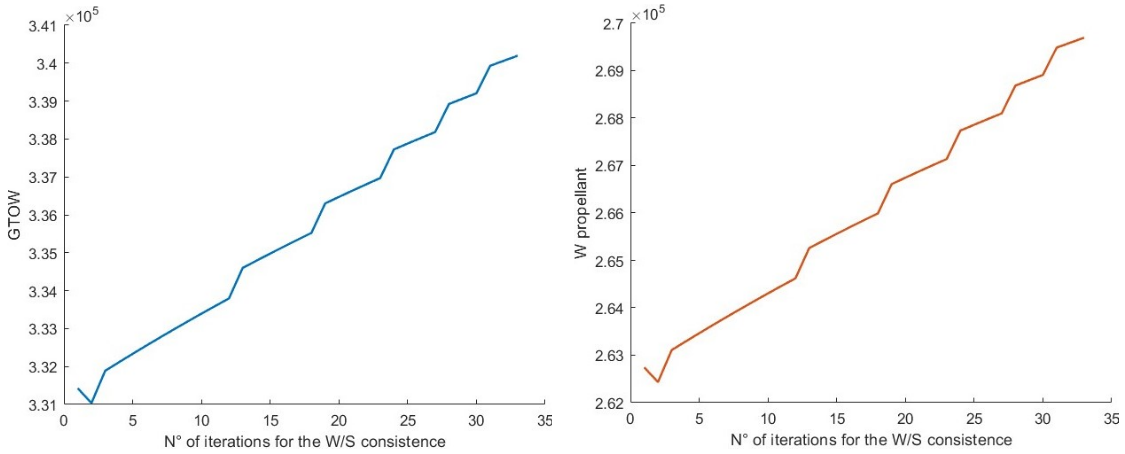

Figure 4.12: Gross Take-off Weight and Propellant Weight variation during the iterative process

This iteration was carried out by varying τ, starting from the maximum value identified within the range for launchers with airbreathing engines. It is observed that both the takeoff weight and the amount of propellant required to reach orbit increase as the slenderness parameter τ decreases.

Below is reported the error of the different quantities compared to the values of the SKYLON. The SKYLON planform area is not reported in any open-source paper; therefore, it was calculated using the OpenVSP software by inputting the geometric data provided in the SKYLON Users' Manual.

Data comparison			
	SSTO tool	SKYLON D1[42]	error [%]
GTOW	340909 kg	325000 kg	4.9 [%]
W_{dry}	55648 kg	53400 kg	4.2 [%]
S_{pln}	382 m^2	685 m^2	44 [%]

Table 4.14: Tool validation for the SKYLON case study

The estimated error for the weight budget is considered acceptable. However, the planform area value obtained from the sizing code appears to be significantly underestimated, approaching more closely the reference wing area value calculated for the SKYLON from the dimensions provided in the SKYLON Users' Manual ([42]) $S_{\text{wing}} = 345m^2$. Despite this, the dimensional parameters K_w and τ fall within the range of wing-body launchers identified in the chapter "Transatmospheric Launcher Sizing" [33]. If an attempt were made to increase the planform area, and thus decrease the wing loading, the configuration would become much heavier. Additionally, it would require higher thrusts according to the requirements curves plotted in the matching chart.

We could approach the SKYLON values provided by REL by considering higher values of ICI, which according to the author could already be achievable today given that the estimate of the maximum ICI value was provided about 20 years ago (see Ref [33]). However, it should be noted that the coefficients used for the weight and volume estimates reported in Table 3.3 and Table 3.4 have been considered with minimum values, so the obtained concept design is not conservative at all. Another way to reduce weights is to consider a higher wing loading, but this would lead to an increase in the value of tau, entering the "Hypersonic glide" category, and reducing lift levels, besides having to verify the requirements for take-off and landing lengths. Furthermore it has been noted, from the insertion of different inputs, that an improvement in the performance of the airbreathing phase engine with a fixed ICI leads to an overall increase in weights because the structural index is forced to increase. It should be noted that these two parameters are still to be considered independent, so if the level of technological maturity is not given as a parameter, it is possible that the propulsion index increases without the structural index being varied, and vice versa.

Finally, the on-board Oxygen to Fuel Ratio is evaluated. From the values obtained through the design tool, the possible position occupied by the SABRE can be identified in the following graph reported in Curran's Transatmospheric Launcher Sizing chapter [33].

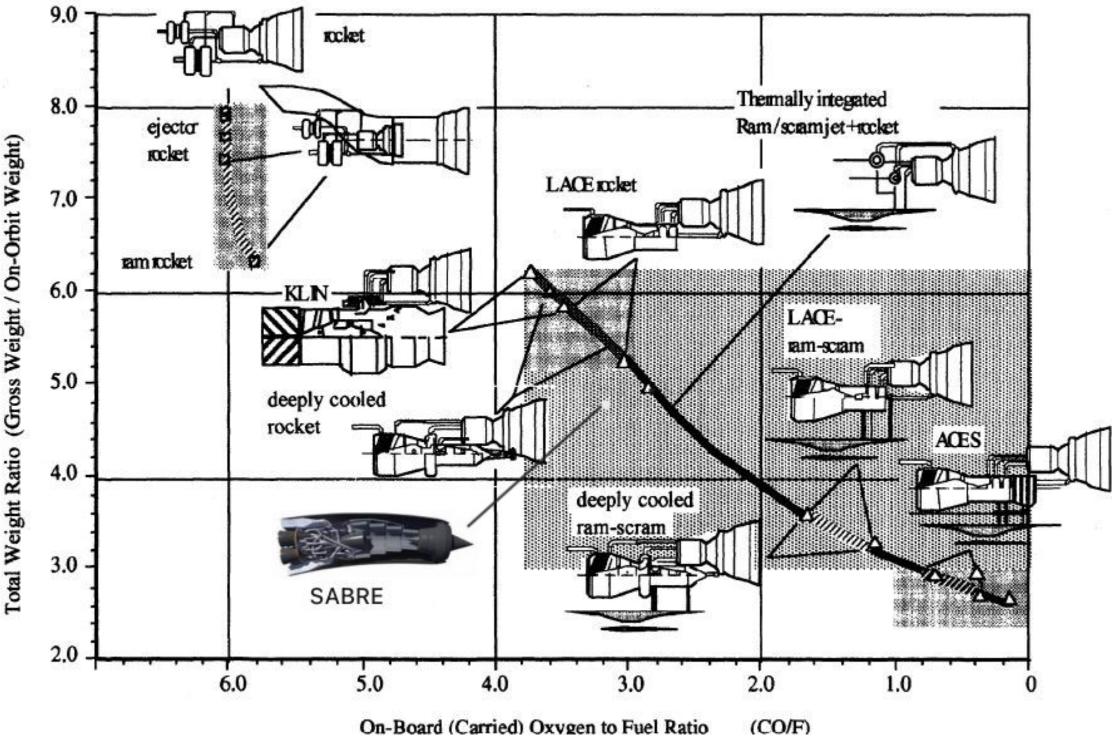

Figure 4.13: Weight Ratio to orbit and carried oxygen depending on different propulsion cycles

Ascent Phase validation with ASTOS

In this section, the results of the ascent analysis performed in the ASTOS environment in Cau's thesis [39] are reported, inputting the values obtained from the tool. With the current vehicle configuration obtained from the tool, it is possible in simulation to reach an altitude of 100 km. There is residual propellant present at the end of the ascent, indicating that the tool with the inputs considered does not provide the optimized configuration.

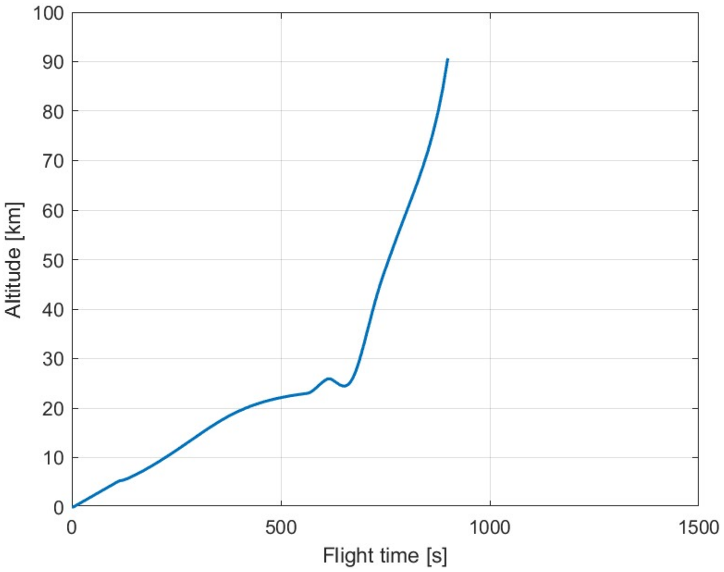

Figure 4.14: Simulated Mission Profile [39]

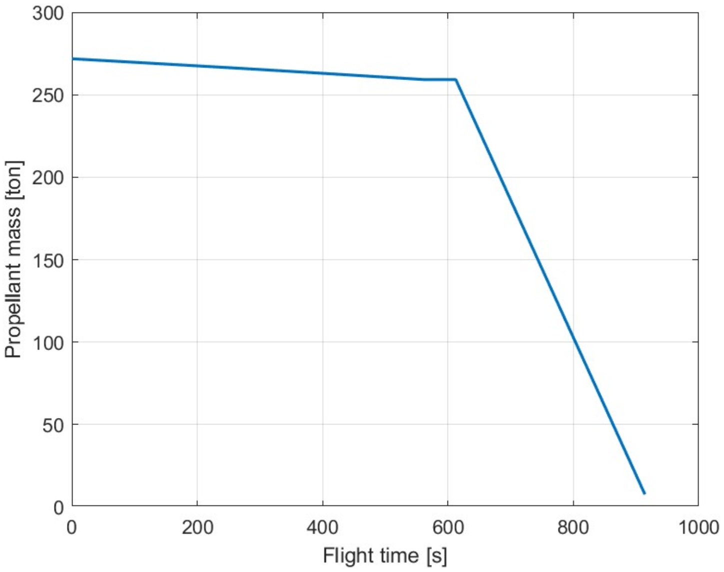

Figure 4.15: Simulated propellant consumption during the ascent [39]

Chapter 5

Conclusion

Access to space is seeking new configurations of innovative launchers that allow for amortization of production costs due to their ability to be reused in a short period. The main space and aerospace agencies for the development of these vehicles use design synthesis systems to simplify the design process and make it clearer. The conceptual design phase is very important in this context, where the majority of the flight vehicle configuration and mission concepts are determined. Therefore, the focus of this thesis has been on developing a concept design methodology for a reusable Horizontal Takeoff Horizontal Landing SSTO vehicle, which could allow for a very high flight frequency without the need for dedicated launch bases or integration with other stages.

The thesis begins with a comprehensive literature review covering design methodologies, past and present SSTO projects, and a review of the state of the art in propulsion systems and thermal control systems that could be adapted to a Horizontal Takeoff Horizontal Landing (HTOL) SSTO. Data collection regarding weights, thrusts, and dimensions of SSTO HTOL vehicle concepts is included to perform a statistical analysis useful for estimating thrust-to-weight ratios. The values obtained from the statistical analysis will be used as input in the tool for conceptual design development. Aerodynamic, Engine, and Thermal Protection System databases were then created, aiming to provide a multifidelity approach for performance analysis. The methodology underlying the tool refers to the VDK and Czysz sizing methodology but also includes control over available thrusts and mission requirements through the use of the Multiple Matching Chart, as well as an aerothermodynamic analysis leading to TPS sizing. It should be noted the introduction of a formulation extrapolated from the space access requirement, which extends the applicability of the Multiple Matching Chart approach, initially designed for hypersonic vehicles.

From the required payload mass and volume towards a target orbit, selecting the propulsion strategy and vehicle configuration concept, as well as the transition

conditions from airbreathing mode to rocket mode if present, the tool provides a sizing of the vehicle concept and an estimation of the thrusts.
The tool has been verified against SKYLON D1 using the dedicated SABRE database, within accepted percent error for the weight estimates, while there is an inconsistency regarding the dimensions of the planform area.
In the future, a graphical user interface could be integrated to make it easier and more user-friendly. Additionally, the available databases could be expanded if new configurations similar to the case study are developed, as well as more accurate analytical models could be included for performance calculation, as the data available today are limited and moderately reliable.

Appendix A

Databases

A.1 Size and Weight database

This section reports a database of the SSTO concepts considerated, with their main sizing characteristiscs.

Vehicle	**GTW [tons]**	**Wpay [tons]**	**Wdry [tons]**	**H [m]**	**Wing Span [m]**	**Surface $[m^2]$**	**Lenght [m]**	**T_0 [kN]**	**T_v [kN]**
Star-raker	2278.8	100	330.4	556000	110	3814	104.3	20480	
Boeing Langley SSTO	1250	30	175		70		102	8583	
ALRS 205	855.5		128.7		39.93	790	59.13		9273
Hyperion	363	9.07	70.51		29.87	548.128	54.56	2138.1	
JSP Spaceplane	350	20	110		29		94		
Skylon	325	15	53.4	200000	26.8	345	83.3	2700	4000
Hyperplane 271	271	26.3	87						
Argus	270.08	9.1	34.25		16.18	262.45	52.12	1602	
Tupolev-2000	260	10		200000	14	760		900	
HOTOL	250	8	50	300000	28.3			3153	
X-30	140	15	60		36			1370	
Lazarus	81.65	2.27	18.87	161000	18.75	136.1	31.33	480.572	645.212
Lynx Mark	5	0.65		103000	7.3		9.1	52	
Ascender	4	0.35		100000	7.62		13.72	32	88.3

A.2 Aerodynamic database

This section reports a database of the aerodynamic characteristics of some vehicles that can be associated with those of a single-stage to orbit with horizontal take-off and landing.

Mach	**Alpha**	**CL**
0.30	-5	-0.23
0.30	0	-0.01
0.30	5	0.23
0.30	10	0.47
0.30	15	0.69
0.30	20	0.84
0.30	25	0.86
0.30	30	0.86
0.60	-5	-0.24
0.60	0	0.01
0.60	5	0.26
0.60	10	0.49
0.60	15	0.69
0.60	20	0.83
0.60	25	0.87
0.60	30	0.96
0.80	-5	-0.26
0.80	0	0.01
0.80	5	0.26
0.80	10	0.51
0.80	15	0.72
0.80	20	0.86
0.80	25	0.95
0.80	30	1.01
0.95	-5	-0.32
0.95	0	0.01
0.95	5	0.31
0.95	10	0.63
0.95	15	0.90
0.95	20	1.09
0.95	25	1.21
0.95	30	1.25
1.05	-5	-0.32
1.05	0	0.01
1.05	5	0.28
1.05	10	0.57

Mach	**Alpha**	**CD**
0.30	-5	0.024
0.30	0	0.007
0.30	5	0.029
0.30	10	0.083
0.30	15	0.159
0.30	20	0.281
0.30	25	0.396
0.30	30	0.494
0.60	-5	0.024
0.60	0	0.012
0.60	5	0.037
0.60	10	0.088
0.60	15	0.176
0.60	20	0.293
0.60	25	0.408
0.60	30	0.555
0.80	-5	0.034
0.80	0	0.017
0.80	5	0.029
0.80	10	0.086
0.80	15	0.191
0.80	20	0.313
0.80	25	0.452
0.80	30	0.594
0.95	-5	0.071
0.95	0	0.042
0.95	5	0.059
0.95	10	0.137
0.95	15	0.262
0.95	20	0.411
0.95	25	0.572
0.95	30	0.751
1.05	-5	0.076
1.05	0	0.051
1.05	5	0.073
1.05	10	0.144

1.05	15	0.85
1.05	20	1.09
1.05	25	1.29
1.05	30	1.39
1.20	-5	-0.29
1.20	0	-0.02
1.20	5	0.24
1.20	10	0.50
1.20	15	0.77
1.20	20	1.01
1.20	25	1.21
1.20	30	1.34
1.60	-5	-0.28
1.60	0	-0.07
1.60	5	0.17
1.60	10	0.41
1.60	15	0.63
1.60	20	0.83
1.60	25	1.03
1.60	30	1.21
2.00	-5	-0.24
2.00	0	-0.05
2.00	5	0.17
2.00	10	0.37
2.00	15	0.56
2.00	20	0.74
2.00	25	0.92
2.00	30	1.09
3.00	-5	-0.17
3.00	0	-0.02
3.00	5	0.14
3.00	10	0.29
3.00	15	0.43
3.00	20	0.59
3.00	25	0.75
3.00	30	0.91
4.00	-5	-0.12
4.00	0	-0.01
4.00	5	0.11
4.00	10	0.23

1.05	15	0.264
1.05	20	0.428
1.05	25	0.631
1.05	30	0.831
1.20	-5	0.073
1.20	0	0.051
1.20	5	0.068
1.20	10	0.130
1.20	15	0.240
1.20	20	0.399
1.20	25	0.594
1.20	30	0.800
1.60	-5	0.066
1.60	0	0.042
1.60	5	0.054
1.60	10	0.108
1.60	15	0.200
1.60	20	0.335
1.60	25	0.506
1.60	30	0.724
2.00	-5	0.064
2.00	0	0.039
2.00	5	0.051
2.00	10	0.095
2.00	15	0.178
2.00	20	0.296
2.00	25	0.457
2.00	30	0.655
3.00	-5	0.049
3.00	0	0.029
3.00	5	0.039
3.00	10	0.078
3.00	15	0.142
3.00	20	0.240
3.00	25	0.374
3.00	30	0.550
4.00	-5	0.039
4.00	0	0.024
4.00	5	0.034
4.00	10	0.068

4.00	15	0.36
4.00	20	0.51
4.00	25	0.67
4.00	30	0.81
5.50	-5	-0.09
5.50	0	-0.01
5.50	5	0.08
5.50	10	0.18
5.50	15	0.30
5.50	20	0.44
5.50	25	0.59
5.50	30	0.75
5.94	9	0.19
6.67	12	0.23
7.48	13	0.26
8.58	12	0.24
10.13	11	0.18
12.19	8	0.13
14.95	4	0.08
16.97	1	0.07

4.00	15	0.125
4.00	20	0.210
4.00	25	0.333
4.00	30	0.496
5.50	-5	0.032
5.50	0	0.024
5.50	5	0.029
5.50	10	0.054
5.50	15	0.105
5.50	20	0.186
5.50	25	0.303
5.50	30	0.460
5.936	9.324	0.068
6.673	11.583	0.086
7.483	12.779	0.095
8.577	12.453	0.088
10.131	10.626	0.064
12.189	7.512	0.042
14.952	3.510	0.027
16.969	0.907	0.024

Table A.1: Aerodynamic data of the SKYLON for air-breathing phase (source: MORE&LESS project, Politecnico di Torino)

Mach	**Alpha**	**Cl (ext)**	**Cd (ext)**
0.30	-6	0.002	0.025
0.30	-4	0.047	0.025
0.30	-2	0.090	0.028
0.30	0	0.133	0.035
0.30	2	0.180	0.042
0.30	4	0.229	0.053
0.30	6	0.281	0.069
0.50	-6	0.003	0.026
0.50	-4	0.048	0.025
0.50	-2	0.093	0.030
0.50	0	0.137	0.034
0.50	2	0.185	0.045
0.50	4	0.235	0.054
0.50	6	0.288	0.073

Table A.2 continued from previous page

0.70	-6	0.003	0.028
0.70	-4	0.049	0.027
0.70	-2	0.094	0.030
0.70	0	0.139	0.036
0.70	2	0.187	0.045
0.70	4	0.238	0.057
0.70	6	0.293	0.074
0.80	-6	0.005	0.029
0.80	-4	0.051	0.028
0.80	-2	0.097	0.031
0.80	0	0.142	0.037
0.80	2	0.191	0.046
0.80	4	0.243	0.059
0.80	6	0.299	0.076
0.95	-6	0.007	0.033
0.95	-4	0.056	0.034
0.95	-2	0.103	0.037
0.95	0	0.152	0.044
0.95	2	0.202	0.054
0.95	4	0.256	0.068
0.95	6	0.313	0.086
1.05	-6	-0.004	0.041
1.05	-4	0.047	0.041
1.05	-2	0.095	0.045
1.05	0	0.144	0.051
1.05	2	0.195	0.061
1.05	4	0.249	0.075
1.05	6	0.306	0.093
1.20	-6	-0.009	0.042
1.20	-4	0.039	0.042
1.20	-2	0.085	0.045
1.20	0	0.131	0.051
1.20	2	0.180	0.060
1.20	4	0.232	0.073
1.20	6	0.287	0.090
1.50	-6	-0.020	0.041
1.50	-4	0.024	0.040
1.50	-2	0.066	0.042

Table A.2 continued from previous page

1.50	0	0.109	0.047
1.50	2	0.154	0.055
1.50	4	0.202	0.066
1.50	6	0.254	0.081
1.70	-6	-0.026	0.039
1.70	-4	0.016	0.038
1.70	-2	0.057	0.040
1.70	0	0.098	0.044
1.70	2	0.141	0.051
1.70	4	0.188	0.061
1.70	6	0.237	0.076
2.00	-6	-0.032	0.037
2.00	-4	0.007	0.035
2.00	-2	0.046	0.036
2.00	0	0.085	0.039
2.00	2	0.126	0.045
2.00	4	0.169	0.055
2.00	6	0.215	0.068
3.00	-6	-0.043	0.029
3.00	-4	-0.010	0.026
3.00	-2	0.023	0.025
3.00	0	0.056	0.027
3.00	2	0.092	0.031
3.00	4	0.130	0.038
3.00	6	0.169	0.048
4.00	-6	-0.033	0.011
4.00	-4	-0.004	0.010
4.00	-2	0.025	0.010
4.00	0	0.055	0.012
4.00	2	0.086	0.017
4.00	4	0.118	0.024
4.00	6	0.151	0.034
5.00	-6	-0.029	0.009
5.00	-4	-0.004	0.007
5.00	-2	0.022	0.008
5.00	0	0.049	0.010
5.00	2	0.076	0.014
5.00	4	0.104	0.021

Table A.2 continued from previous page

5.00	6	0.133	0.029
6.00	-6	-0.025	0.008
6.00	-4	-0.003	0.006
6.00	-2	0.020	0.007
6.00	0	0.044	0.009
6.00	2	0.068	0.013
6.00	4	0.094	0.018
6.00	6	0.121	0.027
7.00	-6	-0.022	0.007
7.00	-4	-0.002	0.006
7.00	-2	0.019	0.006
7.00	0	0.040	0.008
7.00	2	0.063	0.011
7.00	4	0.087	0.017
7.00	6	0.113	0.025
8.00	-6	-0.019	0.007
8.00	-4	-0.001	0.005
8.00	-2	0.017	0.006
8.00	0	0.037	0.007
8.00	2	0.058	0.011
8.00	4	0.081	0.016
8.00	6	0.106	0.023

Table A.2: Aerodynamic data of the Stratofly, clean version (source: Politecnico di Torino)

A.3 Engines database

Mach number	F_u [kN]
0.0034	612.8280
0.1100	621.5371
0.1845	629.3827
0.3976	647.6756
0.5005	656.3859
0.5645	653.7396
0.7849	644.9161
0.8810	637.8855

Mach number	F_g [KN]
0.0048	613.3992
0.0690	629.1537
0.1474	645.7871
0.3935	700.061
0.4755	717.5696
0.5753	731.5885
0.7179	745.6223
0.8106	754.3947

0.9805	636.9760
1.2043	647.3933
1.2966	653.4835
1.3747	658.7040
1.6021	669.1200
1.6802	670.8420
1.7762	674.3070
2.0106	680.3474
2.0818	672.4508
2.1671	666.2985
2.4018	650.4729
2.4730	642.5763
2.5618	637.2974
2.7823	618.8529
2.8606	613.5777
2.9530	606.5483
3.1451	588.1137
3.2340	580.2109
3.3407	571.4272
3.5292	551.2447
3.6323	544.2115
3.7319	536.3049
3.9275	515.2452
4.0164	509.0917
4.1125	500.3117
4.3400	483.6141
4.4254	479.2110
4.5178	473.0562
4.7454	456.3585
4.8094	451.9630
4.9054	444.0577
5.0014	442.2748

0.9211	762.2994
0.9924	769.3163
1.0851	787.7026
1.1600	801.7128
1.3561	831.4973
1.4274	846.3802
1.5059	857.7696
1.7233	883.1916
1.8160	894.586
1.8980	902.4806
2.0976	920.9044
2.1939	922.686
2.2830	928.8352
2.5040	936.7784
2.6002	941.1821
2.6857	943.834
2.9103	954.4004
3.0030	957.9288
3.1027	957.9637
3.3059	961.5307
3.4021	965.0604
3.5126	965.973
3.7443	967.802
3.8441	971.3329
3.9367	970.4913
4.1577	974.9385
4.2361	977.5879
4.3074	977.6128
4.5711	980.327
4.6566	979.4829
4.7529	981.2646
4.9845	983.9675

Table A.3: Propulsive data of the SABRE engine (source: Reaction Engine Ltd.)

A.4 TPS database

Source: Parametric Weight Comparison of Advanced Metallic, Ceramic Tile, and Ceramic Blanket Thermal Protection Systems by David E. Myers, Carl J. Martin, and Max L. Blosser ([36])

Item	**Thickness (cm)**	**Density (kg/m^3)**	**Unit Weight (kg/m^2)**
Protective Coating	0.025	2002	0.51
Outer Fabric	0.028	985	0.27
Insulation	t	96	0.5t
Inner Fabric	0.023	985	0.22
RTV Adhesive	0.020	1410	0.29
Edge Closeout	0.028	985	0.007t

Table A.4: Weight Calculations for AFRSI

Item	**Thickness (cm)**	**Density (kg/m^3)**	**Unit Weight (kg/m^2)**
Protective Coating	0.025	2002	0.527
Outer Fabric	0.028	881	0.273
Insulation	t	96	0.5t
Corrugation	0.023*2	881	0.450
Inner Fabric	0.023	881	0.224
RTV Adhesive	0.020	1410	0.268
Edge Closeout	0.028	985	0.007t

Table A.5: Weight Calculations for TABI

Item	**Thickness (cm)**	**Density (kg/m^3)**	**Unit Weight (kg/m^2)**
Protective Coating (top)	0.03	1666	0.508
Protective Coating (side)	0.03	1666	0.0693t
LI900	t	144	0.750t
Densified Region	0.025	384	0.976
RTV Adhesive	0.020*2	1410	0.571
Nomex SIP	0.40	86.5	0.351

Table A.6: Weight Calculations for LI-900

Item	**Thickness (cm)**	**Density (kg/m^3)**	**Unit Weight (kg/m^2)**
Protective Coating (top)	0.25	800	2.03
Protective Coating (side)	0.05	800	0.042t
AETB-8	t	128	0.667t
RTV Adhesive	0.02	1410	0.571
Nomex SIP	0.40	86.5	0.351

Table A.7: Weight Calculations for AETB-8

Item	**Thickness (cm)**	**Density (kg/m^3)**	**Unit Weight (kg/m^2)**
Protective Coating (top)	0.025	800	2.03
Protective Coating (side)	0.05	800	0.042t
AETB-12	t	192	t
RTV Adhesive	0.020	1410	0.571
Nomex SIP	0.40	86.5	0.351

Table A.8: Weight Calculations for AETB-12

Item	**Thickness (cm)**	**Density (kg/m^3)**	**Unit Weight (kg/m^2)**
Titanium Sidewall	0.008	4533	0.024(t+0.976)
Titanium Multiwall	t	144	0.750t
RTV/Nomex Felt	0.48	197	151
Fasteners	n/a	n/a	0.298+0.006t

Table A.9: Weight Calculations for TIMW

Item	**Thickness (cm)**	**Density (kg/m^3)**	**Unit Weight (kg/m^2)**
IN617 Upper Facesheets	0.013*2	8345	2.226
Upper h/c core (IN617)	0.71	133	0.947
Q-Fiber	tx1	56	0.292tx1
Cerrachrome	tx2	96	0.50tx2
IN617 Sidewall	0.008	8345	0.043(tx1+tx2+4.345)
Ti Lower Facesheets	0.01	4437	1.035
Lower h/c core (Ti)	0.43	94.5	0.405
Fasteners	n/a	n/a	0.424+0.011(tx1+tx2)
RTV/Nomex Felt	0.48	197	0.151
Braze Alloy	n/a	n/a	0.464

Table A.10: Weight Calculations for SA/HC

Item	**Thickness (cm)**	**Density (kg/m^3)**	**Unit Weight (kg/m^2)**
IN617 Upper Facesheets	0.013*2	8345	2.226
Upper h/c core (IN617)	0.71	133	0.947
Saffil	t	50	0.260t
IN617 Sidewall	0.008	8345	0.043(t+4.345)
Ti Lower Facesheets	0.01	4437	0.844
Lower h/c core (Ti)	0.43	94.5	0.176
Fasteners	n/a	n/a	0.424+0.011t
RTV/Nomex Felt	0.48	197	0.151
Braze Alloy	n/a	n/a	0.415

Table A.11: Weight Calculations for SA/HC2

Item	**Thickness (cm)**	**Density (kg/m^3)**	**Unit Weight (kg/m^2)**
Ti Upper Facesheets	0.013*2	4437	1.181
Upper h/c core (IN617)	0.71	94.5	0.674
Q-Fiber	t	56	0.292t
Ti Sidewall	0.008	4437	0.023(t+4.345)
Ti Lower Facesheets	0.01	4437	0.844
Lower h/c core (Ti)	0.43	94.5	0.176
Fasteners	n/a	n/a	0.302+0.006t
RTV/Nomex Felt	0.48	197	0.151
Braze Alloy	n/a	n/a	0.122

Table A.12: Weight Calculations for TI/HC

Item	**Thickness (cm)**	**Density (kg/m^3)**	**Unit Weight (kg/m^2)**
PM2000 Upper Facesheets	0.013*2	7192	1.919
Upper h/c core (PM2000)	0.71	115	0.820
IMI Insulation	t	73	0.380t
PM2000 Sidewall	0.008	8345	0.037(t+3.515)
Ti Lower Face	0.01	4437	0.356
Ti Tubular Frame	0.43	4437	0.591
Fasteners	n/a	n/a	0.137
RTV/Nomex Felt	0.48	197	0.151
Braze Alloy	n/a	n/a	0.381

Table A.13: Weight Calculations for AMHC

Appendix B

Propulsion Analysis: Analytical Methods

Turbojet Mode

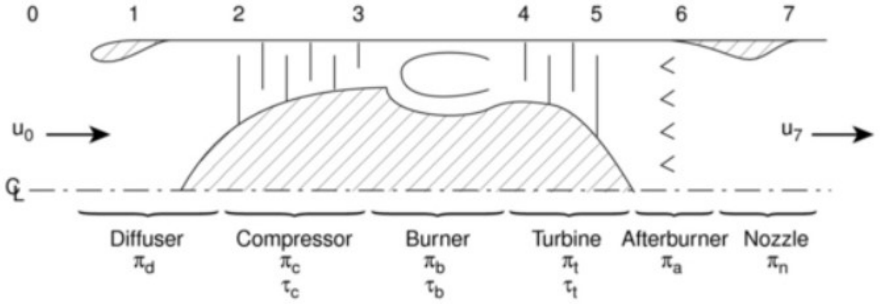

Figure B.1: Turbojet schematic featuring notations corresponding to its components [43]

Let's start with the expressions of thrust and propulsive impulse:

$$F = \dot{m}\left[(1+f)\,u_7 - u_0\right] + (p_7 - p_0)\,A_7 \tag{B.1}$$

and

$$I_{sp} = \frac{F}{gf\dot{m}} \tag{B.2}$$

The ratio between exit speed and inlet speed can be expressed as:

$$\frac{u_7}{u_0} = \frac{M_7}{M_0}\sqrt{\frac{\gamma R T_7}{\gamma R T_0}} \approx \frac{M_7}{M_0}\sqrt{\frac{T_7}{T_0}} \tag{B.3}$$

The ratio between exit static temperature and inlet static temperature can be manipulated algebraically as a function of the Mach number and the temperature changes across each component of the engine, going through the definition of the total exit temperature.

$$T_{t7} = T_0 \theta_0 \tau_c \tau_b \tau_T \tag{B.4}$$

with $\theta_0 = T_{t0}/T_0$. Considering the static outlet pressure equal to the static inlet pressure:

$$1 + \frac{\gamma - 1}{2} M_7^2 = \delta_0^{\frac{\gamma-1}{2}} \pi_c^{\frac{\gamma-1}{2}} \pi_T^{\frac{\gamma-1}{2}} = \theta_0 \tau_c \tau_T \left(= \frac{T_{t7}}{T_7} \right) \tag{B.5}$$

$$\frac{T_7}{T_0} = \frac{T_7}{T_{t7}} \frac{T_{t7}}{T_0} = \tau_b \tag{B.6}$$

substituting into the equation:

$$\frac{u_7}{u_0} = \sqrt{\frac{(\theta_0 \tau_c \tau_T - 1)\, \tau_b}{\theta_0 - 1}} \tag{B.7}$$

We now have two remaining steps to undertake. Firstly, we express τ_c in relation to τ_T, recognizing their correlation through the condition that the compressor's power consumption equals the turbine's power output. Secondly, we express the burner temperature ratio in relation to the burner's exit temperature (T_{t4} or more specifically $\theta_T = T_{t4}/T_0$), given that this constitutes the engine's highest temperature point and serves as a prevalent standard for evaluating diverse design configurations. The steady flow energy equation articulates that:

$$\dot{m} \Delta h_t = \dot{q} - \dot{w}_s \tag{B.8}$$

Given the adiabatic nature of both the compressor and turbine and considering the direct connection between the turbine shaft and the compressor shaft:

$$\dot{m}_c c_{p,c} \left(T_{t3} - T_{t2} \right) = \dot{m}_T c_{p,T} \left(T_{t4} - T_{t5} \right) \tag{B.9}$$

Assuming the mass flow and specific heats are the same between the compressor and turbine:

$$\left(\frac{T_{t3}}{T_{t2}} - 1 \right) \frac{T_{t2}}{T_0} = \frac{T_{t4}}{T_0} \left(1 - \frac{T_{t5}}{T_{t4}} \right) \tag{B.10}$$

$$\left(\tau_c - 1 \right) \theta_0 = \theta_T \left(1 - \tau_T \right) \tag{B.11}$$

That initial step established the connection between the temperature increase across the turbine and that across the compressor. The subsequent step involves expressing the temperature rise across the combustor in relation to $\theta_T = T_{t4}/T_0$.

$$\tau_b = \frac{\theta_T}{\theta_0 \tau_c} \tag{B.12}$$

and for an engine with an afterburner:

$$\tau_b = \frac{\theta_a}{\theta_T \tau_T} \tag{B.13}$$

By substituting our derived expressions for τ_b and τ_T into the equation for u_7/u_0 and subsequently into the initial thrust equation, we obtain the following specific thrust equation:

$$\frac{F}{\dot{m}a_0} = M_0 \left[\left\{ \left(\frac{\theta_0}{\theta_0 - 1} \right) \left(\frac{\theta_T}{\theta_0 \tau_c} - 1 \right) (\tau_c - 1) + \frac{\theta_T}{\theta_0 \tau_c} \right\}^{\frac{1}{2}} - 1 \right] \tag{B.14}$$

the specific thrust formulation can be inserted into the specific impulse equation:

$$I_{sp} = \frac{a_0 M_0 \left[\left\{ \left(\frac{\theta_0}{\theta_0 - 1} \right) \left(\frac{\theta_T}{\theta_0 \tau_c} - 1 \right) (\tau_c - 1) + \frac{\theta_T}{\theta_0 \tau_c} \right\}^{\frac{1}{2}} - 1 \right]}{gf} \tag{B.15}$$

Ramjet Mode

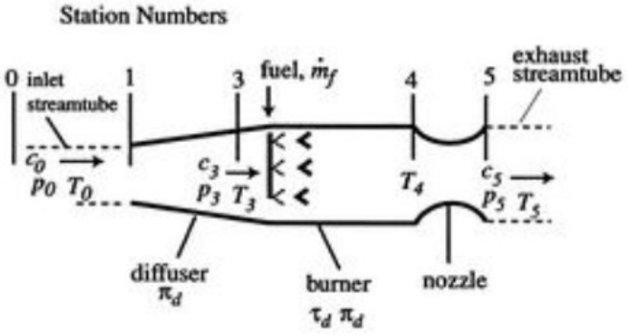

Figure B.2: Ramjet schematic diagram featuring notations corresponding to its components [43]

In a ramjet configuration, the expression for thrust, without considering the fuel mass flow, is:

$$F = \dot{m}\,(c_5 - c_0) \tag{B.16}$$

where c_5 and c_0 are respectively the exit and inlet flow velocities.
The equation can be rewritten to obtain the specific thrust:

$$\frac{F}{\dot{m}a_0} = \frac{c_5}{a_5}\frac{a_5}{a_0} - \frac{c_0}{a_0} = M_5\sqrt{\frac{T_5}{T_0}} - M_0 \tag{B.17}$$

where $a = \sqrt{\gamma RT}$ is the speed of sound.
Considering that the airflow in the diffuser and the burner is subsonic, the total pressure-to-static pressure ratios at exit and inlet are equal in value. Consequently, the Mach number at the turbine inlet and the Mach number at the nozzle exit are the same ($M_5 = M_0$).
At this point, we only need to calculate the temperature ratio between the exit and the inlet.

$$\frac{T_5}{T_0} = \frac{T_{t5}}{T_{t0}} = \frac{T_{t4}}{T_{t3}} = \tau_b \tag{B.18}$$

The final equation for the specific thrust is:

$$\frac{F}{\dot{m}a_0} = M_0\left(\sqrt{\tau_b} - 1\right) \tag{B.19}$$

Therefore, the specific impulse can be derived from the following relationship:

$$I_{sp} = \frac{F}{gf\dot{m}} \tag{B.20}$$

A good approximation to facilitate performance calculation is to consider the condition of stoichiometric fuel, meaning in the case of complete combustion.
Additionally, it is assumed that T_{t4} is constant.
Rewriting the parameter τ_b

$$\tau_b = \frac{T_{t4}/T_0}{T_{t3}/T_0} = \frac{\tau_{\max}}{\theta_0} \tag{B.21}$$

The specific impulse is

$$I_{sp} = M_0\left(\sqrt{\frac{\tau_{\max}}{\theta_0}} - 1\right)\frac{a_0}{f_{\text{stoic}}g} \tag{B.22}$$

Scramjet Mode

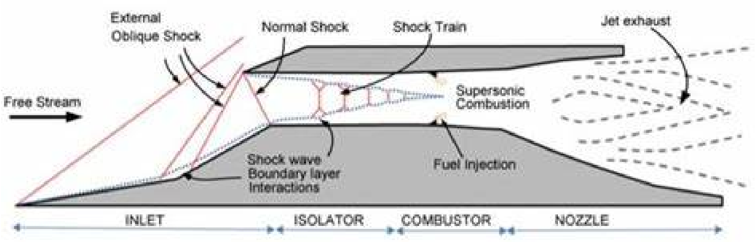

Figure B.3: Scramjet schematic diagram [44]

Estimating the performance of a scramjet is highly complex. In this case, for simplicity, a treatment in terms of Kinetic Energy Efficiency is used. This approach is based on the assumption that each major component of the engine functions according to its capacity to handle the working fluid. It is assumed that the working fluid behaves as a calorically perfect gas with consistent constants across the entire engine. Di conseguenza, the kinetic energy efficiencies of the engine's inlet, combustor, and nozzle are represented respectively as $\eta_{KE,c}$, $\eta_{KE,b}$, and $\eta_{KE,e}$. The total kinetic energy efficiency of the scramjet is equal to

$$\eta_{\mathrm{KEO}} = \eta_{\mathrm{KE,c}} \cdot \eta_{\mathrm{KE,b}} \cdot \eta_{\mathrm{KE,e}}. \tag{B.23}$$

According to [34], the overall kinetic energy efficiency of the air-breathing engine is assumed to fall within the range of $0.65 < \eta_{\mathrm{KEO}} < 0.75$. Thus, the specific thrust of a scramjet engine is given by:

$$\frac{F}{\dot{m}} = M_0\sqrt{\gamma R T_0}\left\{\sqrt{\eta_{\mathrm{KEO}}\ (1+f)\left[1+\frac{\eta_b\ f\ h_{pr}}{c_p T_0\left(1+((\gamma-1)/2)M_0^2\right)}\right]}-1\right\} \tag{B.24}$$

and:

$$I_{sp} = \frac{F}{g f \dot{m}} \tag{B.25}$$

where h_{pr} indicates the lower heating value (or lower calorific value) of the fuel.

Rocket Mode

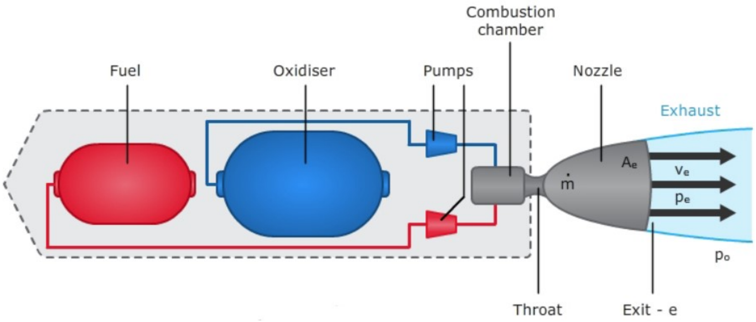

Figure B.4: Simple rocket propulsion system

The rocket performance calculation begins with the definition of thecharacteristic velocity c^*, assuming complete combustion, is calculated as

$$c^* = \frac{\sqrt{RT_c}}{\Gamma} \tag{B.26}$$

where Γ is the corrected mass flow rate for $M = 1$, $R = 8314.5/\mathcal{M}$, where $\mathcal{M}$ is the molar mass of the propellant mixture, and T_c is the temperature in the combustion chamber.

The geometry of the nozzle is evaluated. In the case of a critical nozzle, the mass flow rate at the throat is equated to the mass flow rate at the exit, $\dot{m}_t = \dot{m}_e$.

$$\frac{p_c A_t}{\sqrt{RT_c}} \cdot \Gamma = \frac{p_c A_e}{\sqrt{RT_c}} \sqrt{\frac{2\gamma}{\gamma - 1} \left[\left(\frac{p_e}{p_c} \right)^{\frac{2}{\gamma}} - \left(\frac{p_e}{p_c} \right)^{\frac{\gamma+1}{\gamma}} \right]} \tag{B.27}$$

where p_c is the pressure in the combustion chamber. Assuming the expansion ratio $\epsilon = \frac{A_e}{A_t}$, $\frac{p_e}{p_c}$ is calculated iteratively. The thrust coefficient c_F is obtained

$$c_F = \frac{\dot{\mathrm{m}}_e w_e + A_e \left(p_e - p_0 \right)}{p_c A_t} = \Gamma \sqrt{\frac{2\gamma}{\gamma - 1} \left[1 - \left(\frac{p_e}{p_c} \right)^{\frac{\gamma-1}{\gamma}} \right]} + \varepsilon \left(\frac{p_e}{p_c} - \frac{p_0}{p_c} \right) \tag{B.28}$$

At this point, the specific impulse and the thrust are respectively obtained as

$$I_{sp} = \frac{c^* c_F}{g_0} \tag{B.29}$$

$$F = A_t p_c c_F \tag{B.30}$$

with A_t being the throat area.

Ejector Mode

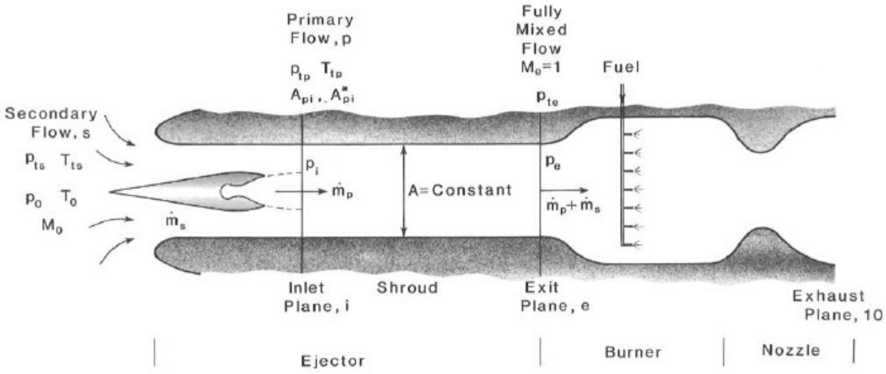

Figure B.5: ERJ schematic diagram for ideal analysis [34]

The performance of the ejector is provided through equations that need to be solved iteratively, with the inlet plane static pressure used as the iteration variable.

$$\left(\frac{2}{\gamma+1}\right)^{\frac{\gamma}{\gamma+1}} < \frac{p_i}{p_0} < \frac{p_{ts}}{p_0} \tag{B.31}$$

During the ideal ejector ramjet analysis, the mass flow of the fuel consumed is not considered. Thus, the performance measures of the ejector ramjet are computed. The thrust augmentation ratio is defined as

$$\phi_p = (1+\alpha)\frac{V_{10}}{V_{p0}} - \alpha\frac{V_0}{V_{p0}} \tag{B.32}$$

and the specific impulse

$$I_{sp_p} = \frac{a_0 M_0}{g_0}\phi_p\frac{V_{p0}}{V_0} \tag{B.33}$$

where α is the ratio between secondary and primary mass flows.

$$\alpha = \frac{p_{ts}}{p_0}\cdot\frac{p_0}{p_{tp}}\cdot\frac{A_{si}}{A}\cdot\frac{A}{A_{pi}}\cdot\frac{M_{si}}{M_{pi}}\sqrt{\frac{T_{tp}}{T_0}\cdot\frac{T_0}{T_{ts}}}\left\{\frac{1+\frac{\gamma-1}{2}M_{pi}^2}{1+\frac{\gamma-1}{2}M_{si}^2}\right\}^{\frac{\gamma+1}{2(\gamma-1)}} \tag{B.34}$$

Appendix C

MATLAB Code

C.1 SSTO HTOL Sizing Code

```
    %% FINAL TOOL

clear all
clc

%% User Inputs
Wpay = 15000;
rho_pay = 50;
Ncrw = 0;
ICI = 37.7;
h_targetorbit = 100000;
Mtr = 5;
htr = 28500; %m
% Engine selection. Please digit 1 for the selected
   engine and 0 for the others
SABRE = 1; % Database
turboramjet = 0; %Analytical Method for Turboramjet+
   Rocket

%% Assumptions
% Atmosphere ISA
            h = 0:100:51000; % m
            R = 287.05;
            [T, a, p, rho] = atmosisa(h,extended=true);
```

```matlab

% Propellant LOX/LH2
rho_f = 70.52/1000; %70.52/1000; %LH2 [ton/m^3]
hpr = 119954; % heat of reaction, H2 [kJ/kg]
rho_ox = 1141/1000; %LOX [ton/m^3]
MR = 6; % mixure ratio %6

% Value from statistics for the input payload to LEO orbit
GTOW_stat = (15.677775549*(Wpay/1000)^1.1229186457)*1000; %Kg
GTOW = GTOW_stat;
Wdry_stat = (0.867751184852*(GTOW_stat/1000)^0.75533773897032)*1000; %Kg
Spln_stat = 1.640205138*(GTOW_stat/1000) -88.1486838; %m^2;
T_to_stat = 1.158721737*10^-6*(GTOW_stat/1000)^3 - 0.001988945288194*(GTOW_stat/1000)^2 + 7.478778432789740*(GTOW_stat/1000) + 56.7545873127545; %kN
%T_vacuum_stat = 23.8854941423234*(GTOW_stat/1000)^0.837718399300137; %kN;
T_vacuum_stat = 10.943743815826*(GTOW_stat/1000) + 37.5226918895443; %kN
T_ramjet_stat = (5.582098252913430*GTOW_stat + 7382.6467029)/1000; %kN
TWO = T_to_stat*1000/(GTOW_stat*9.81); % Take off Thrust-Weight
TvWO = T_vacuum_stat*1000/(GTOW_stat*9.81); % T vacuum / GTOW
TrWO = T_ramjet_stat*1000/(GTOW_stat*9.81); % T high speed / GTOW
WR_stat = GTOW_stat/Wdry_stat;


%% Mission Analysis

g = 9.81;
gamma = 1.35; %adiabatic index

% Airbreathing ascent phase
```

```
% equations from Billing, "Design and Development of SSTO Vehicles"
V(1) = 500*0.305; %Take-off Velocity [m/s]
V(2:74) = sqrt(h(2:1:74)/(0.305*2.035*10^-2) + (V(1)/0.305)^2)*0.305; % [m/s]
q = 0.5*rho(htr/100)*(Mtr*a(htr/100))^2; % constant dynamic pressure [Pa]
V(200) =  sqrt(2*q./rho(200));
x = [h(1) h(74) h(200)]; y = [V(1) V(74) V(200)];
V(75:199) = spline(x,y,h(75:199));
V(200:length(h)) = sqrt(2*q./rho(200:511));
q = 0.5*rho.*V.^2;
M_h = V./a;
if SABRE == 1
M = M_h(M_h<5);
h = h(1:length(M));
V = V(1:length(M)); rho = rho(1:length(M)); hmax_ab = length(M);
Mturb = M(M<2.2); h_turb = length(Mturb); Msub = M(M<1); h_subc = length(Msub);
theta0 = 1+((gamma-1)/2)*M.^2;
end
if turboramjet == 1
    M = M_h;
    theta0 = 1+((gamma-1)/2)*M.^2;
end

%% Aerodynamics from database

CopiadiCD = importfile3("C:\Users\Tommaso\Downloads\Copia di CD.xlsx", "Foglio1", [1, Inf]);
CopiadiCL = importfile4("C:\Users\Tommaso\Downloads\Copia di CL.xlsx", "Foglio1", [1, Inf]);
for i = 1:1:height(CopiadiCD)
    cL(i) = CopiadiCL(i,3);
    cD(i) = CopiadiCD(i,3);
    LD(i) = cL(i)/cD(i);
    M_data(i) = CopiadiCD(i,1);
    alpha_data(i) = CopiadiCD(i,2);
end
j = 0;
```

```
for i = 3:8:83
    j = j+1;
    Cl(j) = cL(i);
    Cd(j) = cD(i);
    M_skylon(j) = M_data(i);
end

[fitresult_cd, gof_cd] = createFit(M_skylon, Cd);
[fitresult_cl, gof_cl] = createFit(M_skylon, Cl);
Cd = fitresult_cd(M)';
Cl = fitresult_cl(M)';
% [fitresult_a, gof_a] = createFit(M_skylon, alpha);
% alpha = fitresult_a(M(M<=17))';
L_D = Cl./Cd;

if turboramjet == 1
%% Propulsion
% Turbojet
cp = gamma*R/(gamma-1)/1000;
Tt4_turb = 1550; % T total inlet turbine, hypothetical value
thetaT = Tt4_turb./T;
pi_c = 10; % compression ratio compressor, hypothetical value
tau_c = pi_c^((gamma-1)/gamma);
f_turb = 0.0291; % stoichiometric;
%f_turb = cp*T.*(thetaT-tau_c*theta0)/hpr;

Specific_Thrust_turb = sqrt((2*theta0/(gamma-1)).*(thetaT./(theta0*tau_c)-1)*(tau_c-1) + thetaT.*M.^2./(theta0*tau_c)) - M;
Isp_turb = Specific_Thrust_turb.*a./(g*f_turb);
SFC_turb = 1./(g*Isp_turb);

% Ramjet
Tt4_ram = 1650; % T total exit combustor, hypotetical value
tau_max = Tt4_ram./T;
tau_b = tau_max./theta0;
f = 0.0291; % stoichiometric;

```

```
Specific_Thrust_ram = M.*(sqrt(tau_b)-1);
Isp_ram = Specific_Thrust_ram.*a./(g*f);
SFC_ram = 1./(g*Isp_ram);

% Scramjet
% energetic formulation from Heiser & Pratt, "Hypersonic
    airbreathing propulsion"
nke = 0.75;
eta_b = 0.9;
Isp_scram = (1./(g*f)).*a.*M.*(sqrt(nke*(1+f).*(1+(eta_b
   *f*hpr./(cp*T.*theta0))))-1);
SFC_scram = 1./(g*Isp_ram);

% Rocket
eps = 40; %area ratio
Tc = 3550; pc = 70;
Mmol = 12; yr = 1.21; %LOX/LH2
Rr = 8314.5/Mmol;
RHO = sqrt(yr)*(2/(yr+1))^((yr+1)/(2*(yr-1)));
c_star = sqrt(Rr*Tc)/RHO;
pe_pc_test = 0.3; tollpe_pc = 0.01;
while 1
pe_pc = (((RHO/eps)^2*(yr-1)/(2*yr))/(1-pe_pc_test^((yr
   -1)/yr)))^(yr/2);
if abs(pe_pc - pe_pc_test) < tollpe_pc
    break
else
    pe_pc_test = pe_pc_test-0.01;
end
if pe_pc_test < 0
    break
end
end
p_bar = p/(1*10^5);
pe = pe_pc*pc;
cf = RHO*sqrt((2*yr/(yr-1))*(1 - (pe/pc)^((yr-1)/yr))) +
    eps*(pe/pc - p_bar/pc);
Isp_rocket = c_star*cf/g;

% OVERALL
```

```
% NB: Hypotetical Mach and altitude for transitions, i'
    ll insert analytical methods
for i = 1:1:length(h)
if Isp_turb(i) > Isp_ram(i)
   Isp(i) = Isp_turb(i);
   Mtr_turboram = M(i);
   h_turb = i;
end
if turboramjet == 1
    if Isp_ram(i) > Isp_turb(i) && M(i) <= 5
    Isp(i) = Isp_ram(i);
    hmax_ab = i;
    end
    if M(i) > 5
    Isp(i) = Isp_rocket(i);
    end
end
end

if turboramjet == 1
M = M(M<=5);
end
V = V(1:length(M)); rho = rho(1:length(M)); T = T(1:
   length(M)); a = a(1:length(M)); h_subc = length(M(M
   <1));
end

%% ITERATION
N_engine = 1;
if turboramjet == 1
    N_engine = 2;
end
while 1
z = 1; % loop control parameter
zz = 0;
tau = 0.25; % First iterative variable
while 1
    Kw = - 93.831*tau.^3 + 59.920*tau.^2 - 5.648*tau +
   2.821; %wing body

    %L_D estimation from Curran Model
```

```
    F = (tau^0.333)*(Kw^0.75);
    A = 3; B = 2; %empirical coefficient
    L_D_est = A*((M+B)./M)*(1.11238 - 0.1866*F);

%% SABRE
if SABRE == 1
M_isp = [0.00778267917923067
0.0719042052302153
0.168092952961613
0.360463989769488
0.428163610646444
0.535002680341789
0.737965911219327
0.830531353540309
0.905303201555242
1.14017864639510
1.23266658485703
1.33227196104139
1.54575634078447
1.64540046889835
1.73079680425754
1.96920513333893
2.12944436191719
2.36443606254561
2.42853821263184
2.52823400998508
2.73832113723996
2.81311881987457
2.91279524126305
3.13713661992753
3.22615626069715
3.31162364126047
3.53236109047930
3.61784138835246
3.69973713274473
3.92405913544445
4.00956526793730
4.07365450071368
4.29080739645161
4.37980120260155
4.47591244647390
```

```
4.71086539517280
4.78917012742926
4.88528782995653
4.99919266813493]';

Isp = [26333.9382940109
25970.9618874773
25390.1996370236
24264.9727767695
23793.1034482758
23357.5317604356
22704.1742286751
22486.3883847550
22268.6025408348
22268.6025408348
22486.3883847550
22704.1742286751
22921.9600725953
22921.9600725953
22994.5553539020
23139.7459165154
22595.2813067150
21941.9237749546
21687.8402903811
21397.4591651542
20707.8039927405
20344.8275862069
20163.3393829401
19364.7912885662
19074.4101633394
18747.7313974591
18203.2667876588
17803.9927404718
17549.9092558983
16860.2540834846
16315.7894736842
16134.3012704174
15735.0272232305
15589.8366606170
15444.6460980036
15009.0744101633
```

```
14936.4791288566
14754.9909255898
14609.8003629764]'/9.81;

[fitresult_isp, gof_isp] = createFit3(M_isp, Isp);
Isp = fitresult_isp(M)';

M_thrust =[0.00342416434331318
0.109956599623499
0.184513763482972
0.397570863625016
0.500549627589753
0.564539022522818
0.784944348263935
0.880955637127682
0.980466204378580
1.20425425223193
1.29659531350530
1.37472945993521
1.60207117910400
1.68023640720722
1.77615445105103
2.01064236494236
2.08178572501629
2.16712822951537
2.40181040386490
2.47295376393884
2.56184216933503
2.78233296967776
2.86056036112760
2.95301797867590
3.14507940849504
3.23399112514622
3.34067896879297
3.52920226813331
3.63232089962795
3.73189363022548
3.92753204261505
4.01642821842957
4.11245504812997
4.34003765026694
```

```
4.42536461392936
4.51781446105933
4.74539706319630
4.80940199896602
4.90542105824810
5.00138572460187]';

Fu = N_engine*8*[153207.007052432
155384.278268005
157345.687262420
161918.889265323
164096.471297629
163434.897881163
161229.031526141
159471.362900293
159244.000460009
161848.333866902
163370.869634138
164675.989096549
167280.011686709
167710.492862094
168576.739097326
170086.842195237
168112.689714764
166574.613110872
162618.226914864
160644.074434392
159324.346585523
154713.224941178
153394.429542509
151637.071733394
147028.436622914
145052.730058776
142856.809839215
137811.166401955
136052.876142640
134076.237128302
128811.312485819
127272.925065194
125077.937295833
120903.513161535
```

```
119802.755701156
118264.057463798
114089.633329500
112990.740769520
111014.412571916
110568.701376608]';

[fitresult_thrust, gof_thrust] = createFit3(M_thrust, Fu
    );
Fu = fitresult_thrust(M)';


%% Rocket Mode

eps = 40; %area ratio
Tc = 3550; pc = 70;
Mmol = 12; yr = 1.21; %LOX/LH2
Rr = 8314.5/Mmol;
RHO = sqrt(yr)*(2/(yr+1))^((yr+1)/(2*(yr-1)));
c_star = sqrt(Rr*Tc)/RHO;
pe_pc_test = 0.3; tollpe_pc = 0.01;
while 1
pe_pc = (((RHO/eps)^2*(yr-1)/(2*yr))/(1-pe_pc_test^((yr
    -1)/yr)))^(yr/2);
if abs(pe_pc - pe_pc_test) < tollpe_pc
    break
else
    pe_pc_test = pe_pc_test-0.01;
end
if pe_pc_test < 0
    break
end
end
p_bar = p/(1*10^5);
pe = pe_pc*pc;
cf = RHO*sqrt((2*yr/(yr-1))*(1 - (pe/pc)^((yr-1)/yr))) +
    eps*(pe/pc - p_bar/pc);
Isp_rocket = c_star*cf(length(cf))/g;
At = 0.154;
Thrust_r = cf*At*pc*10^5;
Fu_rocket = Thrust_r(hmax_ab)*N_engine;
```

```
end

%% WR weight ratio

WRprova = exp((V(hmax_ab))/(g*(Isp(1)+Isp(hmax_ab))/2));
WR_to = 1.01; % statistical value
% Turbo climb
deltah = 100; % segment of climb [m]
flightpath_angle_sub = 8*pi/180; %hypotetical value
j = 1;
for i = 2:1:h_turb
    Vm = (V(i)+V(i-1))/2;
    Ispm = (Isp(i)+Isp(i-1))/2;
    L_Dm = (L_D(i) + L_D(i-1))/2;
    WR_climb_sub(j) = exp(deltah/(Vm*sin(
   flightpath_angle_sub)*Ispm*L_Dm));
    j = j+1;
end
WR_turbo = prod(WR_climb_sub);

% Subsonic cruise, buffer
R_sub = 0; % [m]
V_cruise_sub = V(h_subc); Isp_cruise_sub = Isp(h_subc);
   L_D_cruise_sub = L_D(h_subc);
WR_cruise_sub = exp(R_sub/(V_cruise_sub*Isp_cruise_sub*
   L_D_cruise_sub));

% Turboram climb
flightpath_angle_super = 3*pi/180; % Hypothetical value
j = 1;
for i = h_turb+1:1:hmax_ab
    Vm = (V(i)+V(i-1))/2;
    Ispm = (Isp(i)+Isp(i-1))/2;
    L_Dm = (L_D(i) + L_D(i-1))/2;
    WR_climb_super(j) = exp(deltah/(Vm*sin(
   flightpath_angle_super)*Ispm*L_Dm));
    j = j+1;
end
WR_super = prod(WR_climb_super);

% Total Airbreathing Weight ratio
```

```
WR_ab = WR_to*prod(WR_climb_sub)*prod(WR_climb_super)*WR_cruise_sub;
% Rocket climb
mu = 3.986*10^5;
r0 = 6371+hmax_ab/10;
r1 = h_targetorbit/1000+r0-hmax_ab/10;
r2 = 400+r0-hmax_ab/10;
a_hohmann1 = (r1+r0)/2;
E_hohmann1 = - mu/(2*a_hohmann1);
V0 = sqrt(2*(E_hohmann1 + mu/r0));
V1_1 = sqrt(2*(E_hohmann1 + mu/r1));
a_hohmann2 = (r1+r2)/2;
E_hohmann2 = - mu/(2*a_hohmann2);
V1_2 = sqrt(2*(E_hohmann2 + mu/r1));
deltaVtot = V0 - V(hmax_ab)/1000; % + (V1_2 - V1_1);
deltaVp = 0.05*deltaVtot;
deltaVtot_rocket = deltaVtot + deltaVp;
if SABRE == 1
Isp_rocket_m = Isp_rocket;
end
if turboramjet == 1
    Isp_rocket_m = (Isp(hmax_ab+1)+Isp(length(h)))/2;
end
WR_r = exp(deltaVtot_rocket*1000/(g*Isp_rocket_m));

% Total Weight Ratio
WR = WR_ab*WR_r;

o_f = (6/7)*(1/WR_ab - (1/WR_ab)/WR_r)/((1-1/WR_ab) + (1/WR_ab - (1/WR_ab)/WR_r)/7);
rho_ppl = rho_f*(1+o_f)/(1+(rho_f/rho_ox)*o_f);
Istr = 10*(rho_ppl*1000/(WR-1))/ICI;

k = 0;
Spln = 1; %[m^2]
while 1
while 1

%% Weight Budget
% typical values from Czysz, "Chapter 16, Transatmospheric Launcher Sizing"
```

```
fcprv = 0.45; %0.45:0.01:0.5; %ton/person
Wcprv = fcprv*Ncrw; %ton
Cun = 1.9; % 1.9:0.1:2.1; %ton
fmnd = 1.05; %1.05:0.05:1.45; %ton/person
Csys = Cun + fmnd*Ncrw;
Wcrw = 0.14*Ncrw;
X = 0.697; %0.63:0.01:0.71; % (1/(1+mu) - fsys)
fsys = 0.2;
mu = 1/(X+fsys) -1;
ETW = (-36.25*X + 30.537)*TW0*WR; % suggested relation
   with X from Czysz, "Chapter 16, Transatmospheric
   Launcher Sizing"
%ETW = circa 19.8; % SABRE, data from REL
% NB: the ETW value is for the general airbreathing
   propulsion system and depends on thrust-weight at
   take off, i haven't found yet pratical sizing
   equation for specific configutations like ATR engine
   or dual mode ram-scram engine.
Wdry1 = (Istr*Kw*Spln/1000 + Wcprv + Csys + (TW0*WR/ETW)
   *(Wpay/1000+Wcrw))/(X-TW0*WR/ETW);

%% Volume Budget
% typical values from Czysz, "Chapter 16,
   Transatmospheric Launcher Sizing"
kvs = 0.02; % 0.02:0.01:0.04;
Vun = 5; %5:1:7; %m^3
fcrw = 11; %11:1:12; %m^3/person
kve = 0.25; %0.25:0.05:0.75; %m^3/ton thrust
kvv = 0.1; %0.1:0.1:0.2;
kcprv = 5; %5:0.5:6; %m^3/person
kcrew = 0.9; %0.9:0.1:2; %m^3/person

Wdry2 = (tau*Spln^1.5*(1-kvv-kvs) - (kcprv+kcrew)*Ncrw -
    Wpay/rho_pay - Vun - fcrw*Ncrw)/((WR-1)/rho_ppl +
   kve*TW0*WR) - Wpay/1000 - 0.14*Ncrw;

%% Iteration
toll = 0.2;
if abs(Wdry1 - Wdry2) < toll
    GTOW = (Wdry1+Wpay/1000+0.14*Ncrw)*WR*1000;
    break
```

```
end
    Spln = Spln +1;
    k = k+1;
if k > 2000 % loop control parameter
    break
end
end
if SABRE == 1
if abs(TWO - Fu(1)/(GTOW*9.81)) < 0.001
    break
end
TWO = Fu(1)/(GTOW*9.81);
end
if turboramjet == 1
    break
end
end

%% DATA

W_TOT(z) = GTOW;
Wdry_TOT(z) = Wdry1;
GTOW_Spln = GTOW/Spln;
Swet = Kw*Spln;
Vol_tot = tau*Spln^1.5;
Wdry = Wdry1*1000;
WLH2 = ((1-1/WR_ab) + (1/WR_ab - (1/WR_ab)/WR_r)/7)*GTOW
   ;
WLOX = (6/7)*(1/WR_ab - (1/WR_ab)/WR_r)*GTOW;
Wprop = WLH2+WLOX;
Wprop_TOT(z) =  Wprop;
Wstr_TOT = Istr*Kw*Spln;
Wengine = TWO(1)*WR*(Wdry+Wpay)/ETW;
Wsubsys = fsys*Wdry;

Vpay = Wpay/rho_pay;
Vempty = kvv*Vol_tot;
Vsubsys = Vun + kvs*Vol_tot;
Vengines = kve*TWO(1)*WR*(Wdry+Wpay)/1000;
Vprop = Wprop/(rho_ppl*1000);
VLOX = WLOX/(rho_ox*1000);
```

```
VLH2 = WLH2/(rho_f*1000);

%% Matching Chart
W_S = 100:1:1.5*10^3; % range of values
T_W = 0:0.1:5;

% Take off
l_to = 4000;
s_to = 3.2808*l_to;
TOP_25 = s_to/37.5;
TOP_25 = TOP_25*4.8824;
rho_to = 1.225;
Cl_to = 0.687;
sigma_to = rho_to./rho(1);
T_W_to = (W_S)/(sigma_to*TOP_25*Cl_to);

% Second segment requirement
E_2nd = Cl(1)/Cd(1);
if N_engine == 1
G_2nd = 0.024;
end
if N_engine ==2
G_2nd = 0.024;
end
if N_engine == 3
G_2nd = 0.027;
end
if N_engine == 4
G_2nd = 0.03;
end
T_W_2snd = N_engine/(N_engine-1)*(1/E_2nd + G_2nd)*(1/
    sigma_to)*ones(1,length(W_S));

% Subsonic climb
th_subclimb = 1; G_subclimb = tan(flightpath_angle_sub);
sigma_subclimb = (sigma_to + rho(h_turb)/rho(1))/2;
Cd_subclimb = (Cd(1)+Cd(h_turb))/2;
q_subclimb = (0.5*rho(1)*V(1)^2 + 0.5*rho(h_turb)*V(
    h_turb)^2)/2;
T_W_subclimb = (q_subclimb*Cd_subclimb./(g*W_S) +
    G_subclimb)*(1/(th_subclimb*sigma_subclimb));
```

```matlab

% Subsonic cruise (best range)
th_subcruise = 1;
sigma_subcruise = rho(h_subc)/rho(1);
q_subcruise = 0.5*rho(h_subc)*V(h_subc)^2;
Cd_subcruise = Cd(h_subc);
T_W_subcruise = (q_subcruise*Cd(h_subc)./(g*W_S))*(1/(
    th_subcruise*sigma_subcruise));

% Supersonic climb
th_superclimb = 1;
sigma_superclimb = (rho(h_turb) + rho(hmax_ab))/(2*rho
    (1));
q_superclimb = (0.5*rho(h_turb)*V(h_turb)^2 + 0.5*rho(
    hmax_ab)*V(hmax_ab)^2)/2;
Cd_superclimb = (Cd(h_turb)+Cd(hmax_ab))/2;
G_superclimb = tan(flightpath_angle_super);
T_W_superclimb = (q_superclimb*Cd_superclimb./(g*W_S) +
    G_superclimb)*(1/(th_superclimb*sigma_superclimb));

% Landing
s_LFL = 1900;
s_ALD = s_LFL/1.6;
kapp = 1.7;
Vapp = sqrt(s_ALD*kapp^2);
rho_l = 1.225;
sigma_l = rho_l/rho(1);
Cl_a = 0.864;
W_S_land = rho(1)*sigma_l*Cl_a*Vapp^2/(2*g);
W_S_land_to = W_S_land*WR*ones(1,length(T_W));

%% Supersonic Matching Chart

% Supersonic climb
sigma_superclimb_SUP = (rho(h_turb)+rho(hmax_ab))/(2*rho
    (h_turb));
T_W_superclimb_SUP = (q_superclimb*Cd_superclimb./(g*W_S
    ) + G_superclimb)*(1/(th_superclimb*
    sigma_superclimb_SUP));

% Supersonic cruise
```

```
sigma_supercruise_SUP = rho(hmax_ab)/rho(h_turb);
th_supercruise = 1;
q_supercruise = 0.5*rho(hmax_ab)*V(hmax_ab)^2;
T_W_supercruise_SUP = (q_supercruise*Cd(hmax_ab)./(g*W_S
   ))*(1/(th_supercruise*sigma_supercruise_SUP));

WSUP = GTOW/(WR_to*prod(WR_climb_sub)*WR_cruise_sub);
ROC_ram = (V(h_turb)+V(hmax_ab))/2*sin(
   flightpath_angle_super);
deltaV_ram = V(hmax_ab) - V(h_turb);
h_ram = hmax_ab-h_turb;
Mmax_ram = M(hmax_ab);
% Access to space
[T_W_access_ram] = orbitReachingReq4(tau,WSUP,Wpay,
   Mmax_ram,h_ram*100,ROC_ram,Istr,rho_pay,deltaV_ram);
T_W_access_ram = T_W_access_ram(W_S);

% Identification of design point
WSUP = GTOW/(WR_to*prod(WR_climb_sub)*WR_cruise_sub);
W_S_Design_SUP = (W_S_land_to(1))*WSUP/GTOW;

% Max design point considering Subsonic W/S

% Supersonic Climb
T_W_superclimb_Design_SUPGEN = (q_superclimb*
   Cd_superclimb./(g*W_S_land_to(1)*WSUP/GTOW) +
   G_superclimb)*(1/(th_superclimb*sigma_superclimb_SUP)
   );

% Supersonic Cruise
T_W_supercruise_Design_SUPGEN = (q_supercruise*Cd(
   hmax_ab)./(g*W_S_land_to(1)*WSUP/GTOW))*(1/(
   th_supercruise*sigma_supercruise_SUP));

T_W_Design_MAX_SUPGEN(1) = T_W_superclimb_Design_SUPGEN;
T_W_Design_MAX_SUPGEN(2) = T_W_supercruise_Design_SUPGEN
   ;
T_W_Design_MAX_TOTAL_SUPGEN = max(T_W_Design_MAX_SUPGEN)
   ;


```

```
%% Subsonic Matching Chart

ROC_turb = V(h_turb)/2*sin(flightpath_angle_sub);
deltaV_turb = V(h_turb);
Mmax_turb = M(h_turb);
% Access to space
[T_W_access_turb] = orbitReachingReq4(tau,GTOW,Wpay,
    Mmax_turb,h_turb*100,ROC_turb,Istr,rho_pay,
    deltaV_turb);
T_W_access_turb = T_W_access_turb(W_S);

W_S_Design = W_S_land_to(1);

% Take-off
T_W_to_Design = (W_S_Design)/(sigma_to*TOP_25*Cl_to);

% Second Segment
T_W_2snd_Design = N_engine/(N_engine-1)*(1/E_2nd + G_2nd
    )*(1/sigma_to);

% Subsonic Climb
T_W_subclimb_Design = (q_subclimb*Cd_subclimb./(g*
    W_S_Design) + G_subclimb)*(1/(th_subclimb*
    sigma_subclimb));

% Subsonic Cruise
T_W_subcruise_Design = (q_subcruise*Cd(h_subc)./(g*
    W_S_Design))*(1/(th_subcruise*sigma_subcruise));

% Max design point (SUB)
T_W_Design_MAX_SUB(1) = T_W_to_Design;
T_W_Design_MAX_SUB(2) = T_W_2snd_Design;
T_W_Design_MAX_SUB(3) = T_W_subclimb_Design;
T_W_Design_MAX_SUB(4) = T_W_subcruise_Design;
T_W_Design_MAX_TOTAL_SUB = max(T_W_Design_MAX_SUB);

%% Rocket Mode Matching Chart
Wmax_ab = GTOW/WR_ab;
ROC_r = 125;
h_orbit = 1000;
h_rocket = h_orbit - hmax_ab;
```

```
[T_W_access_rock] = orbitReachingReq5(tau,Wmax_ab,Wpay,
   WR_r,h_rocket*100,ROC_r,Istr,rho_pay,deltaVtot_rocket
   *1000);

W_S_Design_ROCK = (W_S_land_to(1))*Wmax_ab/GTOW;
T_W_Design_ROCK = T_W_access_rock(W_S_Design_ROCK);
T_W_access_rock = T_W_access_rock(W_S);

%% Iteration
if GTOW_Spln < W_S_Design && Spln ~= 2002
    break
end
    tau = tau - 0.001;
    z = z+1;
    zz = zz+1;
if z > 150 % loop control parameter
    break
end
end
Wmax_ab = GTOW/WR_ab;
if SABRE == 1
TWsup = (Fu(h_turb)+Fu(hmax_ab))/(2*9.81*WSUP);
TWrock = Fu_rocket/(9.81*Wmax_ab);
end
if turboramjet == 1
    TWsup = TrW0*GTOW/WSUP;
    TWrock = TvW0*GTOW/Wmax_ab;
end
if TW0 >= T_W_Design_MAX_TOTAL_SUB
    if TWsup >= T_W_Design_MAX_TOTAL_SUPGEN
        if TWrock >= T_W_Design_ROCK
    break
        end
    end
end
if SABRE == 1
 N_engine = N_engine +1;
end
 if turboramjet == 1
 TrW0 = TrW0*(TW0+0.01)/TW0;
 TvW0 = TvW0+0.01;
```

```
 TW0 = TW0+0.01;
 end
 zz = 1;
end
W_TOT = W_TOT(1:zz); Wprop_TOT = Wprop_TOT(1:zz); Wdry_TOT = Wdry_TOT(1:zz);
TW0 = TW0*ones(1,length(W_S));
TWsup = TWsup*ones(1,length(W_S));
TWrock = TWrock*ones(1,length(W_S));

%% TPS sizing

L_D_re = 1.5; cD_re = 0.5; R = 0.1; phi = 70*pi/180;
[Q, qw, v_vc0, Tw, h_re, delta_t_tot, Mach, x, Istr_TPS] = function_TPS(Wdry1*1000, Spln,L_D_re, cD_re, R, phi);
WTPS = Istr_TPS*Swet;
Wstr = Wstr_TOT-WTPS;

%% PLOT

figure(2)
hold on
axis([0 1500 0 5])
xlabel('W/S [kg/m^2]')
ylabel('T/W')
title('Matching Chart - Turbo-ramjet mode')
plot(W_S,T_W_superclimb_SUP, 'blue','LineWidth',1.5)
plot(W_S,T_W_supercruise_SUP,'LineWidth',1.5)
plot(W_S_land_to*WSUP/GTOW,T_W, 'red','LineWidth',1.5)
plot(W_S,TWsup,'--','LineWidth',1.5)
plot(W_S,T_W_access_ram,'LineWidth',1.5)
plot(W_S_Design_SUP, T_W_Design_MAX_TOTAL_SUPGEN, 'ro','MarkerSize', 10, 'MarkerFaceColor','r')
legend('Climb req.','Cruise req.','Ref Surface','High-speed engine mode','Orbit reaching req.','Design point')

figure(1)
hold on
axis([0 1500 0 5])
```

```
xlabel('W/S [kg/m^2]')
ylabel('T/W')
title('Matching Chart - Turbojet mode')
plot(W_S,T_W_subclimb, 'blue','LineWidth',1.5)
plot(W_S,T_W_subcruise,'LineWidth',1.5)
plot(W_S_land_to,T_W, 'red','LineWidth',1.5)
plot(W_S,TW0,'--','LineWidth',1.5)
plot(W_S,T_W_access_turb,'LineWidth',1.5)
plot(W_S,T_W_2snd,'LineWidth',1.5)
plot(W_S,T_W_to,'LineWidth',1.5)
plot(W_S_Design, T_W_Design_MAX_TOTAL_SUB, 'ro', '
    MarkerSize', 10, 'MarkerFaceColor','r')
legend('Climb req.','Cruise req.','Ref. Surface','Low-
    speed engine mode','Orbit reaching req.','2-segment
    req.','Take-off req.','Design point')

figure(3)
hold on
axis([0 1500 T_W_Design_ROCK-0.02 T_W_Design_ROCK+0.02])
xlabel('W/S [kg/m^2]')
ylabel('T/W')
title('Matching Chart - Rocket mode')
plot(W_S,T_W_access_rock,'LineWidth',1.5,Color= '#77AC30
    ')
plot(W_S_land_to*Wmax_ab/GTOW,T_W, 'red','LineWidth'
    ,1.5)
plot(W_S,TWrock,'--','LineWidth',1.5,Color='#7E2F8E')
plot(W_S_Design_ROCK,T_W_Design_ROCK,'ro', 'MarkerSize',
     10, 'MarkerFaceColor','r')
legend('Orbit reaching req.','Ref. Surface','Engine
    rocket mode','Design point')

if SABRE == 1
figure(4)
hold on
xlabel('Mach')
ylabel('Altitude h [m]')
plot(M,h,'LineWidth',1.5)
end

if turboramjet == 1
```

```
figure(4)
hold on
xlabel('Mach')
ylabel('Altitude h [m]')
plot(M,h(1:hmax_ab),'LineWidth',1.5)
end

figure(5)
hold on
xlabel('x [m]')
ylabel('Q [J/m^2]')
plot(x(2:length(x)),Q(2:length(Q)),'-o','LineWidth',1.5)

figure(6)
for i = 1:12:length(h_re)
    hold on
    ylim([0 110000])
    xlim([0 85])
    xlabel('x [m]')
    ylabel('qw [W/m^2]')
    plot(x(2:length(x)),qw(i,(2:length(x))),'LineWidth'
   ,1.5)
end
legend('Mach 27','Mach 19.5','Mach 10.5','Mach 5','Mach
    2.5','Mach 1', 'Mach 0.4')

figure(7)
for i = 1:12:length(h_re)
    hold on
    ylim([200 1300])
    xlim([0 85])
    xlabel('x [m]')
    ylabel('Tw [K]')
    plot(x(2:length(x)),Tw(i,(2:length(x))),'LineWidth'
   ,1.5)
end
legend('Mach 27','Mach 19.5','Mach 10.5','Mach 5','Mach
    2.5','Mach 1', 'Mach 0.4')

figure(8)
hold on
```

```
xlabel('Mach')
ylabel('Tw stagnation point [K]')
plot(Mach,Tw(:,(1))','-o','LineWidth',1.5)

figure(9)
hold on
xlabel('Mach')
ylabel('qw stagnation point [W/m^2]')
plot(Mach,qw(:,(1))','-o','LineWidth',1.5)

figure(10)
hold on
xlabel('Velocity Ratio')
ylabel('Altitude [m]')
plot(v_vc0,h_re,'LineWidth',1.5)

figure(11)
hold on
xlabel('Time from Entry [s]')
ylabel('Velocity Ratio')
plot(delta_t_tot,v_vc0,'LineWidth',1.5)

if SABRE == 1
figure(12)
hold on
xlabel('Flight Mach')
ylabel('L/D')
plot(M,L_D,'LineWidth',1.5)
plot(M,L_D_est,'LineWidth',1.5)
legend('L/D from CFD data', 'L/D from empirical method')
end
if turboramjet == 1
figure(12)
hold on
xlabel('Flight Mach')
ylabel('L/D')
plot(M,L_D(1:hmax_ab),'LineWidth',1.5)
plot(M,L_D_est,'LineWidth',1.5)
legend('L/D from CFD data', 'L/D from empirical method')
end

```

```
zz = 1:1:zz;
figure(13)
hold on
xlabel('N^ of iterations for the W/S consistence')
ylabel('GTOW')
plot(zz,W_TOT,'LineWidth',1.5)

figure(14)
hold on
xlabel('N^ of iterations for the W/S consistence')
ylabel('W propellant')
plot(zz,Wprop_TOT,'LineWidth',1.5,Color='#D95319')
```

C.2 Function: TPS sizing

```
    function [Q, qw, v_vc0, Tw, h_re, delta_t_tot, Mach,
     x, Istr_TPS] = function_TPS(W_dry, Spln,L_D_re,
   cD_re, R, phi)


x = 0:1:84;
beta = W_dry/(cD_re*Spln);
sigma = 5.670367*10^-8;
eps = 0.85;

g0 = 9.81; gamma = 1.35;
h_re = 84000:-1000:1;
[T, a, p, rho, nu] = atmosisa(h_re,extended=true);
nu_e = nu;
r0 = 6371000;
V = sqrt(g0*(r0+h_re)./(1+(rho.*(r0+h_re)*L_D_re)/(2*
   beta)));
Mach = V./a;
u_e = V;
T0 = T.*(1+(gamma-1)*0.5*Mach.^2);

z = 0; b = 0;
for i = 1:1:length(h_re)
```

```matlab
    for j = 1:1:length(x)
% transition above Rex = 3*10^6, fully turbolent achieved Rex = 7*10^6;
Rex(i,j) = u_e(i)*x(j)/nu_e(i); % edge boundary layer = free stream?
ReT(i) = 10^(6.421*exp(1.209*10^-4*Mach(i)^2.641));
k = 0;
Tw(i,j) = T(i);
while 1

xT = 0;
if Rex(i,j) == 0
%stagnation point
Ms = 3; Ns = 0.5; Cs(i) = (1.83*10^-8)*(R^-0.5)*(1-Tw(i,j)/T0(i));
qw(i,j) = rho(i)^Ns*V(i)^Ms*Cs(i)*10^4; %approx of eq 6.106
end

if Rex(i,j) < ReT(i) && Rex(i,j) ~= 0
% Laminar flat plate
M = 3.2; N = 0.5; C(i,j) = (2.53*10^-9)*cos(phi)^0.5*sin(phi)*(x(j)^-0.5)*(1-Tw(i,j)/T0(i));
qw(i,j) = rho(i)^N*V(i)^M*C(i,j)*10^4;
xT = Rex(i,j)*nu_e(i)/(u_e(i));
end

if Rex(i,j) >= ReT(i)
    if xT <= 1
        xT = 0;
    end
% Turbolent flat plate
if V < 3962
    Mt = 3.37;
    Ct(i,j) = (3.89*10^-8)*cos(phi)^1.78*sin(phi)^1.6*(x(j)-xT)^(-1/5)*(Tw(i,j)/556)^(-1/4)*(1-1.11*Tw(i,j)/T0(i));
else
    Mt = 3.7;
    Ct(i,j) = (2.2*10^-9)*cos(phi)^2.08*sin(phi)^1.6*(x(j)-xT)^(-1/5)*(1-1.11*Tw(i,j)/T0(i));
```

```
end
qw(i,j) = rho(i)^N*V(i)^Mt*Ct(i,j)*10^4;
end

% thermal energy radiated
qw_out(i,j) = sigma*eps*Tw(i,j)^4;

if abs(qw(i,j)-qw_out(i,j)) < 305
    break
end
Tw(i,j) = Tw(i,j) + 0.25;
k = k+1;
if k > 8001
    b = b+1;
    n(b) = i;
    break
end
end
    end
% flight time
v_vc0(i) = sqrt(1/(1+(rho(i)*r0*L_D_re)/(2*beta)));
t_tot(i) = 0.5*sqrt(r0/g0)*L_D_re*log((1+v_vc0(i)^2)
   /(1-(v_vc0(i))^2));
delta_t_tot(i) = t_tot(1) - t_tot(i);
if i > 1
    z = z+1;
    delta_t(z) = t_tot(i-1) - t_tot(i);
end
end

% heat load
qw_m = zeros(length(h_re)-1,length(x));
for j = 1:1:length(x)
    for i = 1:1:length(h_re)-1
       qw_m(i,j) = (qw(i,j) + qw(i+1,j))/2;
    end
end

for j = 1:1:length(x)
Q(j) = sum(qw_m(:,j)'.*delta_t);
end
```

```
Q_TPS = Q/(3.281^2*1055);

% Conversion Unit
% 1 [m] = 39.3701 [in]; 1 [J] = [Btu]/1055.056; 1 [m] =
    3.2808 [ft]; 1 [kg]=  2.2046 [lb];
% T(F) = ((T(K) - 273.15) * 1.8) + 32; T(K) = (T(F) +
    459,67) * 5/9;

Q_prova_HT = 3900:1:32000;
Q_prova_LW = 0:1:5500;

Q_prova_HT = 3900:1:32000;
Q_prova_LW = 0:1:5500;

TABI_highT = importdata("C:\Users\Tommaso\OneDrive\
    Documenti\MATLAB\TABI_highT.mat");
[fitresult1, gof1] = createFit3(TABI_highT(:,1)',
    TABI_highT(:,2)');
TABI_hT = fitresult1(Q_prova_HT)';
AETB12TUFI_highT = importdata("C:\Users\Tommaso\OneDrive
    \Documenti\MATLAB\AETB12TUFI_highT.mat");
[fitresult2, gof2] = createFit3(AETB12TUFI_highT(:,1)',
    AETB12TUFI_highT(:,2)');
AETB12TUFI_hT = fitresult2(Q_prova_HT)';
AMHC_highT = importdata("C:\Users\Tommaso\OneDrive\
    Documenti\MATLAB\AMHC_highT.mat");
[fitresult3, gof3] = createFit3(AMHC_highT(:,1)',
    AMHC_highT(:,2)');
AMHC_hT = fitresult3(Q_prova_HT)';
SAHC_highT = importdata("C:\Users\Tommaso\OneDrive\
    Documenti\MATLAB\SAHC_highT.mat");
[fitresult4, gof4] = createFit3(SAHC_highT(:,1)',
    SAHC_highT(:,2)');
SAHC_hT = fitresult4(Q_prova_HT)';
SAHC2_highT = importdata("C:\Users\Tommaso\OneDrive\
    Documenti\MATLAB\SAHC2_highT.mat");
[fitresult5, gof5] = createFit3(SAHC2_highT(:,1)',
    SAHC2_highT(:,2)');
SAHC2_hT = fitresult5(Q_prova_HT)';
LI900_highT = importdata("C:\Users\Tommaso\OneDrive\
    Documenti\MATLAB\LI900_highT.mat");
```

```
[fitresult6, gof6] = createFit3(LI900_highT(:,1)',
    LI900_highT(:,2)');
LI900_hT = fitresult6(Q_prova_HT)';
AETB8TUFI_highT = importdata("C:\Users\Tommaso\OneDrive\
    Documenti\MATLAB\AETB8TUFI_highT.mat");
[fitresult7, gof7] = createFit3(AETB8TUFI_highT(:,1)',
    AETB8TUFI_highT(:,2)');
AETB8TUFI_hT = fitresult7(Q_prova_HT)';


AFRSI_lowT = importdata("C:\Users\Tommaso\OneDrive\
    Documenti\MATLAB\AFRSI_lowT.mat");
[fitresult8, gof8] = createFit3(AFRSI_lowT(:,1)',
    AFRSI_lowT(:,2)');
AFRSI_lT = fitresult8(Q_prova_LW)';
TABI_lowT = importdata("C:\Users\Tommaso\OneDrive\
    Documenti\MATLAB\TABI_lowT.mat");
[fitresult9, gof9] = createFit3(TABI_lowT(:,1)',
    TABI_lowT(:,2)');
TABI_lT = fitresult9(Q_prova_LW)';
TIHC_lowT = importdata("C:\Users\Tommaso\OneDrive\
    Documenti\MATLAB\TIHC_lowT.mat");
[fitresult10, gof10] = createFit3(TIHC_lowT(:,1)',
    TIHC_lowT(:,2)');
TIHC_lT = fitresult10(Q_prova_LW)';
TIMW_lowT = importdata("C:\Users\Tommaso\OneDrive\
    Documenti\MATLAB\TIMW_lowT.mat");
[fitresult11, gof11] = createFit3(TIMW_lowT(:,1)',
    TIMW_lowT(:,2)');
TIMW_lT = fitresult11(Q_prova_LW)';
LI900_lowT = importdata("C:\Users\Tommaso\OneDrive\
    Documenti\MATLAB\LI900_lowT.mat");
[fitresult12, gof12] = createFit3(LI900_lowT(:,1)',
    LI900_lowT(:,2)');
LI900_lT = fitresult12(Q_prova_LW)';

Istr_tps = zeros*length(Q_TPS);
for j = 1:1:length(Q_TPS)
    i = 1;
    while abs(Q_prova_LW(i) - Q_TPS(j)) > 1
```

```
        Istr_tps(j) = min([LI900_lT(i), TIMW_lT(i),
   TIHC_lT(i), TABI_lT(i), AFRSI_lT(i)]);
        i = i+1;
        if i == length(Q_prova_LW)
            Istr_tps(j) = 0;
            break
        end
    end
end

for j = 1:1:length(Q_TPS)
    i = 1;
    if Istr_tps(j) == 0
    while abs(Q_prova_HT(i) - Q_TPS(j)) > 1
        Istr_tps(j) = min([TABI_hT(i), AETB12TUFI_hT(i),
    AETB8TUFI_hT(i), AMHC_hT(i), SAHC_hT(i), SAHC2_hT(i)
   , LI900_hT(i)]);
        i = i+1;
        if i == length(Q_prova_HT)
            Istr_tps(j) = 5;
            break
        end
    end
    end
end

Istr = Istr_tps*3.2808^2/2.2046; Istr_TPS = sum(Istr(1:
   length(Istr)))/(length(Istr));
```

C.3 Function: Orbit Reaching

```
    function [T_W] = orbitReachingReq4(tau,W,W_pay,Mmax,
   h,ROC,Istr,rho_pay,DV)

g0 = 9.81;
Kv0 = 0.4*(rho_pay/175.6)^0.123;                % (
   metric), si veda pag. 107 capitolo Curran
```

```
Kv = (Kv0 - 6.867e-3*tau^-1 + 8.2777e-4*tau^-2 - 2.811e-5*tau^-3)*1.1857;  % Scaled propellant volume fraction, si veda pag. 107 capitolo Curran
Kstr = (0.317)*tau^0.205;                                     % si veda pag. 34 capitolo Curran
tb = h/ROC;                                                  % Burning time
rho_f = 70.52;                                               % LH2 density [kg/m^3]
rho_ox = 1141;                                               % LOX density [kg/m^3]
MR = 6;                                                      % Mixure ratio
rho_ppl = rho_f*(1+MR)/(1+(rho_f/rho_ox)*MR);                % Propellent density
Kw = -93.831*tau^3 + 59.920*tau^2 - 5.648*tau + 2.821;         % wing body, si veda pag. 116 capitolo Curran
Ip = 107.6*10^(-0.081*Mmax);                              % Propulsion index, si veda pag. 9 capitolo Curran

a = Istr*Kv*Kstr*tau;
b = Ip*Kw;
W_ppl = @(W_S) (rho_ppl*W_pay*Kw./(a*W^0.71.*W_S.^-0.71-b));

%T_W = @(W_S) (rho_ppl*W_pay*Kw./(a*W^1.71.*W_S.^-0.71-b*W))*DV./ (g0*tb.*log(1+rho_ppl/Ip));
T_W = @(W_S) W_ppl(W_S).*DV./ (W*g0*tb.*log(W./(W-W_ppl(W_S))));
end
```

Bibliography

[1] J.P. Penn and C.A. Lindley. «Requirements and design for space tourist transportation». In: *1997 IEEE Aerospace Conference.* Vol. 3. 1997, 359–382 vol.3 (cit. on p. 1).

[2] Y Bhavana, N ManiShankar, and Prarthana Bk. «Reusable Launch Vehicles: Evolution Redefined». In: *Journal of Aeronautics and Aerospace Engineering* 2 (2013), pp. 1–5 (cit. on p. 1).

[3] Michael A. Rampino. «Concepts of Operations for a Reusable Launch Vehicle». MA thesis. Alabama, USA: The School of Advanced Airpower Studies, Maxwell Air Force Base, 1997 (cit. on p. 1).

[4] Loveneesh Rana. «SPACE ACCESS SYSTEMS DESIGN: Synthesis Methodology Development for Conceptual Design of Future Space Access Systems». Ph.D. dissertation. Texas, USA: The University of Texas at Arlington, Aug. 2017 (cit. on p. 2).

[5] E. Haney. «Data Engineering in Aerospace Systems Design and Forecasting». Ph.D. thesis. Texas, USA: The University of Texas at Arlington, May 2016 (cit. on p. 3).

[6] B. Chudoba and W. Heinze. «Evolution of generic flight vehicle design synthesis». In: *Aeronautical Journal* 114 (2010), pp. 549–567 (cit. on p. 3).

[7] E. H. Hirschel. *Basics of Aerothermodynamics.* Berlin, DE: Springer, 2005 (cit. on p. 4).

[8] Gerald D. Walberg. «A Survey of Aeroassisted Orbit Transfer». In: *Journal of Spacecraft and Rockets* 22 (1985), pp. 3–18 (cit. on p. 5).

[9] D. Ferretto. «Innovative Model Based Systems Engineering approach for the design of hypersonic transportation systems». Doctoral Dissertation. Torino, IT: Politecnico di Torino, 2020 (cit. on p. 6).

[10] K. D. Wood. *Aerospace Vehicle Design Volume II: Spacecraft Design.* Colorado: Johnson Publishing Company, 1964 (cit. on p. 10).

[11] J. L. Hunt. «Hypersonic Airbreathing Vehicle Design (Focus on AEROSPACE PLANE)». In: *Recent Advances in Multidisciplinary Analysis and Optimization, Part 3*. 1989, pp. 1157–1194 (cit. on p. 11).

[12] P. A. Czysz, C. Bruno, and B. Chudoba. *Future Spacecraft Propulsion Systems and Integration, Third Edition*. Springer, 2018 (cit. on p. 13).

[13] W. E. Hammond. *Design Methodologies for Space Transportation Systems*. AIAA Education Series, 2001 (cit. on p. 15).

[14] D. Ferretto, R. Fusaro, and N. Viola. «A conceptual design tool to support high-speed vehicle design». In: *2020 AIAA Aviation Conference*. 2020 (cit. on pp. 16, 62, 63).

[15] A. J. Butrica. *Reusable Launch Vehicles or Expendable Launch Vehicles? A perennial debat*. Tech. rep. AIAA Paper 2006-3890. NASA, 2006 (cit. on p. 17).

[16] D. A. Reed, H. Ikawa, and J. A. Sadunas. «Star-Raker: An Airbreather/Rocket-Powered, Horizontal Takeoff Tridelta Flying Wing, Single-Stage-to-Orbit Transportation System». In: *AIAA Conference on Advanced Technology for Future Space Systems*. Hampton, Virginia, 1979 (cit. on p. 18).

[17] R. L. Chase. *Earth-to-Orbit Reusable Launch Vehicles - A Comparative Assessment*. Tech. rep. National Aeronautics and Space Admintstration Langley Research Center, 1978 (cit. on p. 19).

[18] Kenneth Chang. «25 Years Ago, NASA Envisioned Its Own 'Orient Express'». In: *New York Times* (2014) (cit. on p. 20).

[19] C. Gelzer. «Rockwell X-30». In: *NASA Official Site* (2016) (cit. on p. 20).

[20] S. Ictoan and B. David. «HOTOL - The British Space Plane». In: *BBC* (2009) (cit. on p. 22).

[21] H. L. Hillebrand. «Japan Papier». In: *Flug Revue* (1989) (cit. on p. 23).

[22] Roger Longstaff. «From HOTOL to SKYLON British Spaceplane Programmes: Past, Present and Future». In: *18th AIAA International Space Planes and Hypersonic Systems and Technologies Conference*. Tours, FR, 2012 (cit. on pp. 24, 38, 76).

[23] R Gopalaswami. «Concept definition and design of a single-stage-to-orbit launch vehicle-hyperplane». In: *JBIS*. Vol. 63. 2010, pp. 395–405 (cit. on p. 25).

[24] *Radian Aerospace Official Site*. `https://www.radianaerospace.com`. Accessed: April 2024 (cit. on p. 26).

[25] E. Berger. «Radian announces plans to build one of the holy grails of spaceflight». In: *Ars Technica* (2022) (cit. on p. 26).

[26] *Bristol Spaceplane Official Site*. `https://bristolspaceplanes.com/projects/ascender/`. Accessed: April 2024 (cit. on p. 27).

[27] N. R. Anderson and C. Rodway. *XCOR Lynx Payload User's Guide*. Tech. rep. XCOR Aerospace, Inc., 2012 (cit. on p. 27).

[28] J. R. Olds and P. X. Bellini. «Argus, a Highly Reusable SSTO Rocket-Based Combined Cycle Launch Vehicle with Maglifter Launch Assist». In: *AIAA 8th International Space Planes and Hypersonic Systems and Technologies Conference*. Norflok, VA, 1998 (cit. on p. 29).

[29] J. R. Olds, J. Bradford, A Charania, L. Ledsinger, D. McCormick, and K. Sorensen. «Hyperion, a SSTO Vision Vehicle Concept Utilizing Rocket-Based Combined Cycle Propulsion». In: *AIAA 9th International Space Planes and Hypersonic Systems and Technologies Conference*. Norflok, VA, 1999 (cit. on p. 29).

[30] D. A. Young, T. Kokan, I. Clark, C Tanner, and A. Wilhite. «Lazarus: A SSTO Hypersonic Vehicle Concept Utilizing RBCC and HEDM Propulsion Technologies». In: *AIAA 14th International Space Planes and Hypersonic Systems and Technologies Conference*. Canberra, Australia, 2006 (cit. on p. 29).

[31] S. Salvi, C. Paravan, and L. Galfetti. «SSTO Reusable Launchers: a Critical Comparison of Propulsion Concepts». In: *9th European Conference for Aeronautics and Space Sciences (EUCASS)*. 2022 (cit. on p. 31).

[32] Abdul Ossman Ahmad, Christie Alisa Maddock, Thomas J. Scanlon, and Richard Brown. «Prediction of the aerodynamic performance of re-usable single stage to orbit vehicles». In: 2011 (cit. on p. 32).

[33] P.A. Czysz and J. Vanderkerkhove. «Transatmospheric Launcher Sizing». In: Scramjet Propulsion by E.T. Curran and S.B.N. Murthy, AIAA, 2000. Chap. 16, pp. 979–1103 (cit. on pp. 32, 47, 54, 58, 68, 69, 74, 82, 85, 86).

[34] W. Heiser and D. T. Pratt. *Hypersonic Airbreathing Propulsion*. AIAA Education Series, 1994 (cit. on pp. 36, 105, 107).

[35] V. F. Villacè. «Simulation, Design and Analysis of Air-Breathing Combined-Cycle Engines for High Speed Propulsion». Ph.D. thesis. Madrid, ES: Escuela Técnica Superior de Ingenieros Aeronáuticos, 2013 (cit. on p. 37).

[36] David Myers, Carl Martin, and Max Blosser. «Parametric Weight Comparison of Advanced Metallic, Ceramic Tile, and Ceramic Blanket Thermal Protection Systems». In: (July 2000) (cit. on pp. 40, 60, 61, 97).

[37] Michael K. Smart. «Scramjet Inlets Professor». In: 2013 (cit. on p. 51).

[38] Frederick S. Billig. «Design and development of single-stage-to-orbit vehicles». In: *Johns Hopkins Apl Technical Digest* (1990) (cit. on pp. 52, 74).

[39] R. Cau. «Characterisation and Simulation of Reusable Single-Stage-To-Orbit Vehicles Ascent Phase during Conceptual Design». Master's Thesis. Torino, IT: Politecnico di Torino, 2024 (cit. on pp. 53, 75, 86, 87).

[40] V. Dicristina. «Three-dimensional laminar boundary-layer transition on a sharp 8 degcone at Mach 10». In: *AIAA Journal* 8 (1969), pp. 852–856 (cit. on p. 56).

[41] J. Roskam. *Airplane Design, Part I: Preliminary Sizing of Airplanes.* Roskam Aviation and Engineering Corporation, 1985 (cit. on p. 64).

[42] M. Hempsell. *SKYLON User's Manual.* Tech. rep. SKY-REL-MA-0001. Reaction Engines Limited, 2014 (cit. on pp. 71, 72, 76, 85).

[43] Z. Spakovszky. *Unified: Thermodynamics and Propulsion.* Massachusetts Institute of Technology (MIT) (cit. on pp. 101, 103).

[44] Paras Ram, T. H. Kim, and Heuy Dong Kim. «Numerical Study on Shock Train Characteristics in Divergent Channels». In: *Journal of Applied Fluid Mechanics* 13 (2020), pp. 1081–1092 (cit. on p. 105).